

TECHNICAL REPORT STANDARD PAGE

1. Report No. FHWA/LA.11/442		2. Government Accession No.		3. Recipient's Catalog No.	
4. Title and Subtitle Development of Advanced Grid Stiffened (AGS) Fiber Reinforced Polymer (FRP) Tube-Encased Concrete Columns		5. Report Date March 2013			
		6. Performing Organization Code LTRC Project Number: 05-3ST State Project Number: 736-99-1357			
7. Author(s) Guoqiang Li, Ph.D.		8. Performing Organization Report No.			
9. Performing Organization Name and Address Department of Mechanical Engineering Louisiana State University Baton Rouge, LA 70803		10. Work Unit No.			
		11. Contract or Grant No.			
12. Sponsoring Agency Name and Address Louisiana Department of Transportation and Development P.O. Box 94245 Baton Rouge, LA 70804-9245		13. Type of Report and Period Covered Final Report 09/2005-12/2008			
		14. Sponsoring Agency Code			
15. Supplementary Notes Conducted in Cooperation with the U.S. Department of Transportation, Federal Highway Administration					
16. Abstract In this project, a new type of confining device, a latticework of interlacing fiber reinforced polymer (FRP) ribs that are jacketed by a FRP skin, is proposed, manufactured, tested, and modeled to encase concrete cylinders. This systematic study includes a thorough literature survey and the state-of-the-art knowledge in this research area was obtained. In the proof-of-concept study, advanced grid stiffened (AGS) tubes were fabricated by the hand lay-up technology per a pin-guided mandrel system. Both circular and square AGS tubes were manufactured and encased concrete cylinders and beams were tested using uniaxial compression and transverse bending. In the automatic manufacturing and parametric study, a pin-guided system assisted by a collapsible mandrel was developed to filament wind the AGS tubes automatically. A "building-block" test was conducted to reveal the step-by-step development of the composite action. After that, the effect of the rib thickness, skin thickness, and bay area on the structural behavior was evaluated experimentally. Also, the effect of rib thickness on the interfacial bonding strength was investigated using a push-out test. In the fire tolerance test, researchers investigated the enhancement of fire tolerance of AGS tube encased concrete cylinders as a result of incorporating organically modified montmorillonite (MMT) and a traditional fire retardant additive (TSWB®) into a vinyl ester (VE) matrix. Two series of specimens were prepared, fire-tested, and compression-tested to determine their residual load carrying capacity. A non-linear finite element analysis considering the nonlinear behavior of concrete, assisted by a non-associative Drucker-Prager plasticity criterion, was implemented to validate the experimental results and conduct the parametric study. In the engineering economic analysis, the life-cycle cost of new cylinders was compared to conventional steel reinforced concrete cylinders, both quantitatively and qualitatively. The results from this project showed that this type of novel cylinders outperforms the regular FRP tube encased concrete cylinders and has great potential to be used as columns in rebuilding or new construction of bridges or other infrastructure.					
17. Key Words FRP, Advanced Grid Stiffened, Concrete, Column			18. Distribution Statement Unrestricted. This document is available through the National Technical Information Service, Springfield, VA 21161.		
19. Security Classif. (of this report) N/A	20. Security Classif. (of this page) N/A	21. No. of Pages 127		22. Price N/A	

Project Review Committee

Each research project will have an advisory committee appointed by the LTRC Director. The Project Review Committee is responsible for assisting the LTRC Administrator or Manager in the development of acceptable research problem statements, requests for proposals, review of research proposals, oversight of approved research projects, and implementation of findings.

LTRC appreciates the dedication of the following Project Review Committee Members in guiding this research study to fruition.

LTRC Manager

Walid Alaywan, Ph.D., P.E.
Sr. Structures Research Engineer

Members

Gill Gautreau P.E.
Mike Ricca, P.E.
Paul Fossier, P.E.
Arturo Aguirre, P.E.
Michael Boudreaux, P.E.

Directorate Implementation Sponsor

Richard Savoie, P.E.

**Development of Advanced Grid Stiffened (AGS)
Fiber Reinforced Polymer (FRP) Tube-Encased Concrete Columns**

by

Guoqiang Li, Ph.D.
Associate Professor

Department of Mechanical Engineering
Louisiana State University
Baton Rouge, LA 70803

LTRC Project Number: 05-3ST
State Project Number: 736-99-1357

conducted for

Louisiana Department of Transportation and Development
Louisiana Transportation Research Center

The contents of this report reflect the views of the author/principal investigator who is responsible for the facts and the accuracy of the data presented herein. The contents do not necessarily reflect the views or policies of the Louisiana Department of Transportation and Development or the Federal Highway Administration, or the Louisiana Transportation Research Center. This report does not constitute a standard, specification, or regulation.

March 2013

ABSTRACT

In this project, a new type of confining device, a latticework of interlacing fiber reinforced polymer (FRP) ribs that are jacketed by a FRP skin, is proposed, manufactured, tested, and modeled to encase concrete cylinders. This systematic study includes a thorough literature survey and state-of-the-art knowledge in this research area was obtained. In the proof-of-concept study, advanced grid stiffened (AGS) tubes were fabricated by the hand lay-up technology per a pin-guided mandrel system. Both circular and square AGS tubes were manufactured and encased concrete cylinders and beams were tested using uniaxial compression and transverse bending. In the automatic manufacturing and parametric study, a pin-guided system assisted by a collapsible mandrel was developed to filament wind the AGS tubes automatically. A “building-block” test was conducted to reveal the step-by-step development of the composite action. After that, the effect of the rib thickness, skin thickness, and bay area on the structural behavior was evaluated experimentally. Also, the effect of rib thickness on the interfacial bonding strength was investigated using a push-out test. In the fire tolerance test, researchers investigated the enhancement of fire tolerance of AGS tube encased concrete cylinders as a result of incorporating organically modified montmorillonite (MMT) and a traditional fire retardant additive (TSWB®) into a vinyl ester (VE) matrix. Two series of specimens were prepared, fire-tested, and compression-tested to determine their residual load carrying capacity. A non-linear finite element analysis considering the nonlinear behavior of concrete, assisted by a non-associative Drucker-Prager plasticity criterion, was implemented to validate the experimental results and conduct the parametric study. In the engineering economic analysis, the life-cycle cost of new cylinders was compared to conventional steel reinforced concrete cylinders, both quantitatively and qualitatively. The results from this project showed that this type of novel cylinders outperforms the regular FRP tube encased concrete cylinders and has great potential to be used as columns in rebuilding or new construction of bridges or other infrastructures.

ACKNOWLEDGMENTS

This research project was funded by the Federal Highway Administration (FHWA)/ Innovative Bridge Research and Construction (IBRC) program and the Louisiana Transportation Research Center (LTRC). The investigator would like to thank FHWA and LTRC for sponsoring this project, especially Randy Young, Sadi Torres, John Eggers, and Alvin Mix, III. Matt Tircuit helped cast the concrete and test the confined concrete cylinders and other physical properties. Kelvin Schmit helped run the fire test. Dinesh Maricherla, Ravi Velamathy, Gefu Ji, Manu John, and Dr. Zhenyu Ouyang in the Department of Mechanical Engineering at Louisiana State University and Amanuel Ghebreyesus in the Department of Mechanical Engineering at Southern University assisted in the testing and modeling. Dr. Tao Xu at Louisiana State University assisted in formatting the final report. Dr. Walid Alaywan at LTRC, manager of this project, shared his experience and knowledge with the investigator. Sincere thanks also go to the PRC of this project for their meaningful suggestions.

IMPLEMENTATION STATEMENT

The original objective of the study was to develop an advanced grid stiffened (AGS) fiber reinforced polymer (FRP) tube-encased column and to implement the results through the construction and placement of this column on a new bridge construction site. The development of this product was successfully carried out and lab-tested. The report recommends a connection detail(s) between column and bent cap be developed and field tested in order to fully implement the findings of the research.

This project aims at developing a new confining device for rebuilding or for new construction of piers, piles, and columns in infrastructure. Because this is an innovative concept, there is no similar study in open literature. This study has answered several key questions: (1) The AGS tube has a positive composite action with the concrete core. It increases the elastic range and ultimate compressive strength as compared to conventional FRP tube encased concrete cylinders. (2) This study proves that the AGS tube can be manufactured using the filament winding machine associated with a pin-guided collapsible mandrel. (3) This type of cylinder can be designed using finite element modeling by considering nonlinear behavior of concrete assisted by a non-associative Drucker-Prager plasticity criterion. (4) The post-fire residual strength can be enhanced by incorporation of nanoclay in the skin. (5) This new type of column may be long-term cost-effective as compared to traditional steel reinforced concrete cylinders due to its corrosion-resistance and formwork-free construction.

A cost analysis was performed on a 10- ft. section of reinforced concrete column and FRP jacketed column. The analysis was performed on the procurement of the raw materials and constructing those sections. All others issues pertaining to excavation, placement, and connection to other bridge elements were assumed similar and thus were not included in the analysis. Though the cost of the 10-ft FRP jacketed member was about 23% higher than the reinforced concrete member, it should be noted that the FRP column demonstrated a larger axial load capacity than the other member. It is also worth noting that the FRP member is corrosion free since it does not contain any reinforcing steel.

Summarily, the FRP jacketed column offers many advantages when it comes to corrosion resistance, speed of installation, low maintenance, and durability when compared to the reinforced concrete column.

However, it must be indicated that this study is not ready to be used in practice because there are still several key questions that need to be answered that are out of the scope of this study. For example, if the AGS tube-confined concrete column is to be used as a pier, the joining

with foundation and superstructure must be solved. Also, if the novel column is to be used as a pile, its drivability must be validated through extensive dynamic testing, and if it is to be used as a fender, an impact test is necessary.

In summary, this project has demonstrated the success in designing and constructing an AGS/FRP tube encased concrete column as an alternate design for columns or piles.

TABLE OF CONTENTS

ABSTRACT.....	iii
ACKNOWLEDGMENTS	v
IMPLEMENTATION STATEMENT	vii
TABLE OF CONTENTS.....	ix
LIST OF TABLES	xiii
LIST OF FIGURES	xv
INTRODUCTION	1
OBJECTIVE	3
SCOPE	5
METHODOLOGY	7
Literature Survey	7
Type and Terminology of AGS Structures	7
Advantages of AGS Structures	9
Manufacturing Technology.....	10
Modeling of Structural Behavior of AGS Structures.....	16
Application to Reinforced Concrete Beams or Slabs	18
AGS Tube Confined Concrete Cylinders	20
Proof-of-Concept Study (Compressive Behavior).....	22
Raw Materials	22
AGS Tube Fabrication	23
Fabrication of AGS Tube Encased Concrete Cylinders	26
Instrumentation and Testing	27
Proof-of-Concept Study (Bending Behavior).....	28
Specimens' Preparation and Testing.....	28
Automatic Manufacturing and Parametric Study (Manufacturing and Compression Testing)	29
Raw Materials	29
AGS Tube Fabrication	30
Preparation of AGS Tube Encased Concrete Cylinders	32
Burn-out Test and Coupon Test.....	32
Instrumentation and Uniaxial Compression Test.....	33
Automatic Manufacturing and Parametric Study (Manufacturing and Push-out Test)	34
Raw Materials	34
AGS Tube Fabrication	35
Preparation of AGS Tube Encased Concrete Cylinders	35

Instrumentation and Push-out Test	36
Finite Element Modeling	37
Modeling FRP	38
Drucker-Prager Model	38
Non-linear Behavior of Concrete	39
Boundary Conditions and Loading	39
Enhancement of Fire Tolerance	40
Background	40
Raw Materials	40
Equipment	41
Specimen Fabrication	41
Fire Test and Uniaxial Compression Test	44
Engineering Economic Analysis	45
DISCUSSION OF RESULTS	47
Literature Survey	47
Proof-of-Concept Study (Compressive Behavior)	47
Axial Stress-Axial Strain Behavior	47
Specific Compressive Strength and Ductility	49
Volumetric Strain Behavior	50
Failure Mode	51
Summary	52
Proof-of-Concept Study (Bending Behavior)	54
Bending Strength and Ductility	54
Failure Mode	55
Summary	56
Automatic Manufacturing and Parametric Study (Manufacturing and Compression Testing)	56
Development of Composite Action	56
Effect of Design Parameters on the Structural Behavior of AGS Tube Encased Concrete Cylinders	59
Summary	63
Automatic Manufacturing and Parametric Study (Manufacturing and Push-out Testing)	64
Push-out Test of FRP Encased Concrete Tube	64
Push-out Test of AGS-FRP Tube Encased Concrete Cylinders	66
Push-out Strength and Failure Mode	67
Summary	69

Finite Element Modeling	70
FEA (Finite Element Analysis) Validation.....	70
Parametric Analysis	73
Effect of the Skin Axial Stiffness	74
Effect of Rib Thickness	74
Effect of Bay Area	75
Summary	76
Enhancement of Fire Tolerance	77
Burning Test.....	77
Uniaxial Compression Test Results	82
Summary	85
CONCLUSIONS.....	87
RECOMMENDATIONS	89
ACRONYMS, ABBREVIATIONS & SYMBOLS.....	91
REFERENCES	93
APPENDIX A.....	99
Engineering Economic Analysis.....	99
APPENDIX B	103
Computation of Axial Capacity of Different Sections.....	103

LIST OF TABLES

Table 1 Physical and mechanical properties of the raw materials used.....	23
Table 2 FRP skin coupon test results.....	26
Table 3 Physical/mechanical properties of the raw materials used	29
Table 4 Details of FRP tubes	32
Table 5 Elastic properties for each structural component of the AGS tubes	33
Table 6 Details of FRP tubes	35
Table 7 Detail of AGS tube	42
Table 8 Details of fabrication procedure for each group of specimens	43
Table 9 Absolute and specific peak bending load	55
Table 10 Schematic of the load carrying capacity of the composite elements	57
Table 11 Mass loss for each group of specimens	78
Table 12 Compressive strength for each group of specimens	85

LIST OF FIGURES

Figure 1 A schematic of axial stress-axial strain behavior of solid FRP tube-encased concrete cylinder.....	1
Figure 2 Basic grid structure	7
Figure 3 An isometric view of an orthogrid.....	8
Figure 4 A top view of an isogrid.....	8
Figure 5 An isometric view of an isogrid.....	9
Figure 6 A top view of quadric-grid.....	9
Figure 7 An example of hybrid tooling	12
Figure 8 Details of hybrid tooling	12
Figure 9 A schematic of expansion block tooling	12
Figure 10 PEG pattern with a central node pin	13
Figure 11 A pattern with 1.3° lead-in angle	13
Figure 12 A two-layer laminated lay-up pattern	14
Figure 13 Mold and resulting specimen with the four-pin concept.....	15
Figure 14 A schematic of the assembly concept for an ICG	16
Figure 15 An AGS cage	20
Figure 16 Axial rib failure at the end	21
Figure 17 Spalling of external concrete from the cage.....	21
Figure 18 Stacking of hoop ribs on longitudinal ribs.....	22
Figure 19 Slump test.....	22
Figure 20 Air content test.....	22
Figure 21 An aluminum mold	24
Figure 22 The mold with pins	24
Figure 23 Fabrication set-up.....	25
Figure 24 Winding fibers.....	25
Figure 25 Remove the tube from the stand	25
Figure 26 The AGS tube under UV curing	25
Figure 27 Remove the pins.....	25
Figure 28 A cured AGS tube	25
Figure 29 FRP skin wrapped (a) circular AGS tube and (b) square AGS tube.....	26
Figure 30 A circular AGS tube encased concrete cylinder under compression test	27
Figure 31 A square AGS tube encased concrete cylinder under compression test	28
Figure 32 Four-point bending test	29
Figure 33 Collapsible mandrel with holes.....	30

Figure 34 Winding the grid skeleton	31
Figure 35 An AGS tube	31
Figure 36 Schematic of strain gauge locations	34
Figure 37 Schematic the location of the strain gauges	36
Figure 38 DAQ DC-100 data collecting system.....	36
Figure 39 Specimen under push out test.....	37
Figure 40 TEM image of nanoclay morphology in VE matrix with varying mixing effort embedded thermocouples	43
Figure 41 Schematic locations of embedded thermal couples	44
Figure 42 Schematic of the specimen exposure to the jet fire [55].....	44
Figure 43 Comparison of specific axial stress-axial strain behavior of various types of tubes encased concrete cylinders	48
Figure 44 Change of volumetric strain with axial strain	51
Figure 45 Failure mode of (a) circular AGS cylinder under compression and (b) square AGS cylinder under compression.....	52
Figure 46 Four-point bending test	54
Figure 47 Comparison of FRP grid tube encased concrete beam with steel grid tube encased concrete beam under bending.....	55
Figure 48 Axial stress-strain behavior of various cylinders	59
Figure 49 Local stress-strain distributions	62
Figure 50 Failure mode	62
Figure 51 Specimens of Group A after push-out test	64
Figure 52 Specimens of Group B after push-out test	65
Figure 53 Shear stress/strain curve of Group A and B.....	65
Figure 54 Stress/strain curve from the strain gauges on the skin of FRP.....	65
Figure 55 Failure mode of Group D.....	66
Figure 56 Failure mode of Group E	66
Figure 57 Stress/strain curve from stain gauge	67
Figure 58 Comparing the shear stress of Group A to E	67
Figure 59 Stress/strain curve of Groups A to E.....	68
Figure 60 Specimen cut by diamond saw.....	68
Figure 61 (a) Group C, (b) Group D, and (c and d) Group E.....	69
Figure 62 Crushing and cracking of the concrete.....	71
Figure 63 Stress developed in each component in a Group 1 AGS tube encased concrete cylinder.....	72
Figure 64 Axial stress-strain graphs for a Group 1 AGS tube encased concrete cylinder	73
Figure 65 Axial stress-strain for a Group 6 AGS tube encased concrete cylinder.....	73

Figure 66 Effect of skin axial stiffness on the maximum hoop stress in the AGS tube	74
Figure 67 Effect of rib thickness on the maximum hoop stress in the AGS tube	75
Figure 68 Effect of bay area on the maximum hoop stress in the AGS tube	76
Figure 69 Effect of bay area on the maximum hoop stress in the AGS tube (including zero bay area)	77
Figure 70 AGS-FRPC specimens under the jet fire (a) front view and (b) side view.....	79
Figure 71 Temperature history during burning test at (a) location 1, (b) location 2, (c) location 3, and (d) location 4.....	81
Figure 72 (a) and (b) specimens before and after compression test with fire damage; (c) and (d) control specimens before and after compression test without fire damage	82
Figure 73 Compressive axial stress-axial strain behavior of AGS-FRPC cylinders and pure concrete cylinders without fire exposure.....	83
Figure 74 Compressive axial stress-axial strain behavior of AGS-FRPC cylinders after 5 minutes of fire exposure	83
Figure 75 Cross-section sketch of steel reinforced concrete column	100
Figure 76 Cross-section of the equivalent FRP jacketed concrete column	100

INTRODUCTION

In recent years, an ever-increasing attention has been paid to use fiber reinforced polymer (FRP) tube-encased concrete columns for new construction and rebuilding of engineering structures [1], [2]. The purpose in FRP tube-encased concrete columns is to replace the steel rebar by a corrosion-resistant laminated FRP shell. The FRP tube serves as a stay-in-place formwork during construction. During service, the tube confines the lateral expansion of the concrete core and transfers the core to a triaxial compressive stress condition. As a result, the compressive strength and ductility of the column are significantly enhanced. Also, owing to the inherent corrosion-resistance of FRP, it is maintenance-free, providing a long-term cost benefit.

Subjected to an axial compressive load, FRP confined concrete cylinders behave bi-linearly; see a schematic in Figure 1 [3-6]. The bilinear axial stress, axial strain response, consists of three distinct regions, i.e., two linear regions connected by a transition zone. In the first region (region 1), the stress-strain curve can be represented by a straight line, which almost repeats the stress-strain curve of the unconfined concrete. This suggests that the FRP tube cannot confine the concrete in this region. Once the axial stress reaches or is slightly higher than the unconfined concrete strength, a transition zone starts. In the transition zone (region 2), microcracks are produced gradually in the concrete core, resulting in a gradually increasing lateral expansion. As a result, the FRP tube is activated gradually to confine the lateral expansion and counteract the stiffness degradation of the concrete core. The transition zone can be represented by a smooth curve. Finally, a third region (region 3) is recognized in which the FRP tube is fully activated, and the stiffness is generally stabilized around a constant rate, similar to the stiffness of the FRP tube.

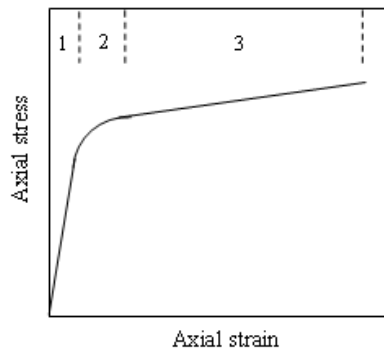


Figure 1
A schematic of axial stress-axial strain behavior of solid FRP tube-encased concrete cylinder

From the previous discussion, it is seen that confinement provided by the FRP tube is passive. The FRP tube cannot confine the concrete core until the concrete has sufficient lateral expansion, i.e., when the concrete is cracked or crushed. The higher ultimate compressive strength of the confined concrete cannot be realized unless the concrete is damaged and there is an excessive axial strain (an axial strain in the order of 0.02 or higher), which is much larger than the currently accepted design strain of 0.003, as specified by the American Concrete Institute (ACI 318-99). Since confined concrete cylinders are designed to work in the elastic region, i.e., the first linear region in the axial stress-axial strain curve, the strengthening potential of the FRP tube cannot be realized and utilized in practice. In order to utilize the strengthening potential of the FRP, the first region must be enlarged.

The reason for this can be summarized as follows [7]: (1) Due to the orthotropic structural properties and various couplings, a FRP tube usually has a much larger radial (out-of-plane) Poisson's ratio than that of a concrete core. Subjected to the same axial strain, the larger transverse Poisson's ratio of the FRP tube leads to a radial deformation larger than that of the concrete core. Consequently, the FRP tube cannot confine the concrete core in this region, i.e., the first region or elastic region in the stress-strain curve. (2) For most FRP tubes, fibers are aligned toward the hoop direction in order to provide higher confinement. As a result, the axial stiffness of the FRP tube may be lower than that of the concrete core. A lower axial stiffness also translates to a higher transverse or radial deformation.

While the axial stiffness of the FRP tube can be increased by using higher stiffness fibers or by aligning fibers along the axial direction, the out-of-plane Poisson's ratio may always be higher than that of concrete, i.e., it may always be the case that the FRP tube cannot confine the concrete core in the first region. Therefore, an innovative idea must be created in order for the FRP tube to confine the concrete core in the elastic region.

A viable way of solving this problem is to use a grid-stiffened composite tube. By using a hybrid tube (a lattice of steel grids wrapped by a FRP skin), it was proved that a mechanical interlocking between the tube and core was developed [8]. This ensured that the grid tube was activated or engaged in confining the concrete core once the axial load was applied. As a result, the steel-grid tube-confined concrete cylinders had a higher elastic region than the solid FRP tube-confined counterparts. Because FRPs behave linearly elastic while steel behaves as elastic-perfectly plastic, it is interesting to find how FRP grid tube-encased concrete cylinders behave.

OBJECTIVE

The objective of this study is to investigate the structural behavior of a novel AGS tube encased concrete cylinder through systematic experimental testing and finite element modeling. Parameters that determine the structural response will be evaluated. The fire resistance will be enhanced through nano-reinforcement. A life-cycle economic analysis will be conducted to evaluate the potential application of this novel column in bridge construction.

SCOPE

The scope of this project focused on lab-scale testing and numerical modeling. A field-level study was out of the scope of this study. This was a systematic experimental and numerical study. First, an extensive literature survey was conducted. The research focus was then on validating the concept. Following this, the focus was on the automatic manufacturing and parametric study through experimental testing. After that, the study was focused on non-linear finite element modeling. Furthermore, the enhancement of fire tolerance by nanoclay and fire retardant incorporation was investigated. Finally, the study concentrated on the life-cycle cost-benefit analysis. The test results and modeling results were analyzed and meaningful conclusions were obtained.

METHODOLOGY

Literature Survey

Type and Terminology of AGS Structures

A basic grid structure is a latticework of rigid, interconnecting beams in two, three, or four groups and directions [9, 10]. Figure 2 demonstrates an orthogrid AGS structure and the terminology used to describe it. Nodes, ribs, beams, and cells are the grid structure elements. *Nodes* are the crossover points, *ribs* are linear segments that span adjacent nodes, and *beams* are a collection of aligned ribs and nodes. *Cells* are the spaces enclosed between ribs. Structurally related terms are center-to-center, in-plane, and out-of-plane. *Center-to-center* indicates the distance between the centers of adjacent parallel beams. *In-plane* actions take place within the plane of the grid. *Out-of-plane* actions occur orthogonally to the plane of the grid. Element-level terms describe the rib cross-sectional dimensions where width is an in-plane measurement, while depth (height) is out-of-plane.

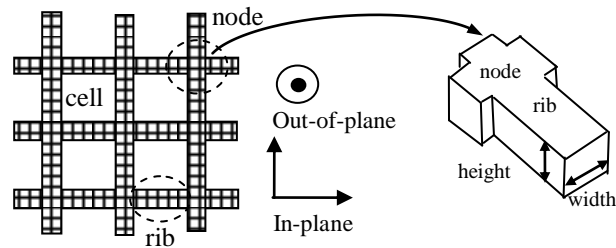


Figure 2
Basic grid structure

The displayed grid segment in Figure 2 comprises of beams placed in a bidirectional pattern, giving rise to the reference term *bi-grid*. A special case of the *bi-grid* is the one in which beams intersect orthogonally with equal spacing. In this configuration, there are two identical mechanical directions, and the term *orthogrid* is applied. Figure 3 shows an isometric view of an *orthogrid*.

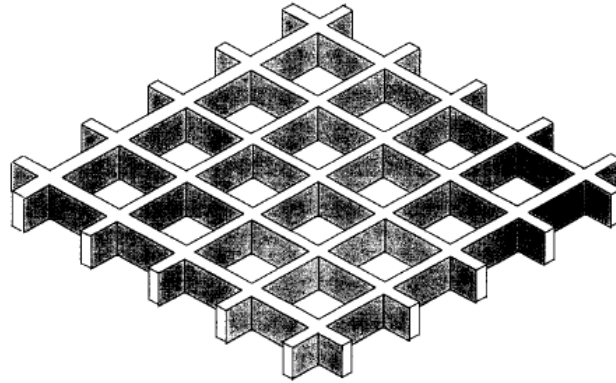


Figure 3
An isometric view of an orthogrid

Tri-grids are the next level of complexity, with three beam groups and directions. A special case of this tri-grid is known as an isogrid. The isogrid has three identical mechanical directions from the uniform distribution of beams at $0^\circ/\pm 60^\circ$ to form equilateral pockets, leading to quasi-isotropic in-plane stiffness. Figure 4 shows a top view of this grid type and Figure 5 shows an isometric view of this structure.

A final grid configuration, the *quadri-grid*, uses four beam groups. When equally distributed at $0^\circ/\pm 45^\circ/90^\circ$, this grid has four equivalent directions, again, leading to quasi-isotropic in-plane stiffness. The main benefit of this structure over the isogrid is not in the mechanical performance, but rather in the usefulness of the geometry. A rectangular plate cut from an isogrid has only two sides along which beams span the entire distance, which makes joining surrounding structures difficult. The same size plate cut from a *quadri-grid* can have beams spanning the entire perimeter, allowing for simple joining to surrounding structures. A top view of a quadric-grid is schematically shown in Figure 6.

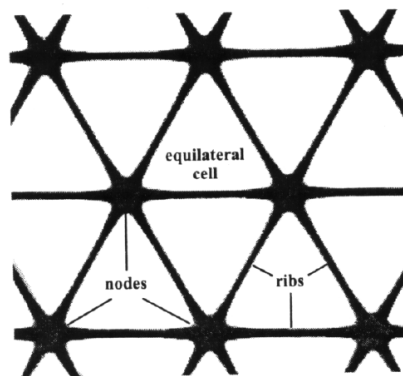


Figure 4
A top view of an isogrid

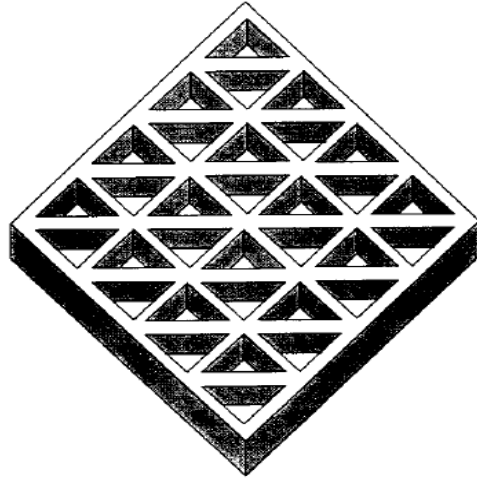


Figure 5
An isometric view of an isogrid

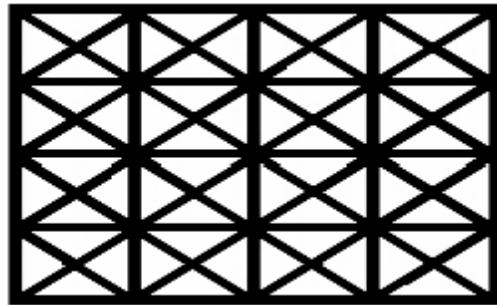


Figure 6
A top view of quadric-grid

Advantages of AGS Structures

A number of studies have been conducted to investigate the structural behavior of AGS structures experimentally and theoretically [9], [11-17]. These tests and analyses show that AGS structures are inherently resistant to impact damage, delamination, and crack propagation; they can achieve better performance in multiple directions by running ribs in several directions and by finding optimal rib orientations, and the grids carry loads collaboratively. The overall load carrying capacity can be fully utilized because grid failure proceeds along the direction of greatest strength. This configuration proves to be an inherently strong and resilient arrangement for composite materials, without the material mismatch associated with laminated structures.

Grids made of composite materials offer low mass with high stiffness and strength that are competitive with traditional composite laminates. Commonly available manufacturing processes such as filament winding, pultrusion, and tubes made from female molds can be

used to produce composite grids. Cost effective grids can then be made in large sizes and quantities. Grids derive their global stiffness and strength from their ribs. The models for stiffness and failure modes can be viewed as simple extensions of laminated plate theory. It is foreseen that grids will emerge as one of the common composite structural forms along with solid, stiffened, and sandwich panels. The most immediate potential payoff for FRP grid reinforcement is likely to be in structural applications that involve environments that are detrimental for steel use and that do not have restrictive deflection requirements. Applications in areas of harsh chemical exposure (e.g., salt) or restrictive electromagnetic requirements offer high potential payback for FRP grid use.

In summary, composite grid panels have several advantages over the conventional solid or sandwich panels as listed below:

- Unidirectional composite ribs have no material mismatch and they are unlikely to delaminate and have higher impact and fatigue resistance than laminated structures. In addition, by having separate ribs, cracks do not propagate to the next ribs and may promote damage tolerance.
- For the same amount of material, grid panels are always thicker than laminates and have higher flexural rigidity.
- Being an open structure, grids are not susceptible to moisture incursion as are sandwich panels. Also, inspection and repair of grids are relatively easy because they are open and repeated structures.
- Other typical benefits of composite materials, such as light weight, high stiffness and strength, high corrosion resistance, etc., are retained.

Manufacturing Technology

During the past 10 years, remarkable progress has been made in the manufacturing of AGS structures. Programs at the Boeing Company, the US Air Force Research Laboratory, McDonnell-Douglas (now part of the Boeing Company), Alliant Tech Systems, Composite Optics International Inc., Stanford University, and others have pushed the state-of-the-art technology in AGS structure's manufacturing, finally leading to processes and methods of interest to real-world production systems. It is well known that all AGS structures suffer from the same manufacturing difficulty: for an AGS structure to have all fibers continuous through a rib crossing point, there must be twice as much material in each crossing point as in each rib, making rib compaction difficult or impossible. For most manufacturing methods,

this difficulty leads to a buildup at the nodal points, which is undesirable for many reasons, including loss of strength, stiffness, and modeling accuracy.

Two types of tooling have been used by Huybrechts et al. to solve this problem: hybrid tooling and expansion block tooling [18]. Both provide lateral compaction of ribs during curing by taking advantage of the thermal expansion of tooling materials.

An example of the hybrid tooling is shown in Figure 7 and the details are shown in Figure 8. The hybrid tooling consists of a base and an expansion tool. The base is composed of a hard, thermally stable material with grooves cut into it. The expansion tool is composed of a high coefficient of thermal expansion material (for instance silicon rubber) and laid into the base tool. Prepreg tow is laid or wound into the groove in the expansion tool to create the structure's ribs. A skin is then laid up or wound over the top of the base tool.

Expansion block tooling consists of a "base tool," typically a stable, stiff material (for instance aluminum), and "blocks" made of a nearly incompressible material having a high thermal expansion coefficient (for instance cast silicon rubber). During curing, the blocks expand to provide lateral compaction to the ribs. The block can be bolted to the base or simply placed against it. The ribs can be laid up before or after the blocks are placed, depending on the process. A schematic of this tooling is shown in Figure 9.

In addition to the hybrid tooling and expansion block tooling methods, Dutta et al. introduced a pin-enhanced geometry system and nodal-offset concept to solve the nodal built-up problem [10]. Manufacturing high-quality grid structures requires the implementation of three concepts: (1) high nodal interlace density, (2) high fiber linearity, and (3) distributed fiber crossovers. Figure 10 shows the PEG (pin-enhanced geometry) pattern with a central node pin without any lead angle in the mold, and Figure 11 shows a pattern with 1.3° lead-in angle in the mold to smoothen the rib-node transition. However, alternating the placement of each roving to opposite sides of the pin did not reduce the node thickness to rib thickness. As a solution, a two-layer laminated lay-up pattern (shown in Figure 12) was used. In doing this, it was soon realized that while the expanded node volume and lead-in angle helped improve the volume fraction ratio between the ribs and node, the single pin in the middle disturbs the fibers and initiates dry zones.

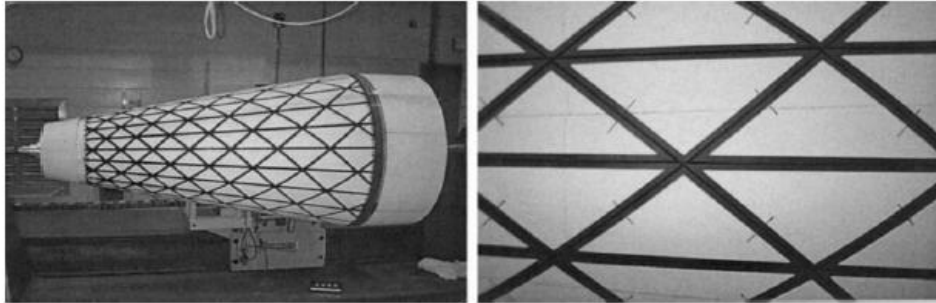


Figure 7
An example of hybrid tooling

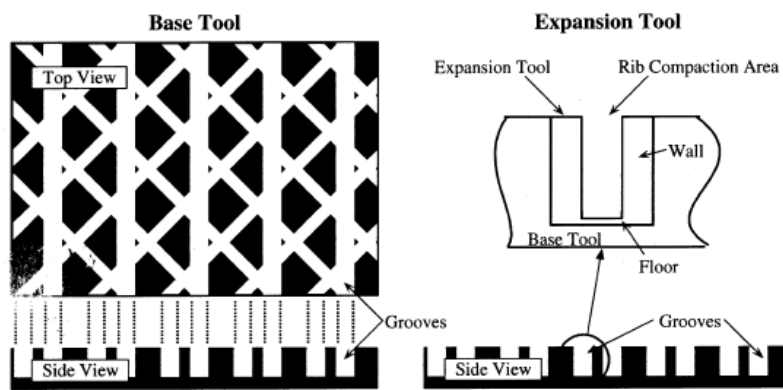


Figure 8
Details of hybrid tooling

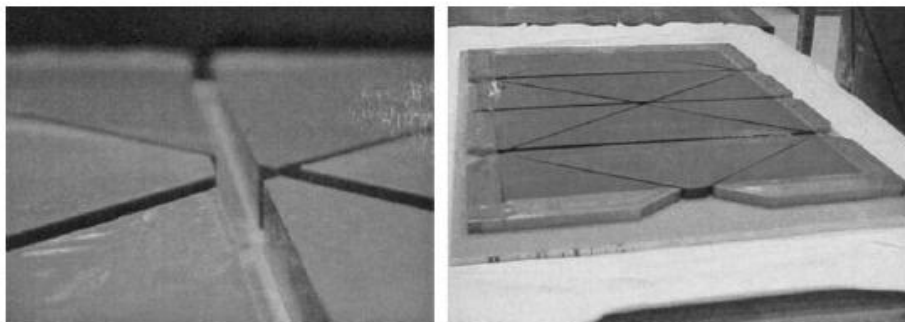


Figure 9
A schematic of expansion block tooling

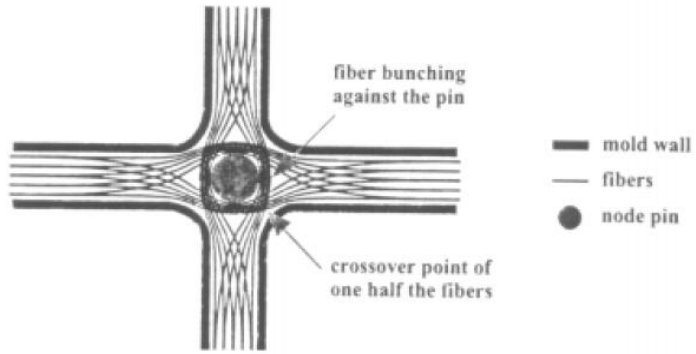


Figure 10
PEG pattern with a central node pin

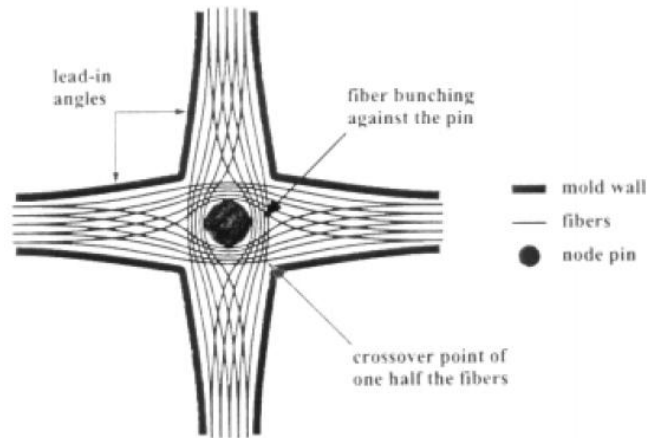


Figure 11
A pattern with 1.3° lead-in angle

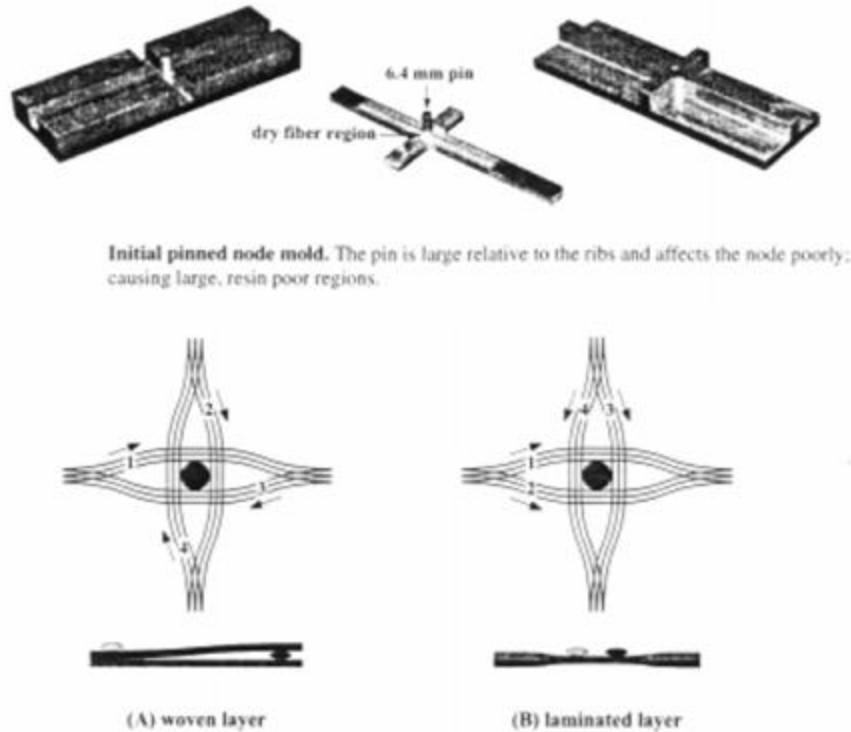


Figure 12
A two-layer laminated lay-up pattern

A follow-up modification was to replace the 0.25-in. (6.4-mm) central pin with four 0.06-in. (1.5-mm) pins at the node. Figure 13 shows the first mold and resulting specimen with the four-pin concept. In this test mold, the rib width was sized to the wetted diameter of the roving 0.10 in. (2.5 mm). The pins were located on the central axis of the ribs and set back from the node center such that four fiber paths had unobstructed 0.10-in. (2.5-mm) channels through the node. The wall geometry was designed to provide a minimum 0.10-in. (2.5-mm) gap between any wall and pin. The pins were intended to remain in the specimen following cure. A bolt at the end of each beam channel guided the roving and provided a tensioning point. This mold also used a new concept in part removal. Instead of machining channels into a solid metal plate, individual blocks were bolted to a base plate to form the channel pattern. After part lay-up and cure, the blocks were unbolted and lifted from the base plate with the specimen. The blocks were then knocked out from the specimen individually. This minimized the wall friction to overcome at any one time during removal and eliminated the need for release draft angles. Based on visual inspection, the specimens from this mold were successful. The fibers were straight throughout the specimen. The rib ply layers were indistinguishable and the vertical fiber density of the rib and node appeared equivalent. Measurements of the lateral fiber spread confirmed a nodal fiber width of approximately

twice the rib width (ratio of 1.9). Most specimens had geometry variations of less than 0.010 in. (0.25 mm) over the absolute design value. This variation was the result of the combined errors of mold machining and mold assembly, both of which could easily be reduced in better settings. In later attempts to force the fibers to conform properly, excessive pressure was applied during the cure cycle. Resin pools, fiber undulations, and wrinkles remained. In addition, resin-poor regions in the nodes also appeared. The nodal double-points supported the entire applied load, and the high nodal pressure forced most resin to flow into the low-pressure zones of the ribs. Beyond producing poor specimens, this method was found to damage the aluminum of the mold due to the concentrated load at the nodes. Following these experiences a process was developed that integrates methods of specified fiber placement, innovations in nodal geometry, and fiber tension. The greatest effort involves adding fiber guides to the nodes and modifying the shape of the nodes.

Recently, Han and Tsai [19] proposed another method to produce flat AGS panels. A new manufacturing method for a square grid using slotted joint and adhesive bonding (Interlocked Composite Grid or ICG) with pultruded ribs has been developed. Compared to previously proposed grids, it is mass producible at a lower cost. It has great potential for many applications, particularly for large civil structures. The conventional slotted joint is weak and not suitable for high performance grid structures. The innovation by Han and Tsai is to bond rib-caps over the open slots to provide additional load paths and to alleviate strength and stiffness reduction due to slots. A schematic of the assembly concept for an ICG is shown in Figure 14. The assembly starts with pultruded unidirectional ribs and rib-caps. Slots half the rib height are cut into the ribs. An orthogrid is formed by inserting the ribs into matching slots of one another. Rib caps are then bonded to the top and bottom sides of the ribs to bridge the open slots. The top and bottom caps are orthogonal to each other and the whole structure is thus interlocked.

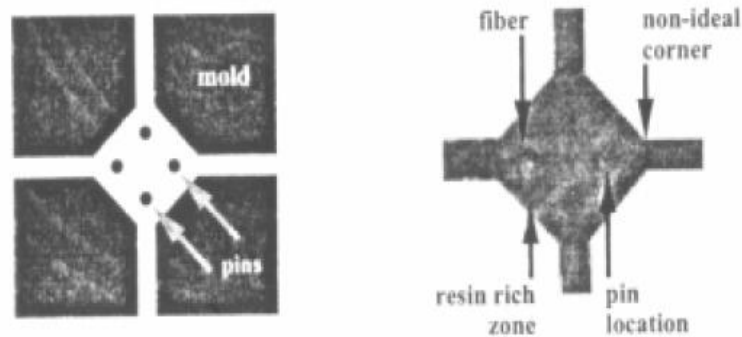


Figure 13
Mold and resulting specimen with the four-pin concept

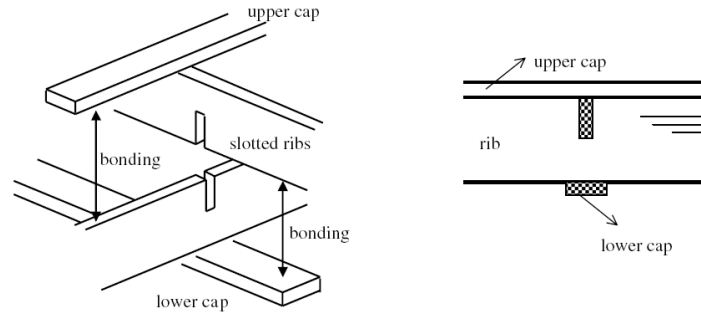


Figure 14
A schematic of the assembly concept for an ICG

Modeling of Structural Behavior of AGS Structures

The analysis of grid structures is well established and various mathematical models are available, in general, based on the smearing method, finite element analyses, and homogenization [9], [11], [13], [20-22]. The general idea in these studies is to transfer the periodic grid structure to an equivalent continuous anisotropic structure. Once this equivalent structure is obtained, the existing laminated plate theory can be employed to analyze the structural behavior subjected to various loading conditions. Recently, Li and Cheng developed a generalized analytical modeling without smearing and homogenization by considering the physical discontinuity from the rib to the bay [17]. It has been proved this method is robust and can be used to analyze and design orthogrid structures.

Among all the analyses, buckling analysis of cylinders is a focused topic because global or local buckling/crippling is a major failure mode of AGS structures. Over the past four decades, a number of studies have been focused on the buckling, collapse, and post buckling behavior of cylindrical shells [23]. A good portion of this work was devoted to the study of stiffened cylinders. The simplest stiffened cylinder consists of only axial stiffeners or stringers. A ring structure can be added to the stringers to achieve a better stiffened orthogrid configuration. The work by Graham presented an analysis method for determining the buckling loads of ring and stringer stiffened cylinders [24]. Another type of stiffener arrangement is the cross stiffeners arrangement. This results in a diamond-shaped pattern of stiffeners. Phillips and Gurdal discussed a smearing method for determining the global buckling load of this type of stiffened panels [25]. Isogrid stiffened cylinders consist of cross stiffeners at $\pm 60^\circ$ and horizontal stiffeners, resulting in equilateral triangle grid pattern of stiffeners. From previous studies, it is found that isogrid cylinders are in general more efficient than orthogrid cylinders [12]. Different analytical tools have so far been developed by researches to successfully predict the buckling failure modes associated with stiffened cylinders subjected to different loading conditions. These analytical tools are divided into three major categories:

Discrete Method. The discrete method models stiffeners as lines of axial ending and torsional stiffness on the skin. This approach is difficult to use when the panel is stiffened in more than two directions or when the stiffeners are not symmetric about the skin mid-surface, however can be quite useful for simpler stiffener arrangements. The work conducted by Wang and Hsu is a good example of this type of analysis [26].

Branched Plate and Shell Method. This method is the second approach for building analytical models of grid stiffened composite cylinders. This approach is more flexible and more accurate and usually involves the use of finite-elements modeling. The use of finite-elements analysis for investigation of buckling problem of composite cylinders is becoming popular due to the improvement in computational hardware and emergence of highly specialized software. Depending on the degree of accuracy desired and limit of computational cost, three types of buckling analyses can be carried out. Linear bifurcation analysis is the basic analysis type that does not take into consideration the prebuckling deformation and stresses. This analysis can accurately predict the buckling load of a geometrically perfect compressively loaded cylinder [27]. The second type of bifurcation analysis takes into consideration the nonlinear prebuckling deformation and stresses and results in a more accurate buckling load. The third analysis, the nonlinear buckling analysis, allows for large nonlinear geometric deflections. Unlike the previous two bifurcation analyses that are eigenvalue problems, the nonlinear analysis is iterative in nature. In this analysis the load is steadily increased until the solution starts to diverge. A number of studies have been conducted in finite elements analysis pertaining to the investigation of buckling of stiffened cylinders [27, 28]. One of the major drawbacks associated with this tool is the tedious model-building phase involved and the subsequent inconvenient parametric study.

Smearred Stiffener Method. This approach uses a mathematical model to smear the stiffeners into an equivalent laminate and determine the equivalent orthotropic stiffness of the laminate. A smeared stiffener theory that accounts for the skin-stiffener interaction was developed by Helms et al. [29]. In this work, a method was presented for the derivation of neutral surface profile of the grid/shell assembly by using minimum potential energy principle and static equilibrium conditions. However, this analysis was developed for a symmetric shell laminate and assumed a semi-infinite stiffened flat panel. Another work using the smeared approach was conducted by Phillips and Gurdal [25]. They analyzed the forces on a unit cell that represented the whole grid network and came up with equivalent stiffness parameters of the whole panel. The model developed was limited in the sense that it was restricted to symmetric panels, i.e., panels stiffened on both faces. Another area of interest for researchers studying buckling problems of cylinders is the effect of imperfections on the buckling load of cylinders. The work conducted by Hyer and Riddick was one of the

many papers published on this topic [28]. These authors examined the effect of measured imperfections on the buckling and postbuckling response of circular cylinders constructed of four distinct circumferential segments. In this work, the authors stated that the measured imperfections have an influence on the postbuckling response of the axially-stiff cylinders, but not on the circumferentially-stiff one. Optimization of grid stiffened composite cylinders is also an area of interest to many researchers. Jaunky et al. have studied the optimization of general stiffened composite circular cylinders [12]. They have considered all the possible modes of buckling failure. They have used genetic algorithm discrete optimization. In their study, they considered design variables like axial and transverse stiffener spacing, stiffener height, laminated skin thickness, and stiffening configuration.

Application to Reinforced Concrete Beams or Slabs

Sudden brittle failure and FRP rebar slippage have been a problem for years with FRP rebar reinforced concrete. This motivated the research of using AGS panel to reinforce concrete because of the mechanical interlocking between the grid and concrete. Early research in the field of composite grid reinforcement of concrete was reported by Sugita et al. of Japan, who worked with a New Fiber Composite Material for Reinforced Concrete (NEFMAC) grid made of either carbon fibers or a hybrid combination of carbon and glass fibers in a polymeric matrix [30]. Its primary use was to reinforce concrete. The applications included reinforcement for tunnel lining, shotcrete reinforcement, fender plates, and precast curtain walls (none of which are primary structural components). Other types of commercial FRP grids include IMCO (molded grating), DURADEK (pultruded grating), SAFE-T-GRATE, KORDEK (rectangular grating), KORLOK (pultruded grating), Fibergrate (rectangular grating), and custom-manufactured grids. The design of reinforced concrete structure requires that flexural behavior be understood. The flexural behavior of a reinforced concrete beam can be characterized by its ultimate strength, failure mode, stiffness (or amount of deflection), and predictability.

Composite materials generally have a higher ultimate strength than steel, which allows for higher ultimate loads in composite-reinforced concrete. Bank et al. tested a wide range of pultruded and molded gratings embedded in concrete beams [31]. All but one of the grid-reinforced beams exceeded the ultimate strength of the steel reinforced beam. Schmeckpeper and Goodspeed compared beams reinforced with NEFMAC composite grids with beams reinforced by an equivalent amount of steel based on axial rigidity of the reinforcement [32]. Their results showed significantly higher ultimate strengths with the composite-grid-reinforced beams over the steel-reinforced counterparts. In both research efforts, the higher composite tensile strength resulted in shear failure modes rather than tensile failure of the reinforcement. Larralde and Zervai took a different approach by comparing the flexural

behavior of FRP grating materials alone and embedded in concrete [33]. The purpose of the tests was to show that FRP structural grating that was designed to carry loads independently can be enhanced by adding concrete. The authors concluded that concrete can be used to enhance the stiffness of FRP grids and that using gratings for concrete reinforcement in corrosive applications is feasible. It is found that the general principles and theories currently applied to the design of reinforced concrete structures can be effectively applied to composite reinforcement as well. Banthia et al. tested the flexural response of reinforced concrete slabs and found that the current code equations can be effectively and accurately applied to FRP-reinforced concrete [34]. Shmeckpeper and Goodspeed investigated beams reinforced with NEFMAC grids and concluded that the flexural behavior can be predicted with current design procedures [32]. Sugita and Sugita et al. indicated that the Japanese have also explored the use of FRP-grid reinforcement for shotcrete applications [35], [30]. The prefabricated nature of the grid lowered the construction effort. The flexible nature of the grid that results from its lower stiffness permits easier placement on nonplanar surfaces such as those found in tunnels. These researchers have also found that the higher flexibility of the FRP grid results in fewer voids in the shotcrete matrix that later require filling, further reducing construction costs. This may indicate a viable use for FRP reinforcement in constructing concrete elements with curved surfaces (e.g., domes.). The variability in the types of composite grids available has created problems for research in the area of composite-grid-reinforced concrete. As can be inferred from the work that has been done, there is not a well-established basis for comparison. For the most part, researchers have used what is commercially available. This includes pultruded sections with mechanically attached crossmembers, molded gratings, different fibers, different volume fractions, and different spacings. Despite the difficulties, the past research has been fairly successful as a preliminary investigation. Researchers have shown that the fundamental principles used in design of reinforced concrete structures are directly applicable to composite reinforcement in concrete.

The interest in using AGS panels to reinforce concrete has continued in recent years [36-41]. Such grid reinforcement enhances the energy absorption capability and the overall ductility of the structure is improved, leading to an increase in ultimate load carrying capacity of concrete beams/slabs. It is found that when the opening of grids is filled with concrete, the combined structure derives its shear rigidity from the concrete filler and the concrete prevents the ribs from buckling. FRP composite grids provide a mechanical anchorage within the concrete due to the interlocking elements (cross-rods), thus no bond is necessary for proper load transfer. FRP 3-D grids provide integrated axial, flexural, and shear reinforcement and have the ability to cause a concrete beam to have a pseudo-ductile failure profile. A 2-D grid configuration ensures adequate force transfer to develop the axial tensile strength of the longitudinal bar. At tensile rupture, the grid nodes remained rigid and no

bearing or shear failure was observed between the transverse bar and surrounding concrete.

AGS Tube Confined Concrete Cylinders

Compared with extensive studies of using FRP grids in concrete beams or slabs, very few studies have been conducted on the use of FRP grids in concrete columns. Dutta et al. proposed a stacked joint grid to confine concrete cylinders [10]. The circular reinforcement was composed of two carbon fiber rings separated by extruded tubes. These tubes were bonded to the carbon fiber rings by an epoxy fill to make circumferential reinforcement elements called circs. The circs were connected via pultruded glass fiber reinforced polymer (GFRP) rods. These longitudinal rods, called longis, resist flexure while the carbon fiber reinforced circs contain the concrete under axial compression (Figure 15).

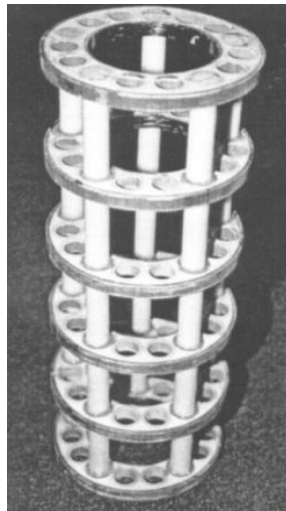


Figure 15
An AGS cage

The circs used in the stacked grids are 0.5-in. (12.7-mm) thick, composed of two hoop-wound carbon fiber reinforced rings, and separated by interior guide rings made from extruded polymers. The guide rings were bound to the inner and outer carbon fiber rings by vacuum-infiltrated epoxy. The finished first-generation circs contained 15 guide rings and the finished second-generation circs contained 21 guide rings, providing holes for the longis. The longis, GFRP rods pultruded with a high fiber volume fraction, serve as longitudinal reinforcement while providing spacing between the circs. The first-generation composite grid structures contained circs having a 7-in. (177.8-mm) outer diameter with a fully packed column of 15 longis, and the second-generation structures contained circs having an 8.125-in. (206.4-mm) outer diameter with a fully packed configuration of 21 longis. The grid structure was constructed by threading the longis through the holes provided by the guide rings and spacing the circs accordingly. After two or three longis connected the desired

number of circs, more longis could be added to the configuration. For the first-generation columns, a small amount of 5-minute epoxy was used to bond each of the circs to the longis at 90° angles. However, for the second-generation longis, only the end circs were bonded with epoxy. The middle circs were spaced with sections of cylindrical cardboard molds for concrete; these also served as the mold for the concrete cylinder. The edge of the cardboard tubing was bonded to the circs using caulk; the tubing and caulk were later removed after the concrete set.

From the above description, it is clear that the grid was not made of interlaced ribs in the real-sense. The load transfer between the axial and hoop ribs was weak. This led to early failure of the axial ribs; see Figure 16. Also, the grid was only a cage for internal reinforcement. Additional formwork was used for casting and curing concrete. This inevitably resulted in spalling of external concrete from the grid; see Figure 17.

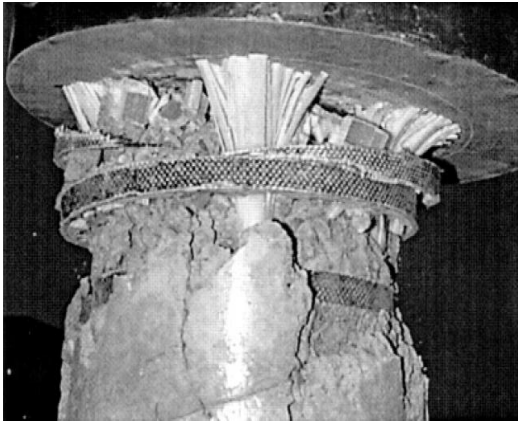


Figure 16
Axial rib failure at the end

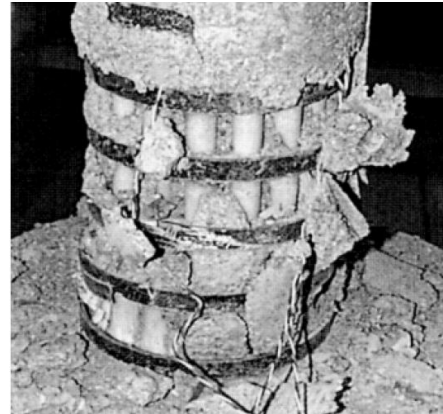


Figure 17
Spalling of external concrete from the cage

Recently, Saafi [42] also prepared FRP grid reinforced concrete columns. The test results show that, subjected to axial compressive load, the compressive strength and ductility of the reinforced column increased considerably. The axial strength-axial strain behavior is similar to that wrapped by FRP fabric. He also developed a stress-strain model and confinement model to predict the stress-strain behavior and ultimate strength and ductility. In his model, he smeared the hoop grids uniformly along the axis of the column. Using the same amount of FRP, it is found that the strengthening efficiency due to the hoop grids and the continuous FRP shell with hoop reinforcement is almost the same. The reason for this is that Saafi's grid was not an interlaced grid structure. Instead, the axial ribs and hoop ribs were stacked to each other; see Figure 18. This arrangement failed to provide the network load carrying capacity. Actually, Saafi reported that, subjected to axial compression, the hoop ribs separated from the axial ribs. Also, like Dutta et al. [10], Saafi's grid is only a reinforcement cage. It is not

an encasing tube. It can only be used to reinforce concrete internally. It cannot be used to encase concrete.

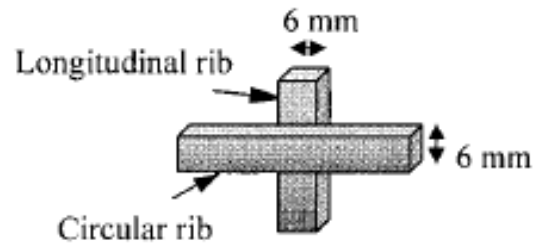


Figure 18
Stacking of hoop ribs on longitudinal ribs

Proof-of-Concept Study (Compressive Behavior)

Raw Materials

Type I Portland cement, gravel, natural sand, water, and a superplasticizer DAVA 170 were used to prepare the concrete. The mix design followed ACI Standard 211.1 (“Standard” 1991). The mix ratio by weight was cement: water: coarse aggregate: fine aggregate: admixture = 1: 0.56: 3.80: 2.19: 0.001. The maximum coarse aggregate diameter was 3/8 in. (9.5 mm). The slump was 5.52 in. (140.2 mm); the air content was 6.8 percent, and the 28-day cylinder compressive strength was 4.35 ksi (30 MPa). Figure 19 shows the slump test, and Figure 20 shows the air content test.



Figure 19
Slump test



Figure 20
Air content test

The AGS composite tubes were fabricated using a Fibrex 503 E-glass fiber roving and a Sunrez UV curing vinyl ester resin. The same fiber and resin were used to manufacture circular AGS tubes and square AGS tubes. For the FRP skin, the same resin was used. The fiber was a unidirectional E-glass 7715 style plain woven fabric. The physical and mechanical properties of the fibers and resin are given in Table 1.

Table 1
Physical and mechanical properties of the raw materials used

Materials	Viscosity at 77 °F (25 °C) lbf·s/ft ² (cps)	Tensile Strength ksi (MPa)	Modulus of Elasticity ksi (GPa)	Density lb _m /ft ³ (g/cm ³)
UV curing resin	0.010 (500)	10 (70)	610 (4.2)	66.8 (1.07)
Fiber roving	—	200 (1,379)	11,611 (80.0)	163.6 (2.62)
Woven fabric	—	435 (3,000)	10,160 (70.0)	164.2 (2.63)

AGS Tube Fabrication

While a number of manufacturing methods have been explored in literature, a hand lay-up process, which simulated the filament winding technology, was used to fabricate circular grid tubes [10, 18, and 19]. An aluminum mold with a hollow core was manufactured. The mold had an outer radius of 2 in. (50.8 mm) and was 12 in. (304.8 mm) high. On the surface of the mold, there were arrays of holes, which were drilled to accommodate rolled pins. The pins acted as guides for fibers along the hoop and longitudinal directions. The mold had holes in a group of four, and there were 12 longitudinal paths and 11 hoop paths for the fiber to pass through; see Figure 21. Before fabrication, the mold was cleaned and wrapped with a mylar sheet and a release agent was applied for demolding. The rolled pins were then hammered into the holes on the circular mold; see Figure 22. After this, a steel rod was passed through the hollow core of the mold and held on a stand at both ends. This simulated the mandrel in filament winding. The fiber spools were held on one extreme. The fibers from the spools were first passed through a roller in the resin bath and then through hooks on the upper wooden piece to guide them properly. The roller helped maintain tension during the fabrication process. In total, 12 fiber spools were used. Eleven of the resin wetted fiber rovings were aligned along the circumference of the mold, and the remaining one fiber roving was aligned along the longitudinal direction of the mold. The tension during this process was supplied and controlled by hand. After the first layer was wound, subsequent layers were laminated in a similar fashion and continued until eight layers were placed. Figure 23 shows the fabrication set-up, and Figure 24 shows winding hoop fibers onto the pin

guided mandrel. Once the eighth layer was laminated, the fiber was cut and the specimen was moved from the stand (Figure 25) and was exposed to an UV-A light source (or sunlight) for curing (Figure 26). Typical curing time was about half an hour for each specimen. Once the specimen was fully cured, the pins were removed and the mold was pushed out of the cured grid (Figure 27). To fabricate the square tubes, a square mold was manufactured and a procedure similar to the circular tubes was used.

The cured circular grid tube had an inner radius of 2 in. (50.8 mm) and a height of 12 in. (304.8 mm); the ribs had a thickness of 0.25 in. (6.25 mm) and width of 0.2 in. (5.08 mm). The bays were squares with a side length of 1 in. (25.4 mm). Figure 28 shows a cured circular grid tube. The square AGS tube had a height of 12 in. (304.8 mm) and the square cross-section with a side length of 4.50 in. (114.3 mm). Each bay was again a square with a side length of 1 in. (25.4 mm). A total of three circular AGS tubes and three square AGS tubes were prepared. The average weight of the circular tubes was 1.28 lb. (0.58 kg); it was 1.41 lb. (0.64 kg) for the square AGS tubes.

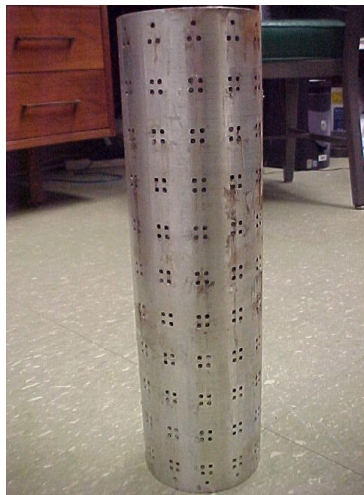


Figure 21
An aluminum mold

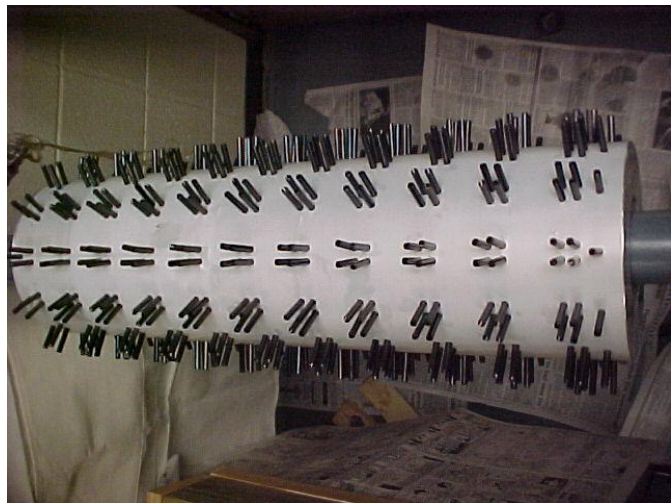


Figure 22
The mold with pins



Figure 23
Fabrication set-up

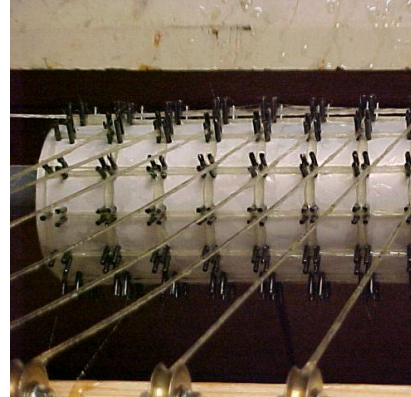


Figure 24
Winding fibers

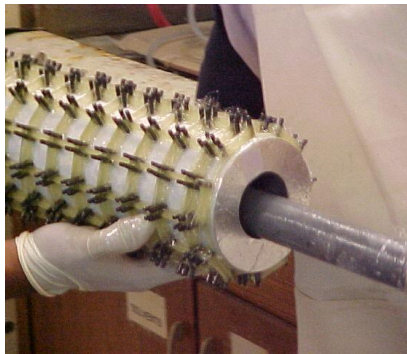


Figure 25
Remove the tube from the stand

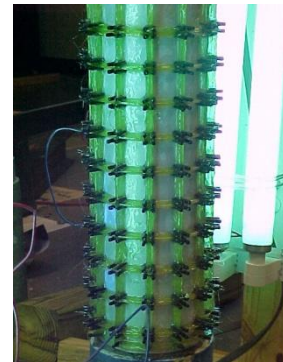


Figure 26
The AGS tube under UV curing



Figure 27
Remove the pins

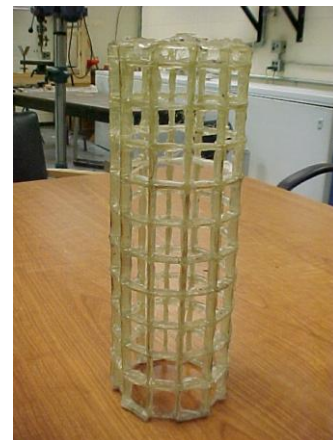


Figure 28
A cured AGS tube

A burn-off test per ASTM D2584 was used to determine the fiber volume fraction in the grids. It was found that the fiber volume fraction was about 30 percent. Unidirectional laminated composite beam coupons were prepared using the same fiber volume fraction and a unidirectional tension test was conducted per ASTM D3039. It was found that the longitudinal tensile strength of the ribs was 32 ksi (220 MPa), and the longitudinal modulus of elasticity was 5080 ksi (35 GPa).

Once the grid tube was cured and de-molded, it was wrapped with two layers of unidirectional E-glass 7715 plain woven fabric reinforced vinyl ester with fibers along the hoop direction. The cured thickness of the skin was 0.03 in. (0.738 mm). The coupon test results per ASTM D3039 are given in Table 2. Figure 29 (a) and (b) shows a wrapped circular AGS tube and a wrapped square AGS tube, respectively.

Table 2
FRP skin coupon test results

Types of coupons	Fiber orientation	Ultimate strain (%)	Tensile strength ksi (MPa)	Modulus of elasticity ksi (GPa)
FRP skin	0° fibers	2.32	46.5 (320.2)	2191.6 (15.1)
	90° fibers	0.85	5.7 (39.3)	566 (3.9)



(a)

(b)

Figure 29
FRP skin wrapped (a) circular AGS tube and (b) square AGS tube

Fabrication of AGS Tube Encased Concrete Cylinders

Once the AGS FRP tubes were prepared, concrete was then prepared, cast, compacted, finished, and cured in a standard curing room (with 100 percent relative humidity) for 28

days. The fabrication of the AGS FRP tube encased concrete cylinders was conducted at LTRC.

Instrumentation and Testing

In order to gain an in-depth understanding of the structural behavior of the hybrid composite cylinders, strain gauges were used to obtain local strain distributions. Two pairs of strain gauges were used for each specimen. Each pair contained two strain gauges mounted at the mid-height of the cylinder aligned in the hoop and axial directions, respectively. The two pairs were spaced at 180° in the hoop direction. The strain gauges were mounted on the surface of the FRP skin above the ribs. During the axial compression test, each specimen was loaded uniaxially to about 40 percent of the compressive strength of the unconfined concrete 4.35 ksi (30.0 MPa) and unloaded to guarantee close contact between each component. Then, the specimen was reloaded until failure. The compression testing was conducted using a FORNEY machine, with a capacity of 604 kips (2,688 kN). The assembled computer data acquisition system can directly record the load-displacement curves. The strain was recorded using a Yokogawa DC100 Data Acquisition Unit. Compression testing was conducted per ASTM C 39. The loading rate was 0.03 kip/s (0.23 MPa/s). Figure 30 shows a circular cylinder under compression test and Figure 31 shows a square cylinder under compression test.



Figure 30
A circular AGS tube encased concrete cylinder under compression test



Figure 31
A square AGS tube encased concrete cylinder under compression test

Proof-of-Concept Study (Bending Behavior)

Specimens' Preparation and Testing

Three grid tubes that had a square cross-section with a side length of 4.5 in. (114.3 mm) and a height of 22 in. (558.8 mm) were also prepared using the same raw materials as the grid tubes in the compressive behavior study. The ribs had a thickness of $\frac{1}{4}$ in. (6.25 mm) and width of 2 in. (50.8 mm). The bays were squares with a side length of 1 in. (25.4 mm). The average weight of the square AGS tubes was 2.9 lb. (1.31 kg). The three tubes were also cast with the same concrete and cured with the same condition. After 28 days of curing, they were tested using transverse bending in order to evaluate their flexural properties.

Four-point bending tests were conducted on each encased square beam specimen. This was a simply supported bending test with a span length of 18 in. (457.0 mm). Each specimen was first loaded with a preload of 4.5 kips (20 kN) to guarantee close contact between each component. The specimen was then unloaded and reloaded until failure. The tests were conducted using the same FORNEY machine per ASTM C 78. The loading rate was 52 lbs/s (230 N/s). Figure 32 shows a square beam under the four-point bending test.



Figure 32
Four-point bending test

Automatic Manufacturing and Parametric Study (Manufacturing and Compression Testing)

Raw Materials

The AGS cylinders were manufactured using a two-axis filament winding machine. Glass fibers and vinyl ester resin were used in fabrication. The resin used is DERAKANE 510C-350 vinyl ester resin by Dow Chemical Co. The composition of the resin contains 98 percent vinyl ester + 2% (MEKP + Cobalt Napthanate). The gel time of the resin can be increased by adding gel time retarder. The fiber used was FIBEREX continuous glass fiber roving RO99. FIBEREX single end roving is made of the E-CR glass formulation. It has superior mechanical, electrical, and corrosion resistance properties and is a preferred choice for most filament winding applications. The physical/mechanical properties of the raw materials provided by the manufacturers are given in Table 3.

Table 3
Physical/mechanical properties of the raw materials used

Material	Tensile Strength ksi (MPa)	Modulus of Elasticity ksi (GPa)	Density lb _m /ft ³ (g/cm ³)	Poisson's Ratio	Shear Modulus ksi (GPa)
Vinyl Ester Resin	12.5 (86)	464.4 (3.2)	71.2 (1.14)	0.35	171.3 (1.18)
E-glass Fiber	330.5 (2277)	10,907 (75.15)	163.6 (2.62)	0.25	444.2 (30.06)

Holcim Type I Portland cement, gravel, natural sand, water, and DAVA 170 were used to prepare the concrete. The mix design followed the American Concrete Institute (ACI) Standard 211.1 ("Standard" 1991). The nominal maximum coarse aggregate size was ¾ in.

(19.0 mm). The mix ratio by weight for the concrete was cement: water: gravel: sand: admixture = 1: 0.51: 3.49: 1.88: 0.001. It was found through concrete experiments that the slump was 6 in. (15.2 cm), the air-content was 8.1 percent, and the 28-day cylinder compressive strength per ASTM C39 was 7.3 ksi (50.0 MPa).

AGS Tube Fabrication

A filament-wound manufacturing technique was used to fabricate these AGS tubes. The filament winding process basically consists of winding a continuous resin impregnated fiber roving onto a rotating mandrel. This method offers good control over fiber placement and uniformity of the structure. In order to use the Little Hornet WLH two-axis filament winder to fabricate the AGS tubes, a pin-guided system assisted by a collapsible mandrel was developed. To prepare the collapsible mandrel, a 4-in. (101.6-mm) inner diameter FRP pipe was cut into two halves. Holes were drilled at the desired location to accommodate the pins. The pins basically acted as guides along which the fibers were arranged to form the grid pattern. Figure 33 shows the two-halves of the collapsible mandrel with drilled holes.

A mold releasing agent was sprayed onto the mandrel of the existing filament winding machine and the two halves of the collapsible mandrel were mounted on it. Rolled pins were then hammered into the holes of the collapsible mandrel. The resin was prepared and poured into the resin bath of the filament winding machine through which the fiber roving passed and wound onto the rotating mandrel. The desired pattern of the grid was generated by controlling the translation speed of the carriage and the rotating speed of the mandrel. For the AGS tubes with a skin, the skin was filament-wound onto the grid skeleton using the same filament winding machine after the grid skeleton was cured. Figure 34 shows winding the grid skeleton.



Figure 33
Collapsible mandrel with holes



Figure 34
Winding the grid skeleton

It is noted that this method cannot be used to fabricate hoop ribs (0° ribs) because the fiber roving must move along the axial direction to keep the fiber continuous and obtain the grid pattern. Here the hoop direction is defined as the circumferential direction of the tube, axial direction is along the cylindrical axis of the tube, and radial direction is along the wall thickness direction of the tube. Therefore, the grid was actually formed by axial ribs and helical or spiral ribs. The angle of the helical ribs depended on the pitch of the spiral. Because of the pins, helical ribs with a small hoop angle (pitch) can be fabricated. For the skin, the minimum hoop angle that can be reached was 10° without slipping due to the lack of pins.

Because of the small angle of the helical ribs, the bay or cell was not a square. It was a rhombus. Also, because of the constraint of the pins, all the axial ribs had almost the same width 0.3 in. (8.5 mm) and all the helical ribs had almost the same width 0.2 in. (5.5 mm). The change was the thickness of the ribs along the radial direction. Figure 35 shows a fabricated AGS tube.



Figure 35
An AGS tube

All AGS tubes were 12 in. (304.8 mm) in length and 4.5 in. (114.3 mm) in inner diameter. A total of 10 groups of tubes were prepared. Each group contained three identical specimens except for Group 1, which contained six identical specimens. The details of each group of AGS tubes are summarized in Table 4. It is seen that the purpose of Groups 1, 2, and 3 was to investigate the effect of the rib thickness; by comparing Groups 1, 4, and 5, the effect of the skin thickness could be found, and by comparing Groups 1, 6, and 7, the effect of the bay area could be observed. By comparing the Groups 1 and 8, the effect of the skin fiber orientation can be evaluated. The purpose of preparing Groups 9 and 10 was to conduct a building-block test in order to investigate the development of the composite action. By comparing Groups 9 (skin only), 10 (grid skeleton only), and 1 (skin wrapped grid), the development of composite action could be identified.

Table 4
Details of FRP tubes

Group No.	Rib thickness in. (mm)	Angle of helical ribs with the hoop direction (°)	Skin thickness in (mm)	Angle of skin fiber with the hoop direction (°)	Bay area in ² (mm ²)
1	0.50 (12.7)	6.06	0.16 (4.10)	10.0	2.2 (1415.6)
2	0.25 (6.35)	6.06	0.16 (4.10)	10.0	2.2 (1415.6)
3	0.75 (19.0)	6.06	0.16 (4.10)	10.0	2.2 (1415.6)
4	0.50 (12.7)	6.06	0.11 (2.73)	10.0	2.2 (1415.6)
5	0.50 (12.7)	6.06	0.22 (5.47)	10.0	2.2 (1415.6)
6	0.50 (12.7)	4.05	0.16 (4.10)	10.0	1.0 (645.2)
7	0.50 (12.7)	8.06	0.16 (4.10)	10.0	4.0 (2580.6)
8	0.50 (12.7)	6.06	0.16 (4.10)	35.0	2.2 (1415.6)
9	—	—	0.16 (4.10)	10.0	—
10	0.50 (12.7)	6.06	—	—	2.2 (1415.6)

Preparation of AGS Tube Encased Concrete Cylinders

Before casting concrete, one end of the AGS tube was capped using a plastic sheet. The concrete was then cast, compacted, finished, and cured for 28 days in a standard wet curing room with a relative humidity of 100 percent. The tubes from Groups 1-8 in Table 4 were filled in with concrete. Each group contained three identical specimens. The total number of AGS tube encased concrete cylinders was 24. For those tubes having strain gauges inside the tube, the strain gauges were pasted on the designed locations before casting concrete.

Burn-out Test and Coupon Test

A burn-out test per ASTM D2584 was used to determine the fiber volume fraction in the FRP ribs, nodes, and skin. It was found that the fiber volume fraction in the ribs was about 27 percent; it was about 54 percent in the nodes and 48 percent in the skin.

Some axial ribs were directly cut from the grid skeleton to conduct uniaxial tension test per ASTM D3039. It was found that the longitudinal tensile strength of the ribs was 32 ksi (220 MPa). The modulus and Poisson's ratio required in the future finite element analysis, which were not tested in this study, were estimated using the rule-of-mixture's method per Table 4 and fiber volume fraction of 27 percent for the ribs, 54 percent for the nodes, and 48 percent for the skin [45]. The results are summarized in Table 5. In Table 5, subscript "1" represents the longitudinal direction, and subscripts "2" and "3" denote the two transverse directions in the principal material coordinates.

Table 5
Elastic properties for each structural component of the AGS tubes

Structural Component	E ₁ ksi (GPa)	E ₂ ksi (GPa)	E ₃ ksi (GPa)	v ₁₂	v ₂₃	v ₃₁
Rib	3311.2 (22.84)	628.5 (4.33)	628.5 (4.33)	0.32	0.35	0.06
Node	6.098.7 (42.02)	981.1 (6.76)	981.1 (6.76)	0.29	0.35	0.047
Skin	5476 (37.73)	859.2 (5.92)	859.2 (5.92)	0.3	0.35	0.047

Instrumentation and Uniaxial Compression Test

In order to gain an in-depth understanding of the composite structural behavior, strain gauges were used to obtain local strain distributions. Ten strain gauges were used for each AGS tube encased concrete cylinder. The strain gauges were mounted at the middle height of the cylinder. Strain gauges were pasted both inside the tube (on the nodes) and outside the tube (on the skin). Figure 36 shows a schematic of the strain gauge locations. Although Figure 36 shows five strain gauges, there are five more strain gauges pasted on the opposite side of the tube, leading to a total of 10 strain gauges in each tube.

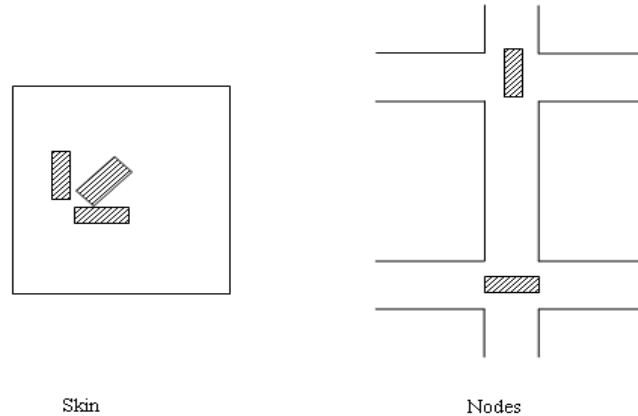


Figure 36
Schematic of strain gauge locations

Each encased concrete cylinder was uniaxially compressed to about 40 percent of the unconfined concrete strength and unloaded to guarantee close contact between each component and to reduce errors in displacement measurement. Then, the specimen was reloaded until FRP failure. FRP failure can be identified visually by the localized whitening and cracking of the FRP and audibly by the loud noise. It can also be identified from the stress-strain curve with a peak stress followed by a large and sudden drop or a continuously descending post-peak branch. The compression tests were conducted using a FORNEY machine. This machine has a capacity of 604 kips (2,688 kN). The assembled computer data acquisition system can directly record the load-displacement curves. The strain was obtained using a Yokogawa DC100 Data Acquisition Unit. The compression test was conducted per the ASTM C39 standard. The loading rate was 0.03 ksi/s (0.21 MPa/s).

Automatic Manufacturing and Parametric Study (Manufacturing and Push-out Test)

Raw Materials

The AGS cylinders were manufactured using a two-axis filament winding machine. Glass fibers and vinyl ester resin were used in fabrication. The resin used is DERAKANE 510C-350 vinyl ester resin by Dow Chemical Co. The composition of the resin contains 98 percent vinyl ester and 2 percent (MEKP Cobalt Naphthanate). The gel time of the resin can be increased by adding a gel time retarder. The fiber used was FIBEREX continuous glass fiber roving RO99. FIBEREX single end roving is made of the E-CR (a kind of “electronic” glass without boron and fluorine) glass formulation. It has superior mechanical, electrical, and corrosion resistance properties and is a preferred choice for most filament winding applications.

Holcim Type I/II Portland cement, gravel, natural sand, water, and type 120 slag were used to prepare the concrete. The mix design followed the American Concrete Institute (ACI)

Standard 211.1 (“Standard” 1991). The nominal maximum coarse aggregate size was $\frac{3}{4}$ in. (19.0 mm). The mix ratio by weight for the concrete was cement: water: gravel: sand: admixture = 1: 0.51: 3.49: 1.88: 0.001. It was found through concrete experiments that the slump was 2.5 in. (6.35 cm); the air-content was 1.5 percent, and the 28-day cylinder compressive strength per ASTM C39 was 3.67 ksi (25.3 MPa).

AGS Tube Fabrication

The filament-wound manufacturing technique was used to fabricate these FRP and AGS-FRP tubes. The filament winding process followed the process as described in the manufacturing and compression testing study. The details of the FRP and AGS-FRP tube are presented in Table 6. Groups C, D, and E are AGS-FRP tubes; Group A is a regular FRP tube having the same materials as Group D, and Group B is also a regular FRP tube having the same wall thickness as Group D (i.e., larger amount of materials than that of Group D). Groups A to E have the same inner diameter of 4.5 in. (114.3 mm). All specimens have the same height of 12 in. (304.8 mm).

Table 6
Details of FRP tubes

Group No.	Rib thickness in. (mm)	Angle of helical ribs with the hoop direction (°)	Skin thickness in. (mm)	Angle of skin fiber with the hoop direction (°)	Bay area in ² (mm ²)
A	—	—	0.41 (10.5)	10.0	—
B	—	—	0.66(16.8)	10.0	—
C	0.25 (6.35)	6.06	0.16 (4.10)	10.0	1.00 (645.2)
D	0.5 (12.70)	6.06	0.16 (4.10)	10.0	1.00 (645.2)
E	0.75 (19.05)	6.06	0.16 (4.10)	10.0	1.00 (645.2)

Preparation of AGS Tube Encased Concrete Cylinders

Before casting concrete, one end of the FRP and AGS-FRP tubes were capped using a plastic sheet. The concrete was then cast, compacted, finished, and cured for 28 days in a standard wet curing room with a relative humidity of 100 percent. Each group contained three identical specimens. The total number of FRP tube encased concrete cylinders was six and the total number of AGS-FRP tube encased concrete cylinders was nine. For those tubes having strain gauges inside the tube, the strain gauges were pasted on the designed locations before casting concrete.

Instrumentation and Push-out Test

In order to gain an in-depth understanding of the composite structural behavior, strain gauges were used to obtain local strain distributions. Strain gauges were used for each FRP and AGS-FRP tube encased concrete cylinder. The strain gauges were mounted at the middle height of the cylinder. Strain gauges were mounted both inside the tube (on the nodes) and outside the tube (on the skin) was pasted. Figure 37 shows a schematic of the strain gauge locations. Five strain gauges were pasted on the AGS-FRP tube in each tube, but only three strain gauges were pasted on the skin of each FRP encased cylinder. Data were collected by the DAQ-DC100 device, as shown in Figure 38. The data storage frequency was the same as the FORNEY machine around 2 Hz.

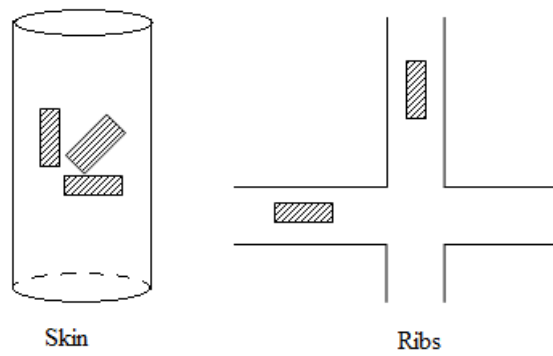


Figure 37
Schematic the location of the strain gauges



Figure 38
DAQ DC-100 data collecting system

Push-out tests were conducted on each encased cylinder specimen. A 2- in. (50.8-mm) high bolt steel ring and a cylinder block were used to do the push-out test. The inner diameter of the steel ring is 4.5 in. (114.8 mm), and the outer diameter of the steel block is 4.5 in. (114.3 mm). Before the push-out test, each specimen was ground and finished on both the top and

bottom surfaces. The push-out experiment set-up is shown in Figure 39. The cylinder steel block was located at the center of the specimens first, and then the steel ring was located around the perimeter of the cylinder.



Figure 39
Specimen under push out test

Each specimen was first loaded with a preload of 4.5 kips (20 kN) to guarantee close contact between each component. The specimen was then unloaded and reloaded until failure. The tests were conducted using the same FORNEY machine per ASTM C 78. The loading rate was 52 lbs/sec (230 N/s).

Finite Element Modeling

Although experimental testing can provide direct evidence of the effect of each design parameter on the structural behavior of the confined concrete cylinders, it is time consuming and expensive. In order to conduct a parametric study and to provide a design tool for this type of AGS tube encased concrete cylinders, FEA is a useful tool. In this study, ANSYS 10.0 software package was used.

Modeling FRP

The hoop direction ribs were modeled as having helical geometry. For the cross-over points of axial ribs and hoop ribs, i.e., nodes, they were modeled as individual entities having different material properties from the ribs. The fibers in the axial stiffeners were oriented along their length and fibers in the hoop direction were oriented in the helical direction. The skin was modeled as having an angle of $\pm\theta$ from the hoop direction. The skin and the stiffeners were glued together upon meshing to ensure displacement compatibility. The ribs and nodes were modeled using a 3D layered SOLID191 element, and the skin was modeled using a SOLID46 element.

Drucker-Prager Model

SOLID65 was used for 3D modeling of concrete without reinforcing bars. The element is capable of cracking in tension and crushing in compression. In the present analysis, confined concrete was modeled as an elastic-perfectly plastic material and the failure was analyzed using a non-associative Drucker-Prager plasticity criterion. The main advantage of Drucker-Prager (DP) type plasticity is that it minimizes the number of parameters by assuming an elastic-perfectly plastic response. The required DP parameters for analyzing concrete are (1) cohesion (c), (2) angle of internal friction (Φ), and (3) dilatancy angle (Φ_f). The cohesion and internal friction angle for concrete are given by the following relations [49]:

$$f'_{co} = \frac{2c \cos \phi}{1 - \sin \phi} \quad (1)$$

$$k_1 = \frac{1 + \sin \phi}{1 - \sin \phi} \quad (2)$$

where k_1 is the confinement effectiveness factor and f'_{co} is the unconfined concrete strength. For FRP confined concrete cylinders, there are many confinement models available in literature. It is well known that the Richart's model ($k_1 = 4.1$) overestimates the confinement efficiency of FRP tubes [5], [6], [50]. Due to the mechanical interlocking between the AGS tube and the concrete core, it is believed that the AGS tube encased concrete cylinders will have higher confinement efficiency [46]. Therefore, the higher efficiency factor $k_1 = 4.1$ was used in this study. It will be seen later that this assumption is valid because FEA results reasonably match the test results.

Plug-in $k_1 = 4.1$ and $f'_{co} = 7.26$ ksi (50 MPa) into equations (4) and (5); it is found that $c = 1.8$ ksi (12.57 MPa) and $\Phi = 37.4^\circ$. Since the concrete is tightly confined, the dilatation is very small. In this study, the dilatancy angle Φ_f was assumed to be zero.

Non-linear Behavior of Concrete

A nonlinear structural analysis was performed by taking into account the nonlinear material behavior of the concrete. ANSYS performs the nonlinear analysis by employing the “Newton-Raphson” criterion. Using this approach, the load is subdivided into a series of load increments and applied over several load steps. It is important to ensure that the problem converges by using several features of the ANSYS like automatic load stepping, bisection, etc.

The uniaxial compressive stress-strain relationship for the concrete used in this study was constructed using the following procedure [51]:

$$\sigma = \frac{E_c \varepsilon}{1 + (\varepsilon / \varepsilon_o)^2} \quad (3)$$

$$\varepsilon_o = \frac{2 f'_{cc}}{E_c} \quad (4)$$

$$E_c = \frac{\sigma}{\varepsilon} \quad (5)$$

where, σ is the stress at any strain ε , ε_o is the strain at the ultimate compressive strength f'_{cc} , and E_c is the modulus of elasticity of concrete in the initial linear elastic region.

Boundary Conditions and Loading

The encased concrete cylinder was modeled in such a way that the axis of the cylinder coincides with a positive z-axis and the bottom face lies in the x-y plane of the global coordinate system. The following boundary conditions were applied to the finite element model:

- 1) The bottom face of the cylinder was fixed, i.e., all six degrees of freedom of the face were constrained.
- 2) The radial and circumferential displacements were constrained at the top face of the cylinder.
- 3) A uniaxial compressive pressure was applied on the top surface.

Enhancement of Fire Tolerance

Background

Although the lattice structure of the AGS tube gives it a unique edge, AGS tube encased concrete cylinder is as vulnerable to fire as its counterpart (i.e., traditional FRP tube confined concrete cylinder) because FRP is highly flammable. It is commonly acknowledged that fire hazards cannot be avoided in offshore drilling platforms, high-rise building, bridges, etc. Once AGS tube confined concrete cylinder is on fire, it will release smoke, heat, and toxic fumes. Additionally, the polymer matrix will burn and evaporate under high temperature. It will cause further decomposition of the fiber. As a result, the AGS tube will lose its confinement capacity, and the concrete cylinders will collapse. Therefore, AGS confined concrete cylinders cannot reach their full market potential unless their behavior under fire is fully understood and rational fire safety guidelines are established [52], [53].

Many efforts have been made to enhance fire tolerance or resistance of polymer materials such as introduction of fire retarding additives. Among all measures, one measure that is of particular interest is the incorporation of organically modified nanoclay. It has been proved that exfoliated and well-dispersed nanoclay can enhance both mechanical and fire resistance properties [54]. The purpose of this study was to investigate the fire tolerance of AGS tube confined concrete cylinders as a result of incorporating organically modified montmorillonite (MMT). A traditional fire retardant additive (TSWB®) was also considered for comparisons. Eight groups of specimens were prepared with various design variables. The fire test and uniaxial compression test were conducted to evaluate the fire tolerance and residual structural performance of each group of specimens. Some meaningful conclusions were obtained based on the systematic test program.

Raw Materials

DERAKANE® 510C-350 epoxy vinyl ester resin was provided by EDO Specialty Plastics. It is a brominated epoxy vinyl ester resin that has the highest degree of fire tolerance of all epoxy vinyl ester resins. It also has a high degree of resistance to mechanical and chemical damage. The hardener included 1.25 percent methyl ethyl ketone peroxide (MEKP) and 0.2 percent cobalt naphthenate (CoNap). Cloisite 10A nanoclay was provided by Southern Clay Products, Inc. The silicate platelets are 0.04 E-12 in. (1 nm) in thickness and 2.8×10^{-12} - 6×10^{-12} in. (70-150 nm) across. TSWB® Fire Retardant Additive was from Avtec Industries. The average particle size is around 28 μm . It is claimed that this additive is extremely effective at a proper loading against open flame and high radiant heat, even in severe fires with high velocity combustion fronts. The selected E-glass fiber roving came from Saint Gobain Vetrotex with 1,091.4 ksi (75.2 GPa) elastic modulus. The melting temperature

varies for each glass composition, but it is generally at about 2300 °F (1260°C). Holcim Type I Portland cement, gravel, natural sand, water, and DAVA 170 were used to prepare concrete. The mixture design followed the ACI (American Concrete Institute) Standard 211.1 (“Standard” 1991). The maximum nominal coarse aggregate size was ¾ in. (19.0 mm). The mixture ratio by weight for the concrete was cement: water: gravel: sand: admixture = 1: 0.51: 3.49: 1.88: 0.001. It was found through experiments that the 28-day cylinder compressive strength was 5.34 ksi (36.81 MPa), the modulus of elasticity was 5,181 ksi (35.97 GPa), and the Poisson’s ratio was 0.19.

Equipment

Two major pieces of equipment used for mixing VE and nanoclay (MMT) were the NETZSCH type 50 bench-top three-roll mill and Sonics VC750 ultrasonic generator. The amplitude of the ultrasonic generator was set to 40 percent, and the pause was set to 5 seconds every 20-second sonification. The MMT/VE mixture obtained after ultrasonic mixing was then pulled into the center roll of the three-roll mill, which was later transferred to the apron roll by adhesion. Dispersion was achieved through shear forces generated between adjacent rolls. The milled materials were then removed from the apron roll by a knife that runs against the roll.

The filament winding machine used in this study was the Little Hornet Winder (LHW), which was manufactured by McClean Andersons. The main components of LHW are a mandrel, horizontal carriage, tooling, and machine control system. It was operated by the pattern development software named Pattern Master II.

Specimen Fabrication

AGS Skeleton Fabrication. The AGS skeleton fabrication followed the same process as described in the automatic manufacturing and parametric study. The details of each group of AGS tubes are given in Table 7. This method offers good control over fiber placement and uniformity of the structure. The polymer used was the pure VE without any additives.

Table 7
Detail of AGS tube

Rib thickness in. (mm)	Width of axial ribs in. (mm)	Width of helical ribs (mm)	Angle of helical ribs with the hoop direction (°)	Bay area in ² (mm ²)
½ (12.7)	0.38 (10.0)	0.38 (10.0)	6.1	1.0 (645.2)

FRP Skin Fabrication. Since the skin was the layer directly exposed to fire, eight groups of skins were prepared with varying additives and mixing procedures; see Table 8. It is well known that nanoclay morphology has a significant effect on its physical/mechanical properties. Therefore, the mixing combination in Table 8 was determined based on a close observation of the nanoclay morphology. In this study, the morphology of nanoclay was examined using transmission electron microscope (TEM). Figure 40(a) shows the nanoclay morphology after 30-min mechanical blending + 1-h ultrasound + one pass of 3-roll mill; Figure 40(b) shows the nanoclay morphology after 30-min mechanical blending + 1-h ultrasound + one pass of 3-roll mill + 1-h ultrasound. Obviously, more nanoclay particles have been exfoliated in Figure 40(b) than in Figure 40(a). In order to further investigate the effect of the mixing effort on the nanoclay exfoliation, the nanocomposite in Figure 40(b) was further mixed by an additional pass of three-roll mill. The corresponding morphology is shown in Figure 40(c). Obviously, with the additional mixing effort, there is no further improvement in the morphology. Actually, it seems that the uniformity of the nanoclay distribution has been slightly reduced, possibly due to fracture of some exfoliated nanoclay sheets by the high shearing force of the three-roll mill. Therefore, it was decided that the mixing effort corresponding to Figure 40(b) should be used, as given in Table 8. For all the groups, a fixed fiber winding angle of 54.6° with the axial direction was used, and the thickness of the FRP skin was 0.2 in. (5 mm).

Table 8
Details of fabrication procedure for each group of specimens

Group name	Nanoclay content (wt. %)	Fire retardant content (wt. %)	Mixing procedure
A	—	—	—
B	1	—	30-min mechanical blending + 1-h ultrasound + 3-roll mill + 1-h ultrasound
C	—	30	Mechanical blending
D	1	30	Mixing nanoclay first as Group B and then mixing fire retardant as Group C
E	—	—	—
F	1	—	30-min mechanical blending + 1-h ultrasound + 3-roll mill + 1-h ultrasound
G	—	30	Mechanical blending
H	1	30	Mixing nanoclay first as Group B and then mixing fire retardant as Group C

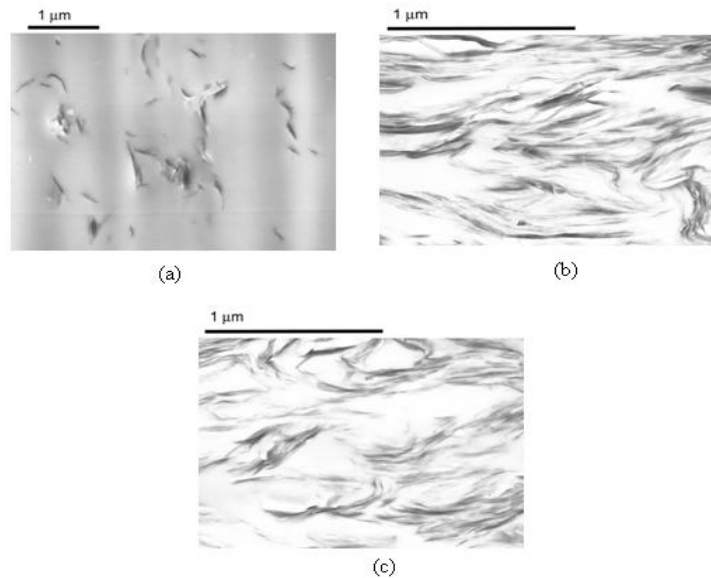


Figure 40
TEM image of nanoclay morphology in VE matrix with varying mixing effort embedded thermocouples

Groups A, B, C, and D were fire tested. In order to obtain the temperature distribution data, four thermocouples were fixed on the inner surface and the center for each AGS encased concrete cylinder before casting concrete. The location of each thermocouple is schematically shown in Figure 41. The thermocouples used were Omega XC-20-K-12, which could sustain a temperature of 2192° F (1200° C). The thermocouples had an insulated wire connection to external instrument for temperature measurement.

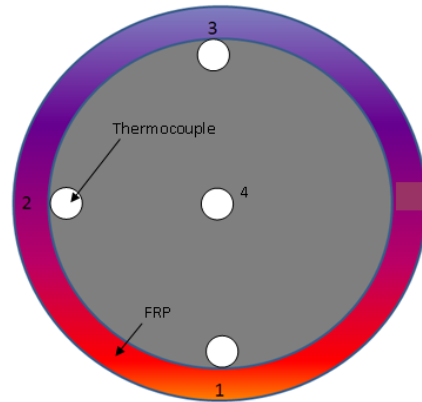


Figure 41
Schematic locations of embedded thermal couples

Concrete Casting. Before casting concrete, one end of the AGS tube was capped using a plastic sheet. The concrete was then cast, compacted, finished, and cured in a standard wet curing room with a relative humidity 100 percent for 28 days.

Fire Test and Uniaxial Compression Test

Fire Test. The fire test was conducted using a jet-flame burner and was fueled by a continuous gas supply from a liquid propane (LP) fuel tank. This burner can provide 1800°F (982°C) high temperature immediately. The specimen was hung up above the nozzle, as shown in Figure 42 [55]. According to the IMO Standard in Resolution A.753 (18), Groups A, B, C, and D were exposed to the fire for 5 minutes. The inside temperature was monitored by using the OMB-DAQ-55 device and Personal DaqView™ software. OMB-DAQ-55 device has a multi-function data acquisition module attached to PCs via Universal-Serial Bus (USB) and high-resolution, 22-bit A/D converter programmable inputs from +31 mV to +20 V scales.

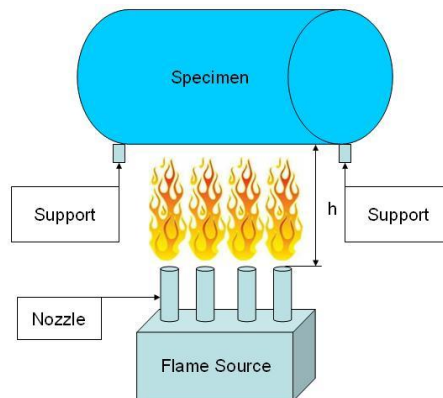


Figure 42
Schematic of the specimen exposure to the jet fire [55]

Uniaxial Compression Test. Each specimen from Group E, F, G, and H (control, without fire burning) and from fire tested Groups A, B, C, and D was evaluated using a uniaxial compression test to determine their compressive behavior and compressive strength. Each specimen was uniaxially compressed to about 40 percent of the unconfined concrete strength and unloaded to guarantee close contact between each component and to reduce errors in displacement measurement. Then, the specimen was reloaded until FRP failure. The compression tests were conducted using a FORNEY machine. This machine has a capacity of 604 kips (2,688 kN). The assembled computer data acquisition system can directly record the load-displacement curves. The compression test was conducted per ASTM C 39 standard. The loading rate was 0.03 ksi/s (0.23 MPa/s).

Engineering Economic Analysis

To evaluate the cost effectiveness of AGS tube encased concrete column, an engineering economic analysis is conducted in this project. The cost effectiveness of AGS tube confined concrete cylinders consists of several perspectives, such as material cost, installing cost, and long term maintenance cost. In order to compare with the traditional steel reinforced concrete column, two columns with identical size and load carrying capacity (one confined with AGS tube and the other reinforced with steel rebar), are considered in the current study.

DISCUSSION OF RESULTS

Literature Survey

Although a number of studies have been conducted on AGS structures and AGS reinforced concrete beams, slabs, and columns, there are no AGS tube encased concrete columns as proposed in our project. The concept proposed by Dutta et al. and Saafi is a structure that seems like the concept proposed in our study [10], [42]. Actually, there are fundamental differences between their concept with the proposed concept: (1) in their concept, the grid is used as a cage, providing internal reinforcement only. In the proposed study, the grid serves dual purposes (a) stay-in-place form during construction and (b) confinement during service. (2) The grid skeleton used by Dutta et al. and Saafi is stacked by the longitudinal FRP rods and hoop FRP rings. They are not grid structures in the real sense, i.e., without fiber interlacing at the nodes. In the proposed study, the ribs will be interlaced and will be actual grid tubes, and it is expected that the grid skeleton will provide better load transfer throughout the network.

Proof-of-Concept Study (Compressive Behavior)

Axial Stress-Axial Strain Behavior

Typical specific axial stress-axial strain behaviors of a circular AGS tube encased cylinder, a square AGS tube encased cylinder, a solid FRP tube encased cylinder, a solid steel tube encased cylinder, and an axial steel grid tube encased cylinder are shown in Figure 43. The test results of the solid FRP tube, solid steel tube, and axial steel grid tube encased cylinders are obtained by dividing the axial stress and axial strain by their respective tube weight of 2.2 lbs (1.32 kg), 11.20 lbs (5.08 kg), and 5.56 lbs (2.52 kg) [8].

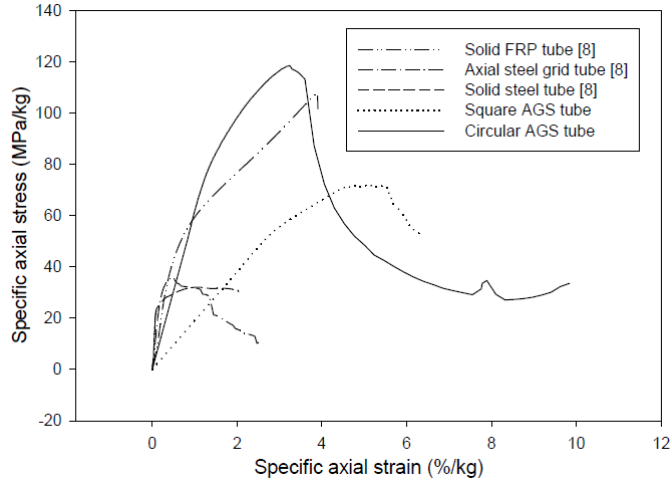


Figure 43

Comparison of specific axial stress-axial strain behavior of various types of tubes encased concrete cylinders

It is seen that the circular AGS tube encased concrete cylinder behaves differently from the solid FRP tube encased concrete cylinder. The axial stress-axial strain curve before the peak stress can be represented by a linear section followed by a non-linear section, instead of the typical bi-linear curve connected by a transition zone. The specific stress at the end of the linear section is about 4.95 ksi/lb. (75 MPa/kg), for the circular AGS cylinder. This value is much higher than that at the end of the first linear section which is about 1.98 ksi/lb. (30 MPa/kg) for the solid FRP cylinder. This suggests that the elastic region of the AGS tube encased concrete cylinder is enlarged. The confinement effect of the FRP can be utilized in structural design.

This type of behavior can be attributed to the unique confinement mechanism and composite action between the AGS tube and the concrete core. By filling fresh concrete into the AGS tube, the concrete flows into the holes or bays formed between and among the surrounding ribs. Once the concrete is cured, the concrete within the bays and surrounding ribs are mated, forming a mechanical interlocking. This type of physical interfacial connection is durable and permanent in nature and offers resistance to deformation. Unlike chemical adhesives, the mechanical interlocking does not degrade or age with time. Once the encased cylinder is loaded, both the concrete core and the AGS tube begin to expand laterally due to the Poisson's effect. However, the lateral expansion of the two components is not independent or free. On the contrary, the two components are mated or coupled because of the mechanical interlocking. As a result, they must adjust the pace of lateral deformation so that they can expand simultaneously and with the same rate. In another word, the AGS tube is engaged in carrying the applied load at the very beginning. The AGS tube is "actively" involved in carrying the load, instead of the passive confinement provided by the solid FRP tube.

Because of the early engagement of the AGS tube, the whole cylinder has a larger linear section before significant degradation of the concrete (cracking or crushing). As the damage within the concrete core increases, the stress-strain curve turns to a non-linear curve with a continuous reduction in stiffness (slope of the curve) until the peak stress is reached. Following the peak stress, there is a continuous drop in the stress with a considerable increase in axial strain. As opposite to the solid FRP tube encased concrete cylinder, which shows a total structural failure once the peak stress is reached, the axial stress does not drop to zero; instead, the stress keeps almost constant or even rebounds at some levels. This means that the AGS tube encased concrete cylinder has a considerable ductility. Once one rib fails, the load is redistributed to other ribs through the network connection.

The square AGS tube encased concrete cylinder and the axial steel grid tube encased concrete cylinder behaved similarly to that of the circular AGS tube encased concrete cylinder. The difference is that the axial steel grid cylinder has a higher stiffness in the elastic region probably due to the higher axial stiffness of steel than that of FRP. The axial stiffness of the square AGS cylinder is the lowest due to the larger lateral and thus axial deformation of the AGS tube caused by the stress concentration at the four sharp corners of the tube. For the solid steel tube confined cylinders, the specific strength is the lowest among all the encasing devices. This is due to the larger density of steel and the lack of mechanical interlocking between the tube and the concrete core.

Specific Compressive Strength and Ductility

From Figure 43, the specific compressive strength is the highest for the cylinder encased by the circular AGS tube, followed by the solid FRP tube, square AGS tube, axial steel grid tube, and solid steel tube. This means that if the same amount of materials is used, the circular AGS tube encased concrete cylinder will have the highest compressive strength. This comparison is more meaningful between the circular AGS tube and the solid FRP tube. Obviously, the circular AGS tube not only has a larger elastic region, but also has a higher ultimate specific strength. Actually, its ductility is also higher. This validates the idea proposed in this study, i.e., the circular AGS tube performs better than the circular solid FRP tube.

Comparing the circular AGS tube with the circular steel grid tube, it is seen that both the specific strength and ductility of the circular AGS tube are higher than those of the steel grid tube. This means that the AGS tube is more effective in confining the concrete core on the basis of the same weight of material. A noticeable difference between them is that the AGS cylinder shows a post-peak curve with a section of plateau or even rebound; while the steel grid cylinder shows a gradually descending post-peak curve. This difference may be because

of the different grid patterns. The bay is a square for the AGS tube, but it is a circle for the steel grid tube. The orthogrid pattern in the AGS tube may be more effective in distributing the applied load once some ribs fail.

Comparing the circular AGS tube with the square AGS tube, the square AGS tube shows a much smaller specific strength and ductility. This is understandable due to the stress concentration at the four sharp corners in the square AGS tube. The stress concentration causes premature rib failure and, thus, smaller specific strength and ductility.

The solid steel tube shows the smallest specific strength and ductility. This is again due to the larger density of steel and the lack of interfacial mechanical interlocking. It is interesting to note that the post-peak stress-strain curve is almost a horizontal curve. This is because the plastic flow of the steel, i.e., the steel tube provides an almost constant confining pressure once the steel yields.

Volumetric Strain Behavior

In order to understand the dilatation behavior of the encased cylinders, volumetric change with load provides useful information. The volumetric strain ε_v is determined from:

$$\varepsilon_v = \varepsilon_A + 2\varepsilon_H \quad (6)$$

where, ε_A (negative) and ε_H (positive) are the axial strain and hoop strain, respectively. For such a sign convention, a positive ε_v means dilatation and a negative ε_v suggests volume contraction.

Using the strain gauge measurement, Figure 44 shows the axial strain-volumetric strain behavior of two encased cylinders. One is a circular AGS cylinder and the other is a square AGS cylinder. It is seen that the volume of both cylinders experience a small volumetric contraction when the axial strain is small. Once the axial strain comes up to a certain value, the tendency reverses and shows volumetric expansion or dilatation. This represents a distinct departure from solid FRP tube encased concrete cylinders, where a volumetric contraction is seen [43]. During the testing, it was found that the failure started always from the thin skin. Once the skin fractured, the concrete within the bay area was significantly damaged (cracked or crushed) and flew out of the bay. Consequently, the ribs lost lateral support and mechanical interlocking. The axial ribs buckled and the compressive strain at the outer surface (where the strain gauge was pasted) was reduced, leading to a larger tensile strain in the hoop ribs. As a result of the reduced axial compressive strain (negative) and the increased hoop tensile strain (positive), a positive volumetric strain, i.e., volumetric expansion [which was determined by equation (6)], was detected. The buckling of the axial

ribs led to premature failure of the cylinder. Therefore, for this type of grid structure, the skin not only serves as a formwork during construction and a protection device during service, it also serves as a confining device to the concrete within the bay area. The skin needs particular consideration. It must be designed in such a way that the skin will continuously provide confinement to the concrete within the bay areas before the ribs fail.

Comparing the square AGS cylinder with the circular AGS cylinder, it is clear that the square cylinder demonstrates more volumetric expansion. This is because the stress concentration causes more premature failure of the skin in the square cylinder. The lack of confinement of the concrete in the bay area results in larger volumetric expansion.

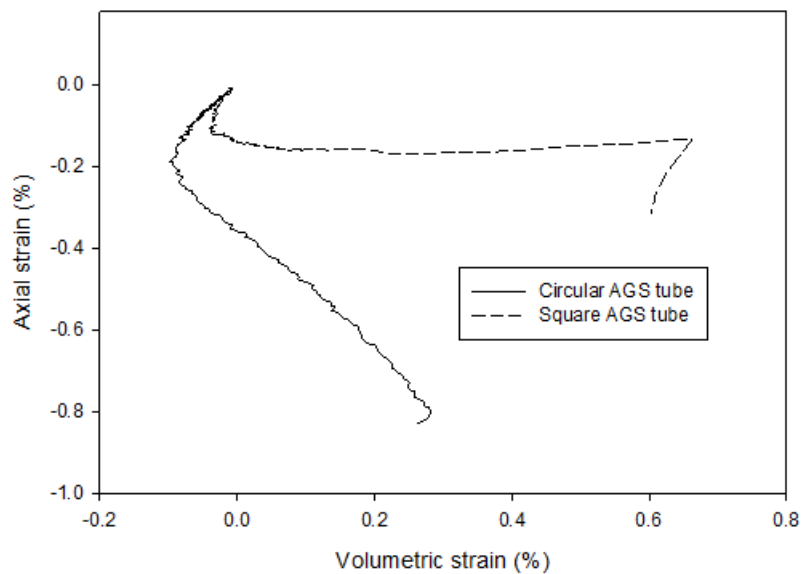


Figure 44
Change of volumetric strain with axial strain

Failure Mode

The failure modes of the circular AGS cylinder and the square AGS cylinder are shown respectively in Figure 45 (a) and (b). It was found during testing that the failure started from the skin for all specimens. This suggests that the two layers of FRP wraps are too thin to confine the concrete within the bay area. A thicker skin is needed. From Figure 45 (a), both the axial ribs and hoop ribs have fractured, close to the nodal area. The very even fractured surface suggests that the failure is due to shear stress. Each rib section between two nodes is like a short beam resting on an elastic foundation. The pressure applied to the ribs by the concrete core is so large that the transverse shear stress within the ribs exceeds the transverse shear strength of the ribs, leading to shear failure of the ribs. Because the shearing force is the largest at the nodes, the fracture occurs near the nodal area. It is also seen that a larger

number of axial ribs are fractured than hoop ribs. The reason is that the hoop ribs are subjected to the transverse bending force and the hoop tensile force. Because of the very large hoop tensile force and transverse shear force, the hoop ribs will be fractured first. Once one hoop rib is fractured, the axial ribs suddenly lose the constraint in the hoop direction. Together with the loss of support and mechanical interlocking from the concrete within the bay, the axial ribs behave like a one-end, built-in rod subjected to axial compression and transverse bending. Therefore, the axial ribs are easily fractured and not one, but the whole row of axial ribs in between the two fractured hoop ribs. This is exactly the case, as shown in Figure 45 (a). Therefore, the failure of ribs is a sequential event. It initiates by the fracture of hoop ribs and ends by a whole row of collapse of axial ribs.

For the square AGS cylinder, the failure is primarily due to the fracture of the hoop ribs at the corner, as shown in Figure 45 (b). This is due to the stress concentration at the sharp corner of the square AGS tube. Obviously, circular cylinders perform much better than square cylinders. In fact, square cylinders should be avoided if at all possible.



Figure 45
Failure mode of (a) circular AGS cylinder under compression and (b) square AGS cylinder under compression

Summary

An experimental program was conducted on a new type of AGS tube encased concrete cylinders. Based on the test results, the following conclusions are obtained:

- The AGS tube ensures that it is engaged in confining the concrete core once the load is applied. A constructive composite action between the concrete core and the AGS tube is developed due to the mechanical interlocking. The interlaced ribs confine the concrete core, and the concrete core protects the ribs from local buckling and crippling.

- Instead of a typical bilinear curve connected by a transition zone in the axial stress-strain curve, the AGS tube encased concrete cylinder behaves linearly elastic until the compressive stress is well above the unconfined compressive strength of concrete, followed by a non-linear curve until peak stress. Once one rib fails, the load is redistributed to other ribs through the network structure, without full disintegration of the cylinder.
- For the circular AGS tube encased concrete cylinder, the specific compressive strength and ductility are the highest among all the types of cylinders compared.
- Square AGS tube encased concrete cylinders show lower specific strength and ductility than the circular AGS counterparts. The use of square AGS tubes should be avoided if at all possible.
- The AGS tube encased concrete cylinders experience a small volumetric contraction when the axial stress is small; once the axial stress comes to a certain value, the cylinder undergoes a volumetric expansion until failure.
- The failure of the circular AGS tube is due to the hoop rib fracture, followed by the collapse of a whole row of axial ribs; the failure of the square AGS tube is due to hoop rib fracture under compression and axial rib fracture under bending.
- The skin is primarily responsible for confining the concrete within the bay; the interlaced ribs are mainly for confining the concrete core. The skin must be designed in such a way that it will not fracture before the ribs fail.

Proof-of-Concept Study (Bending Behavior)

Bending Strength and Ductility

Figure 46 shows the normalized transverse bending load-deflection curves from the four-point bending test. One was encased by the square AGS tube and the other was encased by the same size steel grid tube [44]. The weight, absolute peak load, and specific peak load of each beam are given in Table 9. Three observations can be made. (1) The AGS tube encased beam shows a linear elastic behavior up to the peak load, while the steel grid tube encased beam shows a linear section followed by a non-linear section with a continuous reduction in stiffness. This occurs due to the linear elastic behavior of the FRP and the elastic-perfectly plastic behavior of the steel. (2) The specific load and deflection of the AGS beam is higher than those of the steel grid beam. Together with the higher specific compressive strength and ductility, it is concluded that, using the same weight of materials, AGS tube encased cylinders will have a higher load carrying capacity and higher ductility than the steel grid tube encased concrete counterparts. (3) Both before and after the peak load, the AGS beam shows some fluctuations of load. This is because of the load redistribution through the grid network once the skin or some ribs fail.

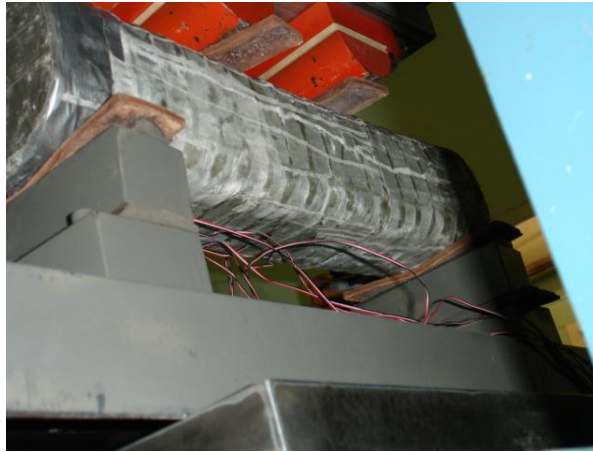


Figure 46
Four-point bending test

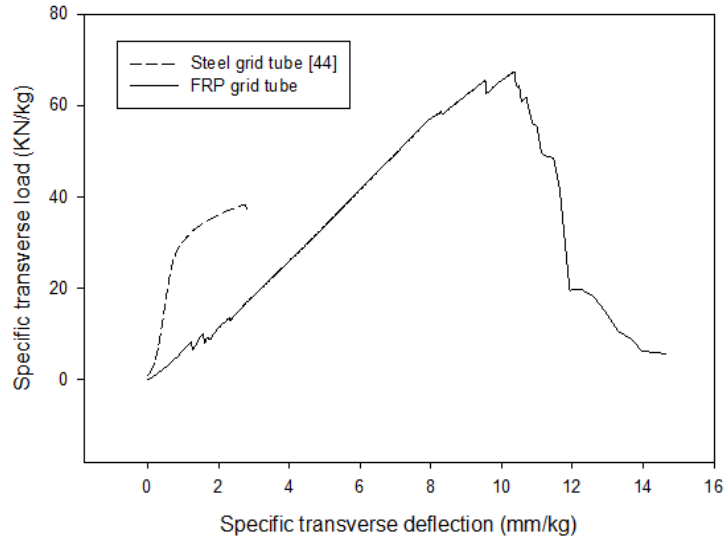


Figure 47
Comparison of FRP grid tube encased concrete beam with steel grid tube encased concrete beam under bending

Table 9
Absolute and specific peak bending load

Type of tube	Weight lb _m (kg)	Absolute peak load kips (kN)		Specific peak load kips/(kN/kg)	
		Average	Standard deviation	Average	Standard deviation
Steel grid tube [44]	14 (6.35)	54.4 (241.9)	16 (3.6)	373.8 (38.1)	13.7 (1.4)
FRP grid tube	2.9 (1.31)	19.8 (88.3)	11.1(2.5)	660 (67.3)	21.6 (2.2)

Failure Mode

A typical failure mode of the AGS beam is shown in Figure 47. Failure started with the fracture of the FRP skin at the bottom of the beam. The concrete crack initiated from the bottom close to the bottom roller and grew along the 45° direction, a typical shear failure mode. However, this 45° crack pattern was not followed all the way. When the crack came to the neutral plane, the crack turned to an almost vertical direction until the upper face. This particular failure mode is different from flexural failure mode and pure shear failure mode. The reason for this may be due to the complex stress condition in the encased beam. In addition to the traditional normal stress in the longitudinal direction and the shear stress in the transverse direction for an unconfined beam under a four-point bending load, the encased beam also developed a hoop (or transverse) tensile stress due to the confinement provided by

the grid tube to confine the volumetric expansion of the concrete in the compression zone.

Summary

An experimental program was conducted on a new type of AGS tube encased concrete beam. A finite element analysis was also conducted to understand the effect of various parameters on the structural behavior of circular AGS FRP tube encased concrete cylinders. Based on the test results and finite element modeling, the following conclusions are obtained:

- The specific bending strength and ductility are higher for the AGS beam than those for steel grid tube encased counterpart. It is envisioned that AGS tube encased concrete cylinders have a sufficient capacity to carry an eccentric axial compression load due to the interfacial mechanical interlocking and, thus, better stress transfer between the AGS tube and the concrete core.
- The failure mode is different from the flexure failure mode and shear failure mode. The crack started from the bottom of the beam near the bottom roller similar to a shear failure mode. However, the crack turned into a vertical crack once it reached the neutral plane. It is believed that the complex stress condition leads to the unique failure mode.

Automatic Manufacturing and Parametric Study (Manufacturing and Compression Testing)

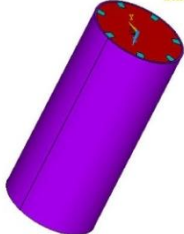
Development of Composite Action

The test results of the peak compressive load from Groups 9, 10, and 1 are summarized in Table 10. Also given in Table 10 is the peak compressive load of pure concrete cylinders having a diameter of 4.5 in. (114.3 mm) and Group 1 is AGS tube encased concrete cylinders. From Table 10, the development of the composite action in a building-block manner can be observed. The total peak load of the two building blocks (skin and grid skeleton) is 12.2 kips (54.4 kN) + 22.3 kips (99.1 kN) = 34.5 kips (153.5 kN), which is smaller than the peak load of the integrated structure (the skin wrapped grid tube), 44.5 kips (198.1 kN). This means that a positive composite action has been developed between the FRP skin and the FRP grid skeleton. The skin protects the grid skeleton from global/local buckling and crippling; the grid skeleton resists the buckling of the skin by providing both axial and hoop reinforcement.

Again, the total peak load of the two building blocks (pure concrete cylinder and the AGS tube) is 106.5 kips (474.1 kN) + 44.5 kips (198.1 kN) = 151.0 kips (672.2 kN), which is much smaller than the integrated cylinder (AGS tube encased concrete cylinder), 463.1 kips

(2060.7 kN). Similarly, the reason for the positive composite action is due to the fact that the AGS tube confines the concrete core, and, the concrete core protects the AGS tube from global/local buckling and crippling.

Table 10
Schematic of the load carrying capacity of the composite elements

Structure name	Peak load kips (kN)	Schematic
Skin	12.2 (54.4)	
Grid skeleton	22.4 (99.1)	
AGS tube	44.5 (198.1)	
Pure concrete cylinder	106.5 (474.1)	
AGS tube encased concrete cylinder	463.1 (2060.7)	

Actually, the positive composite action is not only exhibited by the peak load, but also by the peak stress and ductility. Figure 48 shows the axial stress-axial strain behavior of all the five types of cylinders given in Table 10. It is clear that the AGS tube has a much higher ductility than its two building blocks (skin and grid skeleton). Of course, the peak stress of the AGS tube is smaller than that of the grid skeleton. However, this does not mean that the composite

action between the grid skeleton and the skin is not positive. The reason for this is that the failure of the AGS tube was initiated by the skin, followed by the grid skeleton. Once the skin failed, the load was shifted to the grid skeleton. However, when the stress was calculated in Figure 48, the cross-sectional area of the whole cylinder (skin + grid skeleton) was used. This is why the nominal peak stress of the AGS tube in Figure 48 is smaller than the peak stress of the grid skeleton. If the true cross-sectional area of the grid skeleton was used to calculate the stress after skin failure, the peak stress in the AGS tube would be about 34.7 ksi (239 MPa). This number is much higher than the peak stress of the pure grid skeleton 17.4 ksi (about 120 MPa) in Figure 48. This suggests that the skin protects the grid skeleton from buckling failure, a solid evidence of the positive composite action between the skin and the grid skeleton.

For the system of the AGS tube encased concrete cylinder and its two building blocks (the concrete core and the AGS tube), it is clear that the AGS tube encased concrete cylinder has a higher peak stress than its two building blocks. It seems that the ductility of the AGS tube confined concrete cylinder is smaller than that of the AGS tube. The reason is that the stress controlled uniaxial compressive testing stopped automatically before the post-peak branch was fully developed for the AGS tube confined concrete cylinder due to some default settings of the machine. Actually, it is clear from Figure 48 that the stress starts to rebound at the end of the stress-strain curve, suggesting that there should have been a longer post-peak branch to follow for the AGS tube confined concrete cylinder. Therefore, it is reasonable to assume that the ductility of the AGS tube confined concrete cylinders is also higher than its building blocks. The increase in both peak load and peak stress (load carrying capacity) and ductility (toughness and energy absorption) suggests that the AGS tube encased concrete cylinders have a foreseeable potential in infrastructure, particularly in harsh environments such as corrosion, earthquake, hurricane, overload, etc.

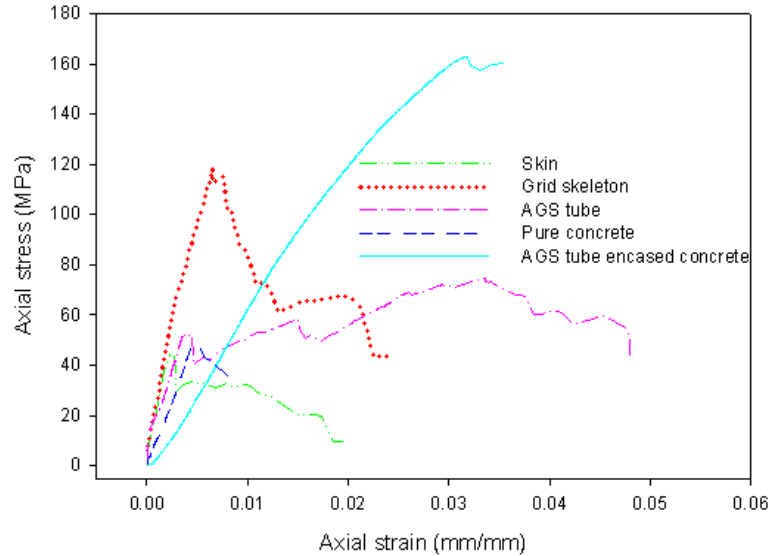


Figure 48
Axial stress-strain behavior of various cylinders

Effect of Design Parameters on the Structural Behavior of AGS Tube Encased Concrete Cylinders

Variation of Rib Thickness. Increasing the rib thickness enhances the load carrying capacity of the cylinders. The thicknesses of the ribs that were investigated during the experiments were ¼ in. (6.4 mm), ½ in. (12.7 mm), and ¾ in. (19.0 mm), (Groups 2, 1, and 3 in Table 4). Their corresponding peak compressive load was 406.6 kips (1809.3 kN), 463.1 kips (2060.7 kN), and 497.9 kips (2215.8 kN), respectively. The cylinder with the largest thickness was able to withstand more loads when compared to other cylinders. However, it is observed that this increase in load carrying capacity is not a linear function of the rib thickness. The rate of increase reduces as the rib thickness increases. This suggests that further thickening the ribs will reduce its confinement efficiency. Therefore, there might have an optimal combination of the AGS tube and the concrete in terms of strength, stiffness, and dimension.

Variation of Bay Area. Cylinders with bay areas of 1 in² (645.2 mm²), 2.19 in² (1415.6 mm²), and 4 in² (2580.6 mm²), (Groups 6, 1, and 7 in Table 4) were fabricated for experimental testing. Their corresponding peak compressive load was 476.7 kips (2120.4 kN), 476.5 kips (2060.7 kN), and 388. kips (1726.5 kN), respectively. This suggests that the load carrying capacity of the cylinders decreases with the increase in the bay area. Besides the reduction in the amount of FRP materials used as the bay area increases, a possible reason for this is that the confinement to the concrete within the bays by the ribs becomes weaker. As a result, the concrete within the bays will be easily damaged (cracked and

crushed), which provides a “hole” for the concrete core to damage and to flow into it. The suitable bay area may also depend on the maximum aggregate size, which determines the composition of the concrete within the bay. If the aggregate size is larger than the bay, only fine aggregates or mortar can flow into the bay during construction, which may reduce the strength of the concrete inside the bay.

Since the change of the bay area leads to the change in the helical rib angle, as given in Table 4, the effect of the bay area can also represent the effect of the helical angle. Obviously, the higher the helical angle, the lower the confinement efficiency. This is true because higher helical pitch results in less strength in the hoop direction.

Variation of Skin Thickness. During fabrication, cylinders were manufactured with three skin thicknesses, 0.11 in. (2.8 mm), 0.16 in. (4.10 mm), and 0.22 in. (5.6 mm), (Groups 4, 1, and 5 in Table 4). The corresponding peak compressive load was 439.2 kips (1954.6 kN), 463.1 kips (2060.7 kN), and 488.7 kips (2174.7 kN), respectively. The test results show that the load carrying capacity of the cylinders increases with the increase in the skin thickness. This suggests that the skin not only serves as a stay-in-place formwork during construction, it also plays an important structural role, i.e., confining the grid skeleton and the concrete within the bays, similar to the findings previously [8], [46]. However, it is noted that the role played by the skin cannot be overestimated. If the skin is too thick, the skin will become the primary confinement device. The grid skeleton will become shear connectors, instead of a confinement device. In the proposed concept, the primary confinement should be provided by the grid skeleton, not the skin. There might have been an optimal combination of the skin and the grid skeleton in terms of strength and stiffness in order to ensure that the cylinder work towards the proposed direction.

Variation of Skin Fiber Orientation. Comparing Groups 1 and 8 in Table 4, it is seen that the fibers oriented more towards the axial direction in Group 8 than in Group 1. The test results show that the peak load of the Group 1 tube encased concrete cylinder is 463.1 kips (2060.7 kN), while the result from Group 8 is 490.0 kips (2180.6 kN). This suggests that the skin fiber orientation has a considerable effect on the load carrying capacity of the encased concrete cylinders. The reason for this is that as more fibers in the skin align towards the axial direction, the axial stiffness of the skin increases and becomes close to that of the grid skeleton, leading to a more compatible working environment of the two components.

Comparison of the Confinement Effectiveness between the Grid Skeleton and the Skin. The effectiveness of the grid skeleton and the skin in confining the concrete core can be compared based on the test results. Based on the dimensions of the AGS tube and the compressive test results, it can be calculated that the confinement efficiency (the ratio of the increment in the peak compressive load over the increment in the volume of the FRP materials) is 736 kip/ft^3 ($1.16 \times 10^{-3} \text{ kN/mm}^3$) when the rib thickness is increased from $\frac{1}{4}$ in. (6.35 mm), (Group 2), to $\frac{1}{2}$ in. (12.7 mm), (Group 1); this number becomes 460 kip/ft^3 ($7.23 \times 10^{-4} \text{ kN/mm}^3$) when the rib thickness is increased from $\frac{1}{2}$ in. (12.7 mm), (Group 1), to $\frac{3}{4}$ in. (19.0 mm), (Group 3). For the skin, the confinement efficiency is 368 kip/ft^3 ($5.78 \times 10^{-4} \text{ kN/mm}^3$) when the skin thickness is increased from 0.11 in. (2.73 mm), (Group 4) to 0.16 in. (4.10 mm), (Group 1); this number becomes 396 kip/ft^3 ($6.22 \times 10^{-4} \text{ kN/mm}^3$) when the skin thickness is increased from 0.16 in. (4.10 mm) (Group 2) to 0.22 in. (5.47 mm), (Group 5). The average confinement efficiency is $9.47 \times 10^{-4} \text{ kN/mm}^3$ for increasing the rib thickness from $\frac{1}{4}$ in. (6.35 mm) to $\frac{3}{4}$ in. (19.0 mm); the average confinement efficiency for increasing the skin thickness from 0.11 in. (2.73 mm) to 0.16 in. (5.47 mm) is 392 kip/ft^3 ($6.0 \times 10^{-4} \text{ kN/mm}^3$). Obviously, for the AGS tubes fabricated in this study, the confinement efficiency of thickening the ribs is about 1.58 times that of thickening the skin. The grid skeleton is more efficient in confining the concrete core than the skin. Therefore, thicker ribs with thinner or moderate skin would be an ideal combination of this type of confining device.

Local Stress-Strain Distributions. The typical local stress-strain distributions for Group 1 specimen are shown in Figure 49. The stress was obtained based on the strain gauge measurements per the laminated plate theory [45]. Two observations can be made: (1) The in-plane shear stress on the surface of the skin is negative and is very high. This suggests that the failure of the skin may start from in-plane shear induced failure. (2) The stress-strain in the nodes behaves linearly elastic in both the hoop and axial directions. Also, the hoop tensile stress is very high and may be close to the tensile strength. This suggests that failure of the grid skeleton may start with the tensile failure of the helical ribs at the nodes.

Failure Mode. During the compression testing, it was observed that the failure of almost all the encased cylinders started from the skin. Once the skin failed, the load was redistributed to the grid skeleton. It was then observed that the rib failure started from the helical ribs at the nodes. Once the helical ribs fractured, the axial ribs lost lateral support from the helical ribs and they became rods clamped at one end and free at the other end (the end at which the helical rib had fractured).

This boundary condition resulted in the failure of the axial ribs by crippling or brooming. Figure 50 shows a typical failure mode of the ribs and the concrete cracks within the bay.

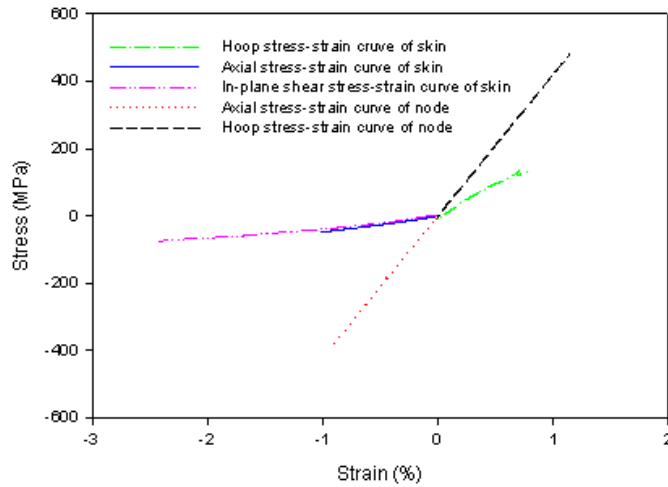


Figure 49
Local stress-strain distributions



Figure 50
Failure mode

Comparison with Regular FRP Tube Encased Concrete Cylinders. The better performance of AGS tubes over regular laminated FRP tubes can be validated by the existing confinement model. Based on the dimensions of a Group 1 specimen, it is calculated that, if the AGS tube (skin and grid skeleton) is smeared into a laminated FRP tube, the equivalent wall thickness of the laminated tube will be about 0.32 in. (8.04 mm). Assuming that the laminated tube has all the fibers oriented along the hoop direction (the perfect tube to provide confinement), the ultimate compressive strength of the encased concrete cylinder can be estimated based on the following confinement model:

$$f'_{cc} = f'_{co} + kf_r \quad (7)$$

$$f_r = \frac{2tf_{FRP}}{D} \quad (8)$$

where, f_{cc} is the confined compressive strength of concrete; f_{co} is the unconfined compressive strength of concrete; t is the wall thickness of the FRP tube; f_{FRP} is the hoop tensile strength of the FRP tube; and D is the diameter of the FRP tube.

Various researchers have proposed the confinement effectiveness factor k . Lam and Teng proposed two models: one is $k = 2.0$ and the other is $k = 3.3$ [47], [48]. Based on the two models, the confined compressive strength using the smeared FRP tube [($t = 0.32$ in. (8.04 mm), $D = 4.5$ in. (114.3 mm), $f_{FRP} = 31.9$ ksi (220 MPa), and $f_{co} = 7.3$ ksi (50 MPa)] is: $f_{cc} = 16.2$ ksi (111.9 MPa), ($k = 2$), and $f_{cc} = 22.1$ ksi (152.1 MPa), ($k = 3.3$). Obviously, even for this ideal laminated FRP tube, the ultimate confined compressive strength is still smaller than that confined by its AGS tube counterpart, which yields a confined compressive strength of 23.5 ksi (161.6 MPa).

Summary

From the above extensive experimental program, the following conclusions are obtained:

- The pin guided system and the collapsible mandrel, along with the 2-axis filament winder, can be used to fabricate AGS tubes automatically.
- The building-block test results show that a positive composite action exists between the grid skeleton and the skin and between the AGS tube and the concrete core. These structural components work collaboratively in carrying the applied load.
- The confinement effectiveness of the AGS tube is higher than its corresponding laminated FRP tube with the same amount of FRP materials.
- The skin may fail due to the high in-plane shear stress and the rib may start failure due to the high hoop tensile stress at the nodes.
- The test results show that the grid skeleton is more efficient than the skin in confining the concrete core. Thicker ribs and thinner skin may be an ideal structural combination.

Automatic Manufacturing and Parametric Study (Manufacturing and Push-out Testing)

Push-out Test of FRP Encased Concrete Tube

Group A and B were regular FRP tube encased concrete cylinders. A total of six specimens experienced the axial push-out test. It is observed that the concrete core was pushed out of the FRP tube to about 1.57 in. (40 mm), as shown in Figure 51 and Figure 52. Traditional push-out shear stress/strain curve is shown in Figure 53. Comparing Group A and B, it is seen that Group B has higher shear strength, 0.39 ksi (2.64 MPa), than Group A, 0.30 ksi (2.08 MPa). Additionally, Group B has higher ductility than Group A, possible due to the higher confinement provided by the thicker Group B FRP tubes.

The interface between the concrete core and the FRP tube were connected only by a physical bond. Therefore, when the interface experienced shear stress, the physical bond was easily broken, pushing the concrete column out of the FRP tube. Of course, it is noted that the FRP tube provided considerable normal pressure to the concrete core through confinement. This occurred due to the lower stiffness of the concrete core and, thus, a larger lateral (radial) expansion of the concrete core due to Poisson's ratio effect. The lateral expansion is confined by the FRP tube, thus a considerable normal pressure is applied to the concrete/FRP interface, leading to higher shear resistance. If a higher strength concrete is used, such as 11.9 ksi (82 MPa), the shear strength would be much smaller [6].



Figure 51
Specimens of Group A after push-out test



Figure 52
Specimens of Group B after push-out test

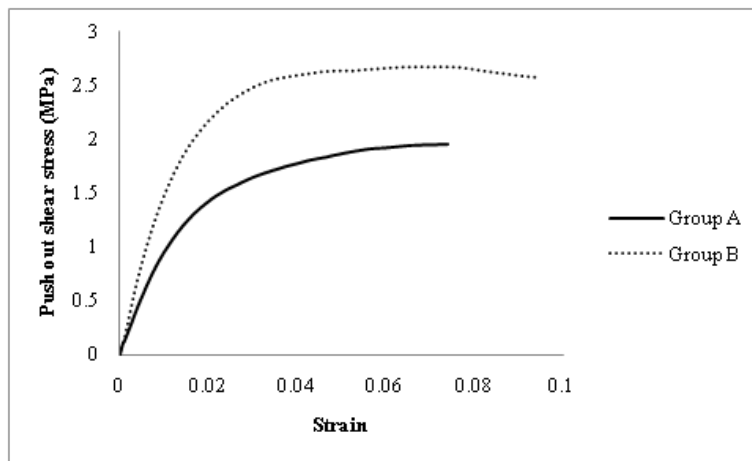


Figure 53
Shear stress/strain curve of Group A and B

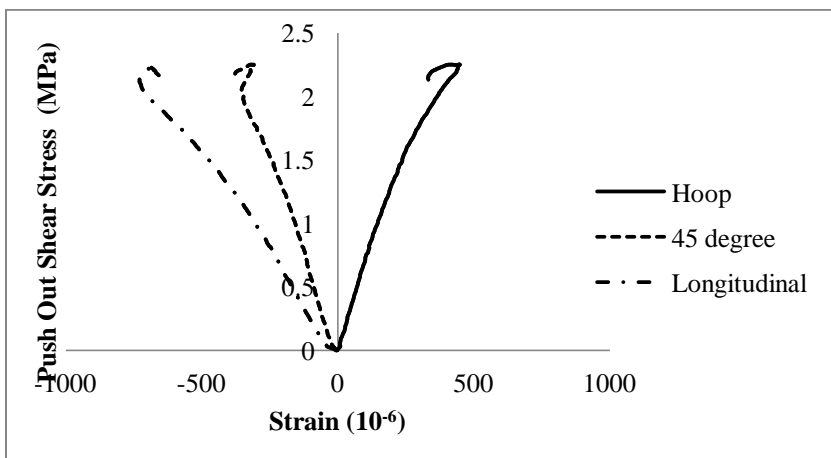


Figure 54
Stress/strain curve from the strain gauges on the skin of FRP

There strain gauges were attached along the hoop, 45°, and longitudinal directions, and the data were collected by the DAQ DC-100 system. The stress/strain curve of Group A is shown in Figure 54. It is seen that strain in 45° and longitudinal directions is negative and positive in the hoop direction. It is also seen that the absolute value of longitudinal strain is larger than the hoop strain and the hoop strain is larger than the 45° strain. The positive hoop strain suggests that the FRP tube has provided considerable confinement to the concrete core, leading to very high interfacial shear resistance.

Push-out Test of AGS-FRP Tube Encased Concrete Cylinders

Groups C, D, and E are AGS-FRP tube encased concrete cylinders, and a total of 15 specimens experienced the push-out test. Comparing Groups C, D, and E, it is observed that the concrete was not pushed out of the AGS-FRP tubes for Groups C and D, as shown in Figure 55. It is also observed that the concrete core was pushed out of the Group E; see Figure 56.



Figure 55
Failure mode of Group D



Figure 56
Failure mode of Group E

The stress/strain curve is shown in Figure 57. Comparing the hoop direction, the tensile strain on the FRP skin is larger than that on the rib, while the longitudinal strain is almost the same on the FRP skin and on the rib.

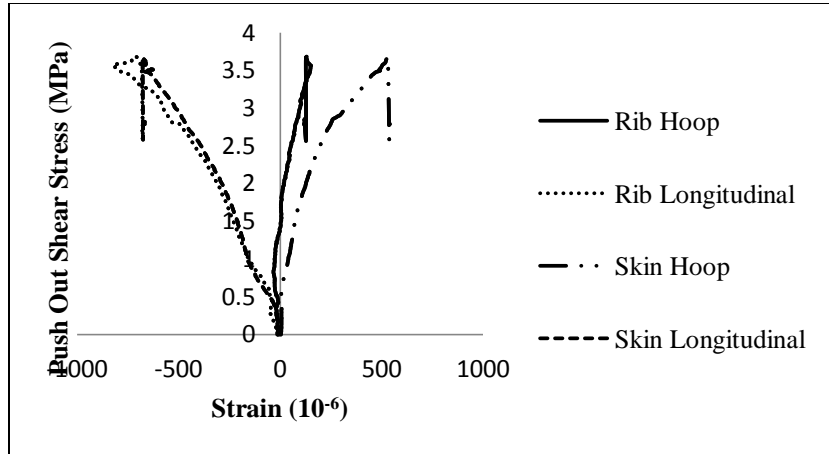


Figure 57
Stress/strain curve from stain gauge

Push-out Strength and Failure Mode

Comparing Groups A and B, C, and D in Figure 58, it is observed that the shear stress was increased as the thickness of the FRP skin increased. Also the shear stress was increased as the thickness of the FRP rib increased. However, as the thickness of the rib increased, such as Group E, the stress in the concrete teeth also increased, similar to a cantilever beam. For the lower strength concrete used in this study, the concrete shear strength was not sufficient to balance the shear stress, leading to concrete teeth shear failure and lower shear strength.

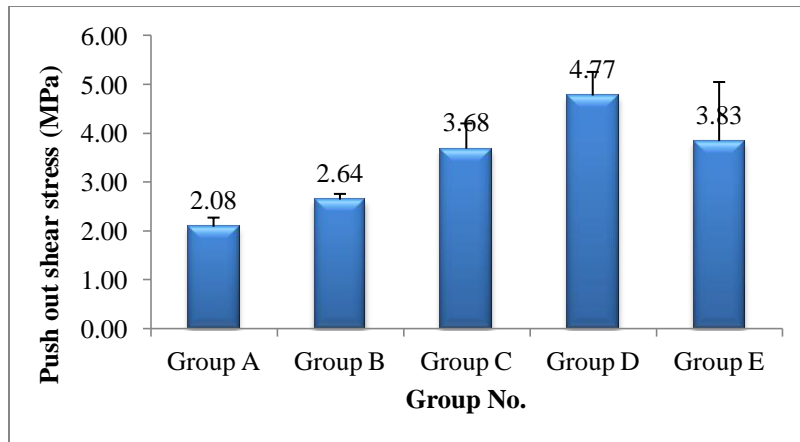


Figure 58
Comparing the shear stress of Group A to E

Comparing the push-out stress/strain curve of Groups A to E in Figure 59, it is observed that Group D has the highest shear strength around 0.69 ksi (4.77 MPa), and the shear strength of

Group E is 0.56 ksi (3.83 MPa); however, it is still larger than that of the Groups B and A. Therefore, even for the lower strength concrete used in this study, which is unfavorable for displaying the mechanical interlocking effect, the AGS tube still provides higher shear resistance than traditional FRP tubes.

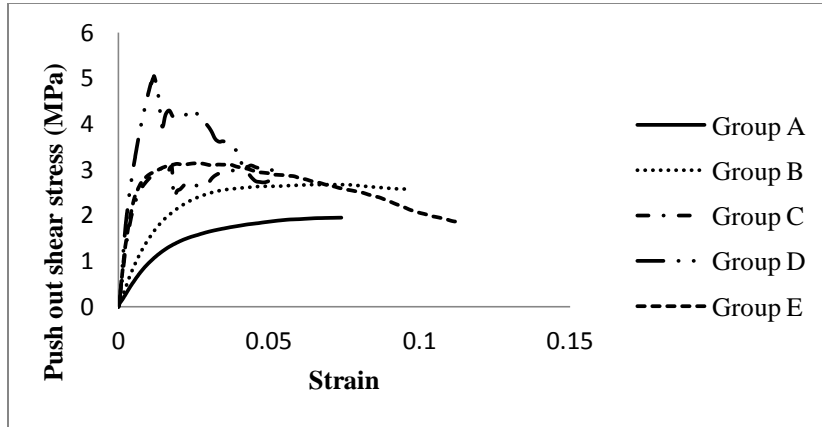


Figure 59
Stress/strain curve of Groups A to E

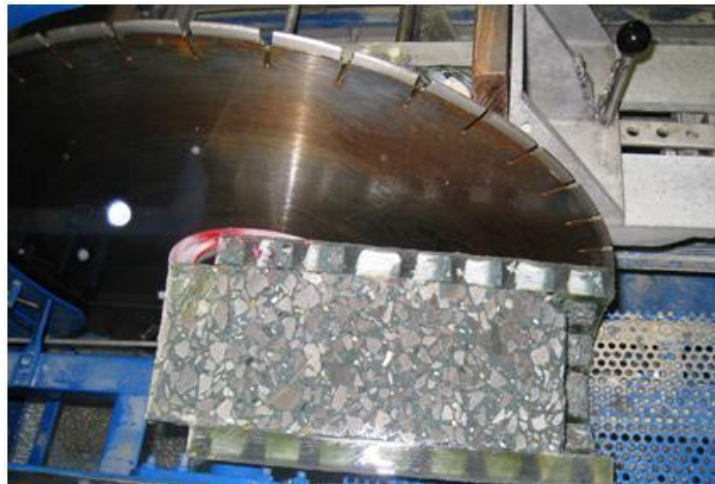


Figure 60
Specimen cut by diamond saw

After the push-out test, all specimens were cut by a diamond saw, as shown in Figure 60. Comparing Groups C and D in Figure 61 (a) and (b), it is observed that the concrete was filled into the bays in the grid. The bonding condition between the FRP grid and the concrete teeth was very good and no cracks were observed between them. The fracture is observed to be at the top of the AGS tube. The concrete teeth were not broken by shearing load during the push-out test.

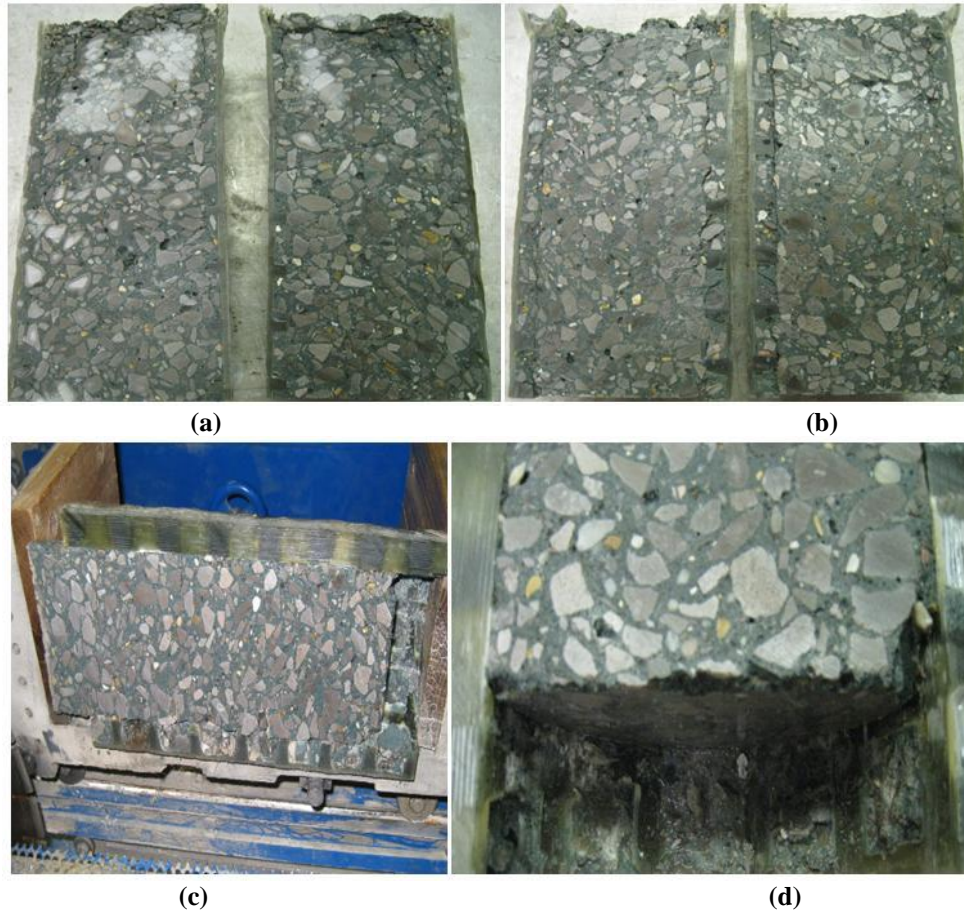


Figure 61
(a) Group C, (b) Group D, and (c and d) Group E

Examining Figure 61 (c) and (d), it is observed that the concrete teeth were cut off by shearing force during the push-out test. It is also observed that a crack was created at the root of each concrete tooth.

Summary

The test results show that the interfacial shear strength of the AGS tube encased concrete cylinders are higher than that of the regular FRP tube encased counterparts, regardless of the same materials or the same wall thickness of the FRP tubes. Due to the lower strength and stiffness of the concrete used, however, the regular FRP tube confined concrete cylinders show a higher shear resistance than with higher strength concrete. It is also observed that the key for the AGS tube to display its confining efficiency is to ensure that the concrete teeth shear failure occurs after concrete compressive failure; otherwise, the mechanical interlocking cannot be ensured and the confining effect cannot be fully displayed. In order to do this, it is suggested that the higher compressive strength or higher shear strength concrete must be used.

Finite Element Modeling

FEA (Finite Element Analysis) Validation

The computational time of the encased concrete cylinders was relatively long because of the nonlinear behavior of the concrete. This nonlinear behavior of the concrete was accounted for in the FEA model as explained in previous sections. The crushing and cracking of the concrete can be plotted using one of the post-processing features of ANSYS. Figure 62 shows the crushing and cracking of the concrete wherein the circles suggest the concrete has cracked and octagons suggest the concrete has crushed. Figure 63 (a) – (c) shows the stress distribution in the concrete core, the skin, and the grid skeleton for a Group 1 AGS tube encased concrete cylinder, respectively. In order to use the FEA as a design tool and to conduct parametric study, the model must be validated against test results.

Figure 64 shows the comparison of the axial stress-strain curves of an AGS tube encased concrete cylinder obtained from the experiment and FEA. The experimental specimen used here was from Group 1. From Figure 64, the linear portions of both curves almost follow the same path. As the load increases, the FEA curve deviates from the experimental curve but the error is within engineering accuracy. This suggests the reliability of the FEA to model the encased concrete cylinders. Of course, the model is more reliable in the elastic zone than in the plastic deformation zone.

Figure 65 shows another comparison. The specimen used in this case was from Group 6. The results show a similar trend to that observed in Figure 64. This further validates the reliability of the FEA model. It also validates that the inputs for the FEA model such as the elastic properties of the FRP, the non-linear stress-strain relationship for concrete, the parameters for the Drucker-Prager criterion, etc. are acceptable.

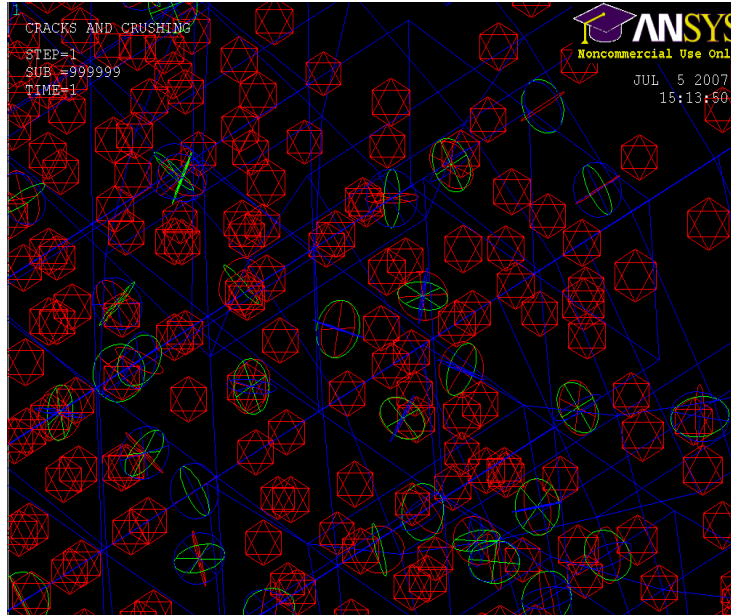
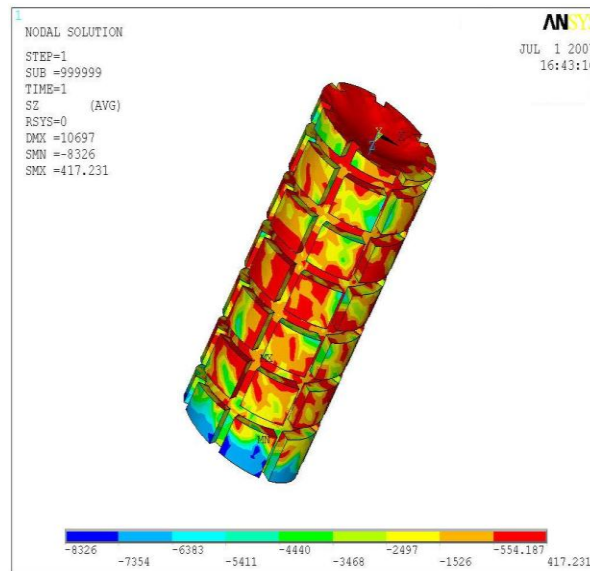
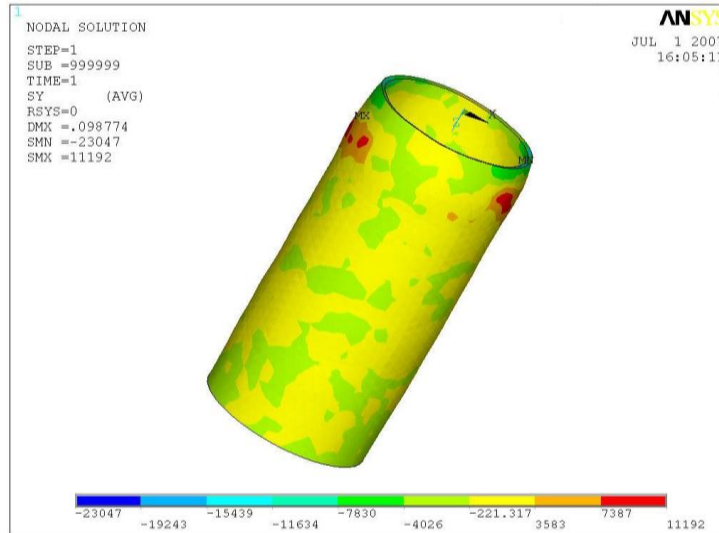


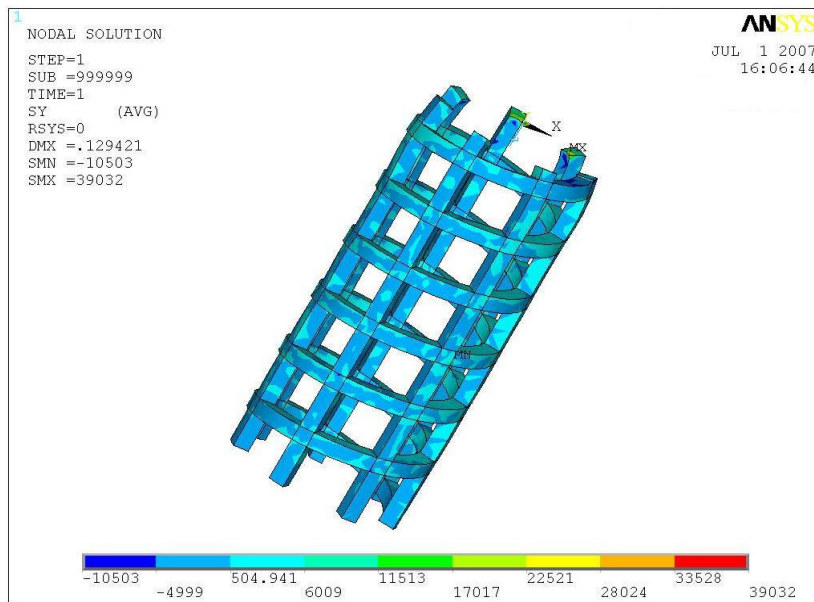
Figure 62
Crushing and cracking of the concrete



(a) Stresses developed in the concrete core



(b) Stresses developed in the skin



(c) Stresses developed in the grid skeleton

Figure 63
Stress developed in each component in a Group 1 AGS tube encased concrete cylinder

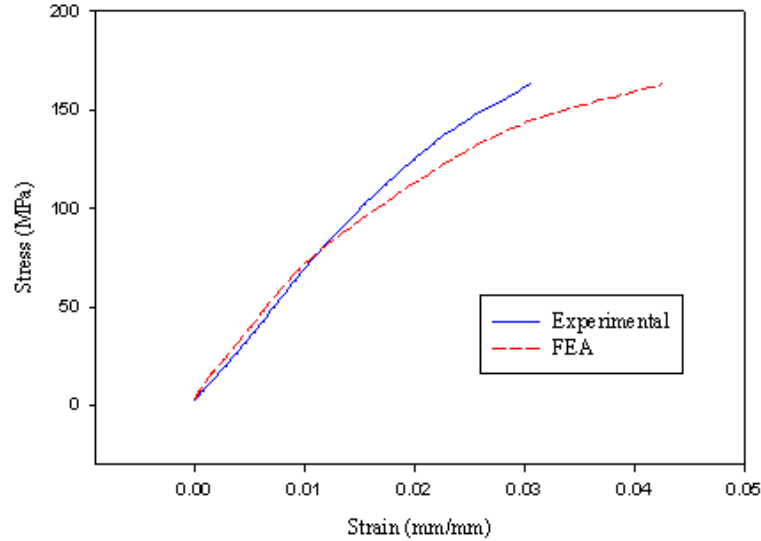


Figure 64
Axial stress-strain graphs for a Group 1 AGS tube encased concrete cylinder

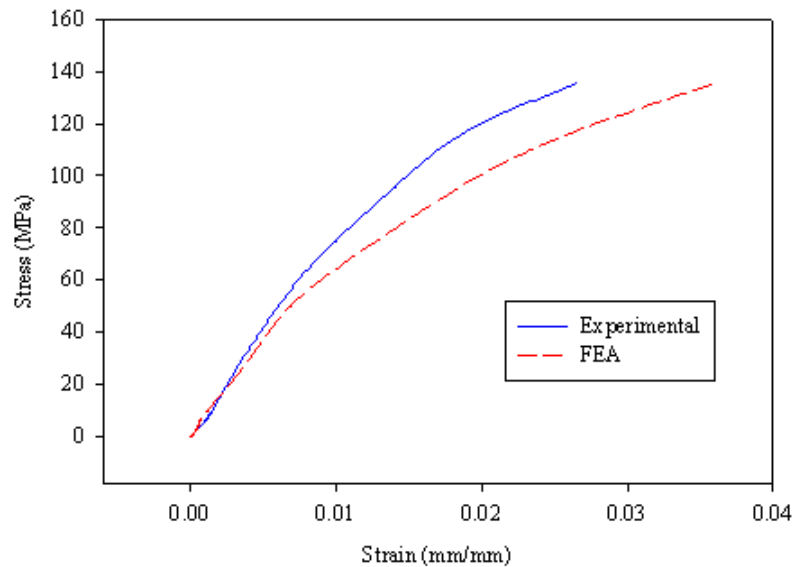


Figure 65
Axial stress-strain for a Group 6 AGS tube encased concrete cylinder

Parametric Analysis

Because the FEA model has been validated, it can be used to conduct a parametric study. All the analyses were conducted by keeping the amount of materials used as constant. Hence, this type of study may lead to an optimized design of the AGS tube encased concrete cylinders. In the following analyses, the skin thickness was kept constant 0.16 in. (4.10 mm), and the fiber orientation was fixed at 10° . The following variables were identified as important and their effect on the structure's performance was analyzed: (1) axial stiffness of the skin, (2) rib thickness, and (3) bay area.

From experiments, it has been found that the failure of the encased cylinder is controlled by the AGS tube, specifically by the hoop tensile stress; see Figure 44. Therefore, in the following parametric study, the maximum hoop tensile stress is selected as an indicator of the effect of each design parameter on the structural performance of the confined concrete cylinders.

Effect of the Skin Axial Stiffness

The effect of the axial modulus of the skin on the load carrying capacity of the AGS tube encased concrete cylinder was investigated. From Figure 66, the maximum hoop stress in the cylinder reduces or the structural capacity of the cylinders increases with the increase in the modulus of the skin. This suggests that increasing the axial modulus of the skin allows the skin to share more load and increase the efficiency of the overall structure. This result is in agreement with the test results. From the test, the skin with a fiber orientation of 35° leads to a higher peak load than the skin with a fiber orientation of 10° .

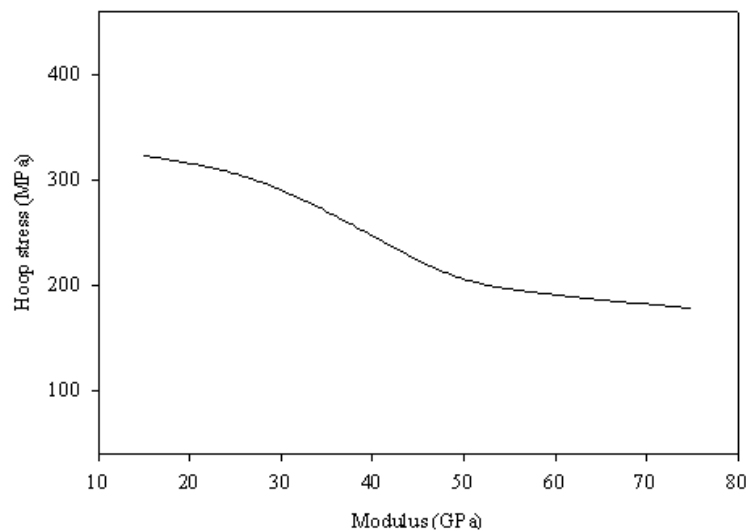


Figure 66
Effect of skin axial stiffness on the maximum hoop stress in the AGS tube

Effect of Rib Thickness

Figure 67 shows the effect of the rib thickness on the load carrying capacity. The maximum hoop stress of the cylinder decreases with the increase in the rib thickness. It can be seen that the load carrying capacity of the encased cylinder increases almost linearly with the increase in rib thickness until some point. Further increasing of the rib thickness will lead to a decrease in the efficiency. Hence, the structural behavior of the AGS tube encased concrete cylinders is complex. It not only depends on each individual structural component (skin, grid skeleton, and concrete core), but it also depends on the compatibility among them. They must

have compatibility in strength, stiffness, and dimension in order to work collaboratively and fully display the potential of this type of composite structures. Again, this result is supported by the test results. From the test, the confinement efficiency increases faster when the rib thickness is increased from ¼ in. (6.35 mm) to ½ in. (12.7 mm) than when the rib thickness is increased from ½ in. (12.7 mm) to ¾ in. (19.0 mm).

It is noted that during testing, the amount of materials used increased as the rib thickness increased; for the FEA model, the amount of materials was kept the same, i.e., the width of the rib decreased as the thickness of the rib increased. This result suggests that using thicker (dimension in the radial direction) and narrower (dimension in the hoop direction) ribs would result in a better confinement. The reason may be that as the rib thickens, the bay becomes deeper. Therefore, there is a higher mechanical interlocking between the grid skeleton and the concrete core.

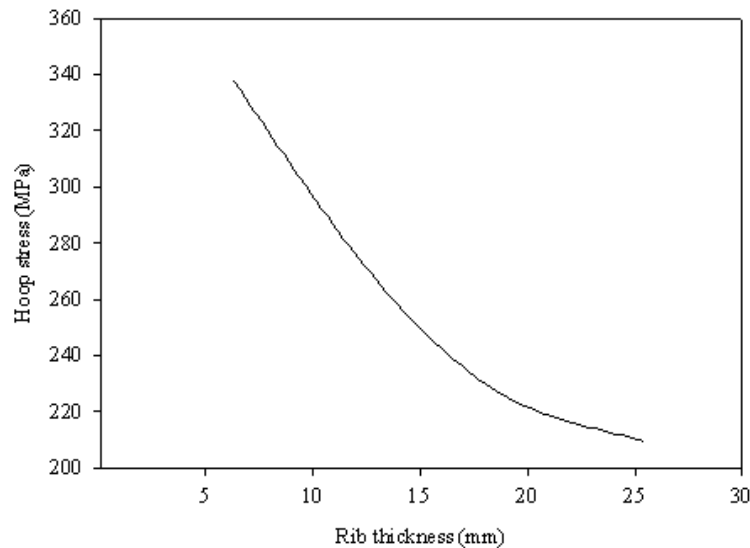


Figure 67
Effect of rib thickness on the maximum hoop stress in the AGS tube

Effect of Bay Area

From Figure 68, increasing the bay area of the grid skeleton decreases the load carrying capacity of the grid cylinders. This is in agreement with the test results. Of course, the difference between the test and the FEA is that the amount of FRP materials used decreases as the bay area increases in the test, while the FRP materials used are constant in the FEA. This is ensured by keeping the rib thickness the same i.e., ½ in. (12.7 mm), and increasing the rib width (dimension in the hoop direction) as the bay area increases.

Again from Figure 68, one might assume that the hoop stress decreases as the bay area decreases and should be the lowest for a cylinder with zero bay area, i.e. a laminated FRP

tube. Figure 69 is rebuilt from Figure 68 by adding the result for an AGS tube with zero bay area, i.e., a regular laminated FRP tube. It is clear that the laminated tube will produce a higher hoop stress than the grid counterparts. Therefore, the AGS tube is better than the laminated FRP tube in terms of confining concrete cylinders. This validates the concept of developing AGS tubes.

Summary

Using the same amount of FRP materials, the FEA suggests that (1) thickening the ribs is more efficient than widening the ribs; (2) there is an optimal bay area corresponding to the lowest hoop tensile stress, although the limited data points cannot precisely predict its value - bay area larger or smaller than the optimal bay area will induce higher hoop tensile stress or lower bearing capacity such as the regular laminated FRP tube, which has a zero bay area; and (3) increasing the skin axial stiffness enhances the confinement efficiency because the skin works more collaboratively with the grid skeleton.

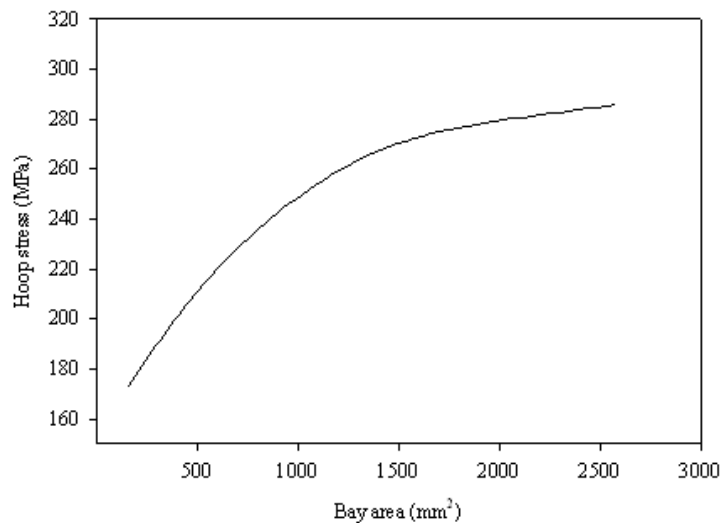


Figure 68
Effect of bay area on the maximum hoop stress in the AGS tube

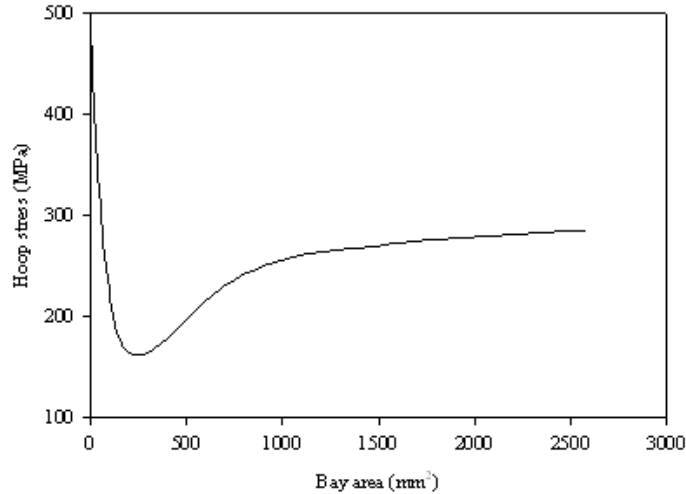


Figure 69

Effect of bay area on the maximum hoop stress in the AGS tube (including zero bay area)

Enhancement of Fire Tolerance

Burning Test

AGS tube encased concrete cylinders exposed to the jet fire during the burning test are shown in Figure 70 (a) and (b) from different viewing angles. It was observed that the high temperature jet fire covered the whole specimen. The part of FRP surface that was burned out released lots of black smoke and irritant gas. However, the specimens with fire retardant additives only released a small amount of smoke.

The mass loss of each encased concrete cylinder after the burning test is given in Table 11. It is seen that the weight loss is the highest for Group A, followed by Groups B and C; the least is Group D. The least weight loss suggests the highest fire resistance. Obviously, nanoclay (Group B) enhanced the fire tolerance as compared to the pure VE (Group A). Similarly, the fire retardant additive also enhanced the fire tolerance of VE (Group C). The combination of nanoclay and fire retardant additive leads to the highest fire resistance (Group D). It is suggested that the exfoliated nanoclay within the VE matrix may have formed many insulating layers and formed a thick charring layer that could partially prevent the chemical reaction between oxygen and VE or reduce the speed of chemical reaction.

Table 11
Mass loss for each group of specimens

Specimen Weight	Specimen Type											
	Group A			Group B			Group C			Group D		
Before Burning Test lb. (kg)	25.51 (11.57)	25.00 (11.34)	25.6 (11.61)	28.20 (12.79)	28.59 (12.97)	28.40 (12.88)	26.30 (11.93)	25.79 (11.70)	26.50 (12.02)	28.11 (12.75)	27.60 (12.52)	27.49 (12.47)
After Burning Test lb. (kg)	24.41 (11.07)	23.10 (10.84)	24.29 (11.02)	27.49 (12.47)	27.60 (12.52)	27.60 (12.52)	25.79 (11.70)	11.39 (11.39)	25.79 (11.70)	27.49 (12.47)	27.09 (12.29)	27.09 (12.29)
Weight Lost lb. (kg)	1.10 (0.50)	1.10 (0.50)	1.30 (0.59)	0.71 (0.32)	0.99 (0.45)	0.79 (0.36)	0.51 (0.23)	0.68 (0.31)	0.71 (0.32)	0.60 (0.27)	0.51 (0.23)	0.40 (0.18)
Average Weight Lost lb. (kg)	1.17 (0.53)			0.84 (0.38)			0.64 (0.29)			0.51 (0.23)		
Standard Deviation lb. (kg)	0.11 (0.05)			0.15 (0.07)			0.11 (0.05)			0.11 (0.05)		

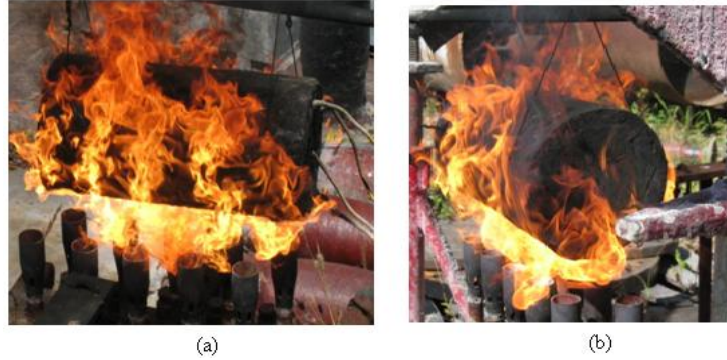
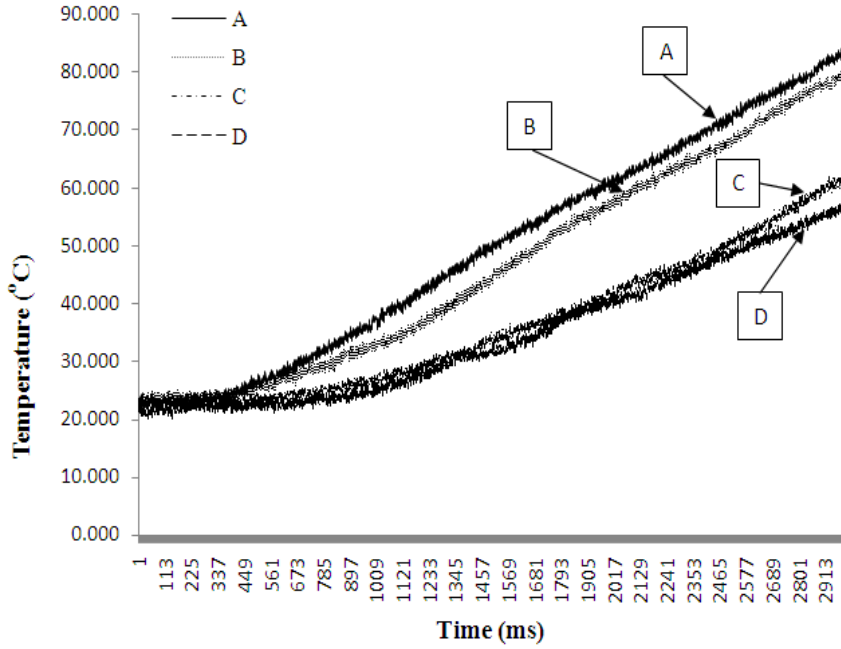


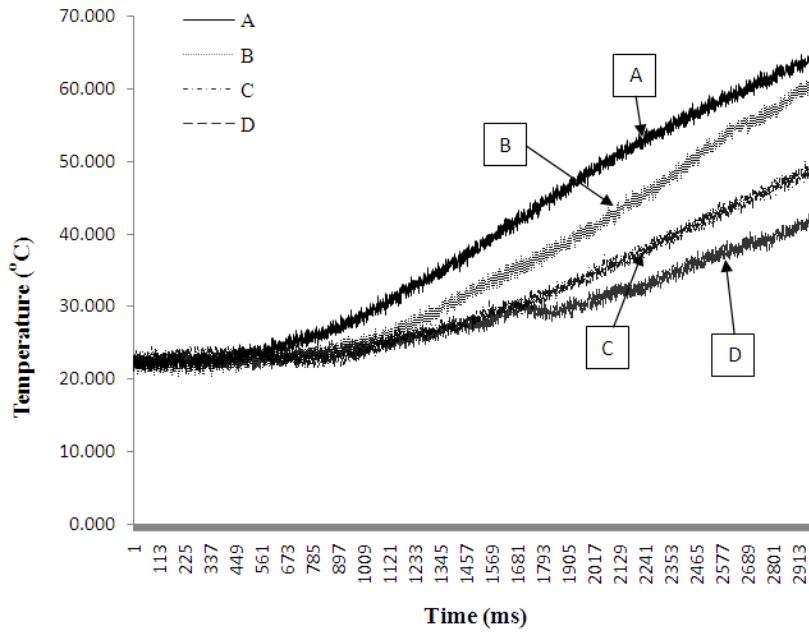
Figure 70
AGS-FRPC specimens under the jet fire (a) front view and (b) side view

The temperature distribution during the burning test was monitored and is schematically shown in Figure 70 with colors representing different temperatures. It is observed that location 1 has the highest temperature because this location is directly exposed to the burner. The lowest temperature location is in the center of the cylinder (location 4). This is because the flame spreads around the cylinder. The center of the cylinder has the longest distance from the fire source. The temperature on the top of the cylinder (location 3) is lower than that in locations 1 and 2, but it is higher than that in location 4 (center of the cylinder). This tendency of temperature distribution is the same for all types of confined cylinders.

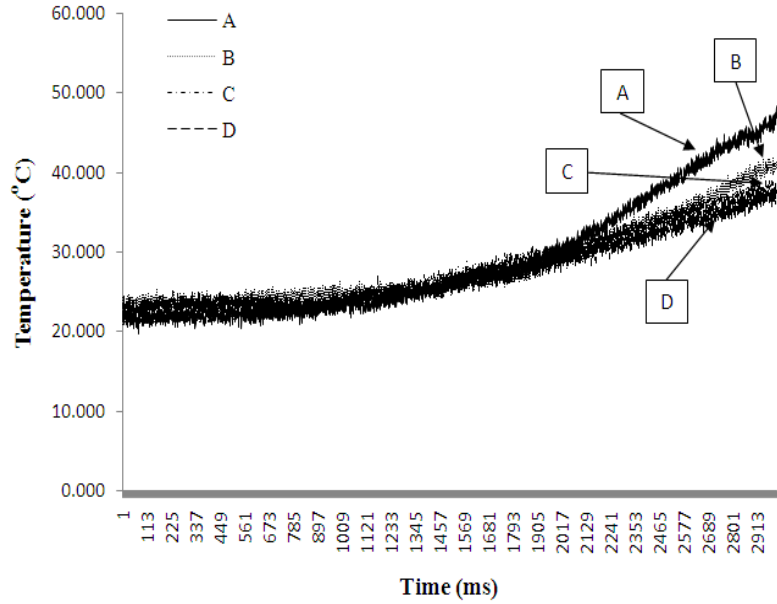
The actual temperature distribution history during the 5 minutes of fire test at each thermocouple location is shown respectively in Figure 71 (a) – (d). The effect of the exfoliated nanoclay and fire retardant additive on reducing the fire hazard can be directly identified from Figure 71 (a) – (d). Comparing Group A with Group B, it is observed that the temperature rise in the nanoclay reinforced specimens (Group B) is systematically lower than the unreinforced counterparts (Group A), and the temperature rise in the specimens consisting of the fire retardant additive is also systematically lower than the specimens without, at all locations (Group C). Actually, the highest temperature in the nanoclay reinforced and fire retardant additive treated specimens after 5 minutes of fire exposure is 136°F (57.8°C), (location 1), (Group D), which is much lower than the highest temperature of the unreinforced and uncoated specimen after 5 minutes of fire exposure, which is 186°F (84.5°C), (location 1), (Group A). It is also noticed that the temperature at the center of the confined cylinder was almost the same after 5 minutes of fire exposure, for all Groups [Figure 71 (d)].



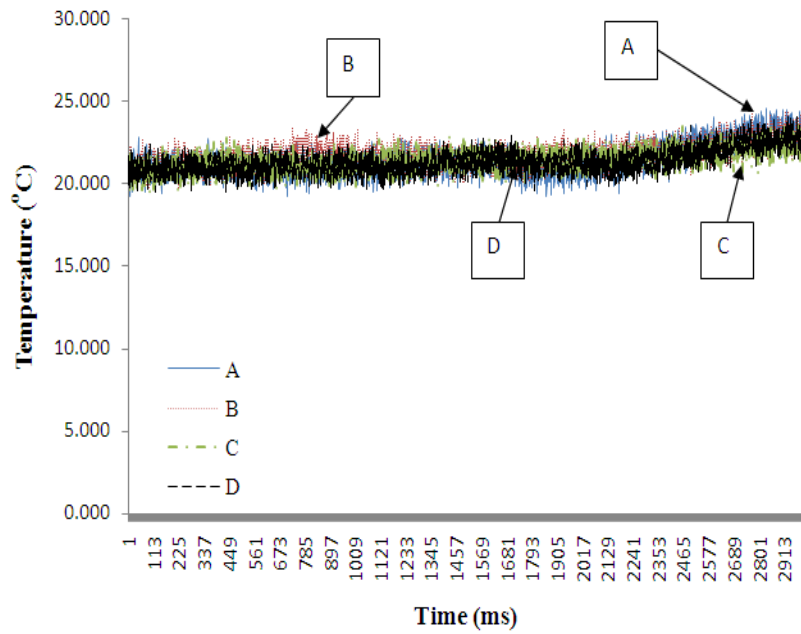
(a) location 1



(b) location 2



(c) location 3



(d) location 4

Figure 71
Temperature history during burning test at (a) location 1, (b) location 2, (c) location 3, and (d) location 4

Uniaxial Compression Test Results

Each group consisted of three effective specimens. A total of 24 AGS tube encased concrete cylinders, which included 12 control specimens and 12 fire tested specimens, were compression tested uniaxially. Specimens before and after the compression test are shown in Figure 72 (a) - (d). The axial stress-axial strain behavior of the confined cylinders both before and after fire exposure is shown in Figure 73 and Figure 74, respectively.

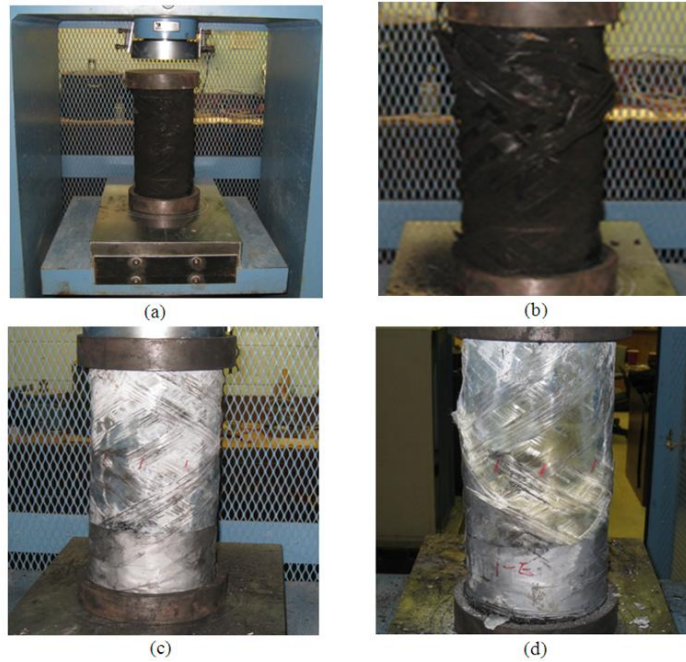


Figure 72

(a) and (b) specimens before and after compression test with fire damage; (c) and (d) control specimens before and after compression test without fire damage

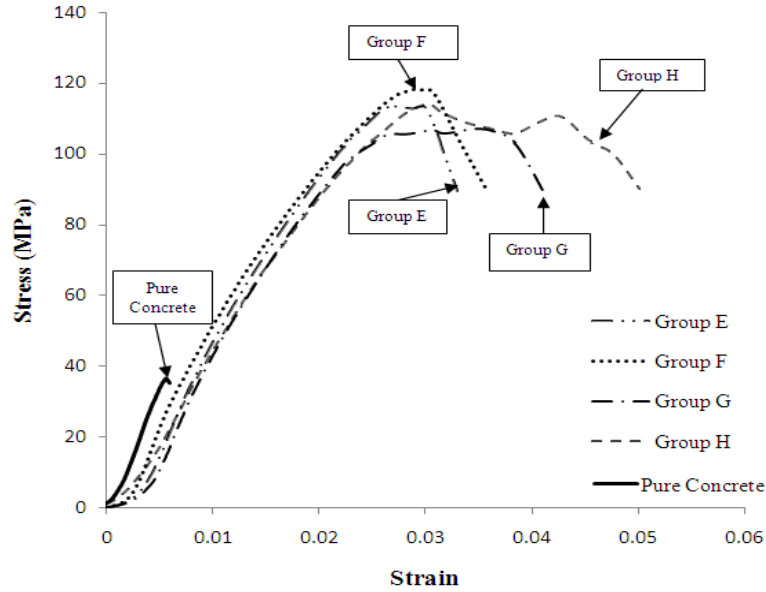


Figure 73
Compressive axial stress-axial strain behavior of AGS-FRPC cylinders and pure concrete cylinders without fire exposure

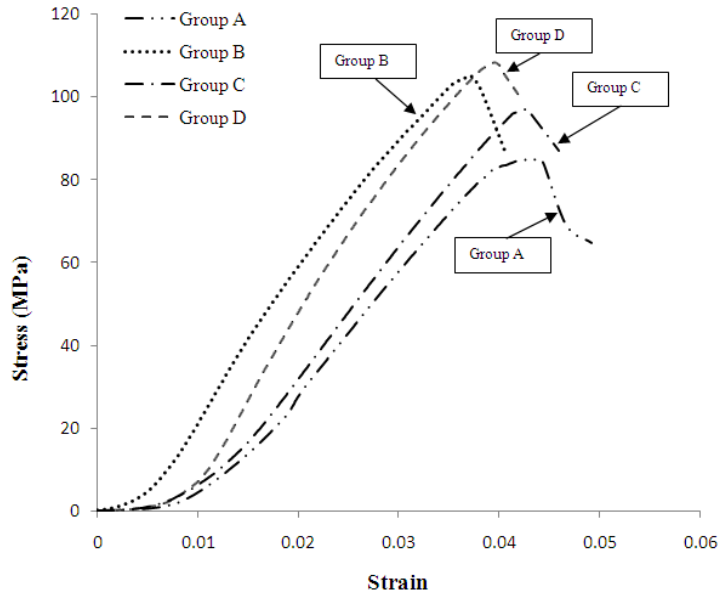


Figure 74
Compressive axial stress-axial strain behavior of AGS-FRPC cylinders after 5 minutes of fire exposure

Comparing the compression behavior of specimens in Figure 73 and Figure 74, the axial stress-strain curve before the peak stress can be represented by a linear section followed by a nonlinear section, instead of the typical bi-linear curve connected by a transition zone for

traditional FRP tube confined concrete cylinders. This type of behavior can be attributed to the unique mechanical interlocking mechanism and composite action between the AGS tube and the concrete core. The AGS tube is engaged in carrying the applied load at the very beginning. As the damage within the concrete core increases, the stress-strain curve turns to a nonlinear curve with a continuous reduction in stiffness until the peak stress is reached. Following the peak stress, the axial stress for some control AGS cylinders did not drop significantly; instead, the stress remained almost constant or even rebounded at some levels (Figure 73). This means that the AGS tube encased concrete cylinder has a considerable ductility and post-peak load carrying capacity. Once one rib fails, the load is redistributed to other ribs through the network connection [1], [2]. For fire damaged specimens, this type of post-peak behavior was not seen. All specimens failed by a monotonically descending branch (Figure 74).

Comparing the compression results in Figure 73 and Figure 74, the fire exposure has a significant effect on the structural behavior and residual strength of the confined cylinders. This can be further validated by the failure mode, which is shown in Figure 72 (b) and (d). The control specimen without firing shows a typical zigzag failure mode of the FRP skin [6], while the burned FRP tube only shows a drum-like lateral expansion.

The averaged peak stress (compressive strength) and standard deviation for each group is summarized in Table 12. Comparing Groups A and B and E and F, it is observed that the nanoclay reinforced AGS tube encased concrete cylinders (Groups B and F) increased the compressive strength either before or after the burning test. This result can be attributed to the exfoliated and well dispersed nanoclay reinforcement.

Comparing Groups A and C, it is observed that the confined cylinder with fire retardant additive (Group C) has higher compressive strength than the confined cylinder without fire retardant additive (Group A) after 5 minutes of the burning test. However, comparing Groups E with G, it shows that the incorporation of fire retardant additive (Group G) reduces the compressive strength without fire damage. This result indicates that the effect of incorporation of fire retardant additive can be seen only after fire damage; otherwise, it has an adverse effect. This is opposite of nanoclay. Nanoclay always shows a positive effect both with and without fire damage.

Table 12
Compressive strength for each group of specimens

Group Name	Average Compressive	Standard Deviation
A	12.5 (86.0)	1.3 (9.0)
B	14.6 (100.5)	1.3 (8.8)
C	13.7 (94.2)	1.1 (7.9)
D	15.3 (105.7)	0.5 (3.5)
E	16.5 (114.0)	0.6 (3.8)
F	17.3 (118.9)	0.9 (5.9)
G	15.7 (108.0)	0.4 (3.0)
H	16.7 (114.8)	0.2 (1.5)

Comparing Groups G and H, it is seen that the additional introduction of nanoclay can recover some of the lost strength due to the incorporation of the fire retardant additive (Group H). It is also noticed that the Group D, which is a nanoclay reinforced AGS tube encased concrete cylinder with FR additive, has the highest compressive strength after 5 minutes of the jet fire burning test. This suggests that the combined nanoclay and FR additive can provide the best fire protection and highest capacity to retain the compressive strength. Comparing Groups B and C and F and G, it is clear that the addition of 1.0 wt.% of nanoclay (Groups B and F) is more effective than the addition of 30.0 wt.% of fire retardant additive (Groups C and G) both with and without fire damage. It is recommended that a small amount of nanoclay addition be considered in practice for both fire tolerance and reinforcement.

Summary

Based on the test results, the following conclusions are obtained:

- Compared with control specimens, the nanoclay increased the compressive strength of the AGS tube confined concrete cylinder both with and without fire damage.
- The fire retardant additive enhanced the compressive strength of the confined cylinders after fire damage; however, it reduced the compressive strength before fire damage as compared with the control specimens.

- The post-fire residual strength is the highest when both nanoclay and fire retardant additive are incorporated.
- It was found that the addition of a small amount of exfoliated nanoclay is more effective than the addition of a large amount of traditional fire retardant additive. It is recommended that nanoclay be a first choice in resisting fire damage and enhancing the structural capacity of AGS tube encased concrete cylinders

CONCLUSIONS

The research presented herein describes the development of a novel AGS tube encased concrete cylinder. A six-stage systematic study including a literature survey, a proof-of-concept study, a manufacturing and parametric study, non-linear finite element modeling, a fire-tolerance study, and an engineering economic analysis were conducted. Some important conclusions were obtained:

- The proof-of-concept study showed that the AGS tube confined concrete cylinders displayed a considerable constructive or positive composite action due to the mechanical interlocking between the AGS grid skeleton and the concrete core. The AGS tube provides an “active” confinement to the concrete core. The elastic range, the specific axial strength, and the specific axial strain of the circular AGS cylinders are considerably higher than those of conventional FRP tube encased concrete cylinders. The square AGS tubes were not as effective as the circular AGS tubes in confining concrete. When subjected to a transverse bending load, it was found that the AGS tube encased concrete beams also showed a significantly higher bending strength than steel grid tube confined concrete counterparts.
- The AGS tube can be automatically manufactured using a two-axis filament winding machine coupled with a pin-guided collapsible mandrel.
- The parametric study showed that (a) the grid skeleton is more effective in confining the concrete core than the skin and (b) with the same amount of FRP materials, AGS tubes have a much higher confinement efficiency than regular laminated FRP tubes.
- The push-out test results showed that the concrete shear strength plays an important role in displaying the positive effect of AGS tube confinement. The AGS tube and the concrete should be designed in such a way that the compressive failure of the concrete core be ahead of the shear failure of concrete teeth. Otherwise, the mechanical interlocking between the grid skeleton and the concrete core cannot be maintained.
- The AGS tube encased concrete cylinder can be modeled and designed using a finite element analysis by considering the non-linear stress-strain constitutive law and by using the non-associative Drucker-Prager plasticity criterion. Some new findings include (a) thickening the ribs is more effective than widening the ribs; and (b) the finite element analysis procedure, along with the parameters taken, is reliable in modeling and designing this type of cylinder.
- It was found that fire exposure had a significant impact on reducing the residual strength of the confined concrete cylinders. The introduction of MMT increased both

fire tolerance and compressive strength of AGS tube encased concrete cylinders. The TSWB[®] fire retardant additive was effective in minimizing the effect of the fire hazard, but it reduced the compressive strength.

- Although there is no sufficient information to quantify the cost-benefits of AGS tube encased concrete columns, it is believed that these new type of columns would be long-term cost-competitive, particularly in corrosive environment.

RECOMMENDATIONS

In this study, a novel confining device, a FRP skin wrapped AGS tube, is proposed and validated through a systematic experimental and theoretical program. The results from this study show that this new confining device outperforms traditional FRP tubes because it develops a positive composite action with the concrete core through mechanical interlocking and it fully utilizes the load carrying capacity of the fibers; it increases the elastic range of the confined cylinders, so the enhanced compressive strength can actually be used in design of encased concrete cylinders. Also, the AGS tube can be manufactured automatically using a two-axis filament winder per a pin-guided collapsible mandrel system. It is concluded that this new confining device has a great potential to replace traditional FRP tubes and should be used as piers, piles, fenders, columns, etc. in the infrastructure. However, the scope of this study was limited. More detailed studies are needed before its practical applications. The following further studies are recommended:

- (1) Beam-column testing
- (2) Joining with other structural members such as footing
- (3) Drivability testing
- (4) Impact testing
- (5) Development of design-oriented confinement model
- (6) Analytical modeling without smearing or homogenizing
- (7) Optimizing structure design

ACRONYMS, ABBREVIATIONS & SYMBOLS

ACI	American Concrete Institute
AGS	Advanced Grid Stiffened
AGS	FRP Tube – Advanced Grid Stiffened Fiber Reinforced Polymer Tube
ANSYS Inc.	An Engineering Simulation Software Provider
ASTM	American Society for Testing and Materials
DERAKANE	Plastics Resin Grades from Ashland Specialty Chemical
ECR	Fiber Glass Similar to E-glass But without Boron and Fluorine
FEA	Finite Element Analysis
FHWA	Federal Highway Administration
FRP	Fiber Reinforced Polymer
GFRP	Glass Fiber Reinforced Polymer
IBRC	Innovative Bridge Research and Construction.
ICG	Interlocked Composite Grid
LHW	Little Hornet Winder
LTRC	Louisiana Transportation Research Center
MEKP	Methyl Ethyl Ketone Peroxide
MMT	Montmorillonite
NEFMAC	New Fiber Composite Material for Reinforced Concrete
RC	Reinforced Concrete
RO99	Saint-Gobain Vetrotex Trade Name for Direct Roving
UV	Ultraviolet
VE	Vinyl Ester

REFERENCES

1. Hollaway, L.C., "The Evolution of and the Way Forward for Advanced Polymer Composites in Civil Infrastructures," *Construction and Building Materials*, 17, 2003 pp. 365-378.
2. Mirmiran, A.; Bank, L.C.; Neale, K.W.; Mottram, J.T.; Ueda, T.; and Davalos, J.F., "World Survey of Civil Engineering Programs on Fiber Reinforced Polymer Composites for Construction," *Journal of Professional Issues in Engineering Education and Practice*, 129, 2003, pp. 155-160.
3. Li, G.; Maricherla, D.; Singh, K.; Pang, S.S.; and John, M., "Effect of Fiber Orientation on the Structural Behavior of FRP Wrapped Concrete Cylinders," *Composite Structures*, 74, 2006, pp. 475-483.
4. Li, G.; Kidane, S.; Pang, S.S.; Helms, J.E.; and Stubblefield, M.A., "Investigation into FRP Repaired RC Columns," *Composite Structures*, 62, 2003, pp. 83-89.
5. Li, G.; Hedlund, S.; Pang, S.S.; Alaywan, W.; Eggers, J.; and Abadie, C., "Repair of Damaged RC Columns Using Fast Curing FRP Composites," *Composites Part B: Engineering*, 34, 2003, pp. 261-271.
6. Li, G.; Torres, S.; Alaywan, W.; and Abadie, C., "Experimental Study of FRP Tube-Encased Concrete Columns," *Journal of Composite Materials*, 39, 2005, pp. 1131-1145.
7. Li, G., "Experimental Study of FRP Confined Concrete Cylinders," *Engineering Structures*, 28, 2006, pp. 1001-1008.
8. Li, G., "Experimental Study of Hybrid Composite Cylinders," *Composite Structures*, 78, 2007, pp. 170-181.
9. Huybrechts, S.M. and Tsai, S.W., "Analysis and behavior of grid structures," *Composites Science and Technology*, 56, 1996, pp. 1001-1015.
10. Dutta, P.K.; Bailey, D.M.; Tsai, S.W.; Jensen, D.W.; Hayes Jr., J.R.; McDonald, W.E.; Smart, C.W.; Colwell, T.; Earl, J.S.; and Chen, H.-J., "Composite Grid/Frame Reinforcement for Concrete Structures," Construction Productivity Advancement Research (CPAR) Program, USACERL Technical Report 98/81, 1998.
11. Jaunky, N. and Knight Jr, N.F., "Formulation of an Improved Smear Stiffener Theory for Buckling Analysis of Grid-Stiffened Composite Panels," *Composite Part B: Engineering*, 27B, 1996, pp. 519-526.

12. Jaunky, N.; Knight Jr, N.F.; and Amburb, D.R., "Optimal Design of General Stiffened Composite Circular Cylinders for Global Buckling with Strength Constraints," *Composite Structures*, 41, 1998, pp. 243-252.
13. Hohe, J.; Beschoner, C.; and Becker, W., "Effective Elastic Properties of Hexagonal and Quadrilateral Grid Structures," *Composite Structures*, 46, 1999, pp. 73-89.
14. Lennon, R.F. and Das, P.K., "Torsional Buckling Behaviour of Stiffened Cylinders under Combined Loading," *Thin-Walled Structures*, 38, 2000, pp. 229-245.
15. Kidane, S.; Li, G.; Helms, J.E.; Pang, S.S.; and Woldeesenbet, E., "Analytical Buckling Load Analysis of Grid Stiffened Composite Cylinders," *Composite Part B: Engineering*, 33, 2003, pp. 1-9.
16. Ambur, D.R.; Jaunky, N.; and Hilburger, M.W., "Progressive Failure Studies of Stiffened Panels Subjected to Shear Loading," *Composite Structures*, 65, 2004, pp. 129-142.
17. Li, G. and Cheng, J.Q., "A Generalized Analytical Modeling of Grid Stiffened Composite Structures," *Journal of Composite Materials*, 41, 2007, pp. 2939-2969.
18. Huybrechts, S.M.; Meink, T.E.; Wegner, P.M.; and Ganley, G.M., "Manufacturing Theory for Advanced Grid Stiffened Structures," *Composite Part A: Applied Science & Manufacturing*, 33, 2002, pp. 155-161.
19. Han, D.Y. and Tsai, S.W., "Interlocked Composite Grids Design and Manufacturing," *Journal of Composite Materials*, 37, 2003, pp. 287-316.
20. Bouabdallah, M.S. and Batoz, J.L., "Formulation and Evaluation of a Ainite Element Model for the Linear Analysis of Stiffened Composite Cylindrical Panels," *Finite Elements in Analysis and Design*, 21, 1996, pp. 265-289.
21. Kassegne, S.K. and Reddy, J.N., "Local Behavior of Discretely Stiffened Composite Plates and Cylindrical Shells," *Composite Structures*, 41, 1998, pp. 13-26.
22. Samanta, A. and Mukhopadhyay, M., "Free Vibration Analysis of Stiffened Shells by the Finite Element Technique," *European Journal of Mechanics A/Solids*, 23, 2004, pp. 159-179.
23. Knight, N.F. and Stranes, J.H., "Development in Cylindrical Shell Stability Analysis," NASA report, 1997.
24. Graham J., "Preliminary Analysis Techniques for Ring and Stringer Stiffened Cylindrical Shells," NASA report TM-108399, 1993.

25. Phillips, J.L. and Gurdal, Z., "Structural Analysis and Optimum Design of Geodesically Stiffened Composite Panels," NASA Report CCMS-90-05, 1990.
26. Wang, J.T.S. and Hsu, T.M., "Discrete Analysis of Stiffened Composite Cylindrical Shells," *AIAA Journal*, 23, 1995, pp. 1753-1761.
27. Hilburger, M.W., "Nonlinear and Buckling Behavior of Compression-loaded Composite Shells," Proceedings of the 6th Annual Technical Conference of the American Society for Composites, VA, 2001.
28. Hyer, M.W. and Riddick, J.C., "Effect of Imperfections of Buckling and Postbuckling Response of Segmented Circular Composite Cylinders," Proceedings of the 6th Annual Technical Conference of the American Society for Composites, VA, 2001.
29. Helms, J.E.; Li, G.; and Smith, B.H., "Analysis of Grid Stiffened Cylinders," Proceedings of ASME/ETCE 2001, Houston, TX, 2001.
30. Sugita, M.; Nakatsuji, T.; Sekijima, K.; and Fujisaki, T., "Applications of FRP Grid Reinforcement to Precast Concrete Panels," *Advanced Composite Materials in Bridges and Structures*, Canadian Society for Civil Engineering, 1992.
31. Bank, L.C.; Xi, Z.; and Mosallam, A.S., "Experimental Study of FRP Grating Reinforced Concrete Slabs," *Proceedings of the Advanced Composite Materials in Civil Engineering Structures Specialty Conference*, Las Vegas, NV, ASCE, 1991, pp. 111-122.
32. Schmeckpeper, E.R. and Goodspeed, C.H., "Fiber-Reinforced Plastic Grid for Reinforced Concrete Construction," *Journal of Composite Materials*, 28, 1994, pp. 1288-1304.
33. Larralde, A.M. and Zerva, A., "Load/deflection Performance of FRP Grating-Concrete Composites," *Proceedings of the Advanced Composite Materials in Civil Engineering Structures Specialty Conference*, Las Vegas, NV, ASCE, 1991, pp. 271-277.
34. Banthia, N.; Al-Asaly, M.; and Ma, S., "Behavior of Concrete Slabs Reinforced with Fiber-Reinforced Plastic Grid," *Journal of Materials in Civil Engineering*, 7, 1995, pp. 252-257.
35. Sugita, M., "NEFMAC grid type reinforcement," *Alternative Materials for Concrete Reinforcement*, Blackie Academic, NY, 1993, pp. 55-69.

36. Smart, C.W. and Jensen, D.W., "Flexure of Concrete Beams Reinforced with Advanced Composite Orthogrids," *Journal of Aerospace Engineering*, 10, 1997, pp.7-15.
37. Matthys, S. and Taerwe, L., "Concrete Slabs Reinforced with FRP Grid. I: One-Way Bending," *Journal of Composites for Construction*, 4, 2000, pp. 145-153.
38. Yost, J.R.; Goodspeed, C.H.; and Schmeckpeper, E.R., "Flexural Performance of Concrete Beams Reinforced with FRP Grids," *Journal of Composites for Construction*, 5, 2001, pp. 18-25.
39. Huang, H.; Chajes, M.J.; Mertz, D.R.; Shenton, H.W.; and Kaliakin, V.N., "Behavior of Open Steel Grid Decks for Bridges," *Journal of Constructional Steel Research*, 58, 2002, pp. 819-842.
40. Zhang, B.; Masmoudi, R.; and Benmokrane, B., "Behaviour of One-Way Concrete Slabs Reinforced with CFRP Grid Reinforcements," *Construction and Building Materials*, 18, 2004, pp. 625-635.
41. Berg, A.C.; Bank, L.C.; Oliva, M.G.; and Russell, J.S., "Construction and Cost Analysis of an FRP Reinforced Concrete Bridge Deck," *Construction and Building Materials*, 20, 2006, pp. 515-526.
42. Saafi, M., "Design and Fabrication of FRP Grids for Aerospace and Civil Engineering Applications," *Journal of Aerospace Engineering*, 13, 2000, pp. 144-149.
43. Samaan, M.; Mirmiran, A.; and Shahawy, M., "Modeling of Concrete Confined by Fiber Composites," *Journal of Structural Engineering*, 124, 1998, pp. 1025-1031.
44. Li, G.; John, M.; and Maricherla, D., "Experimental Study of Hybrid Composite Beams," *Construction and Building Materials*, 21, 2007, pp. 601-608.
45. Gibson, R.F., "*Principles of composite materials mechanics*," McGraw-Hill, Inc., NY, 2004.
46. Li, G. and Maricherla, D., "Advanced Grid Stiffened Fiber Reinforced Plastic Tube Encased Concrete Cylinders," *Journal of Composite Materials*, 41, 2007, pp.1803-1824.
47. Lam, L. and Teng, J.G., "Strength Models for Fiber-Reinforced Plastic-Confined Concrete," *Journal of Structural Engineering*, 128, 2002, pp. 612-23.
48. Lam, L. and Teng, J.G., "Design-Oriented Stress-Strain Model for FRP-Confined Concrete," *Construction and Building Materials*, 17, 2003, pp. 471-89.

49. Mirmiran, A.; Zagers, K.; and Yuan, W., "Nonlinear Finite Element Modeling of Concrete Confined by Fiber Composites," *Finite Elements in Analysis and Design*, 35, 2000, pp. 79-96.
50. Richart, F.E.; Brandtzaeg, A.; and Brown, R.L., "A study of the Failure of Concrete under Combined Compressive Stresses," Engineering Experimental Station Bull, Vol. 185, Urbana, IL, University of Illinois, 1928.
51. Chansawat, K.; Yim, S.C.S.; and Miller, T.H., "Nonlinear Finite Element Analysis of a FRP-Strengthened Reinforced Concrete Bridge," *Journal of Bridge Engineering*, 11, 2006, pp. 21-32.
52. Feih, S.; Mathys, Z.; Gibson, A.G.; and Mouritz, A.P., "Modeling the Tension and Compression Strengths of Polymer Laminates in Fire," *Composites Science and Technology*, 67, 2007, pp. 551-564.
53. Harries, K.A.; Porter, M.L.; and Busel, J.P., "FRP Materials and Concrete - Research Needs," *Concrete International, ACI*, 25, 2003, pp. 69-74.
54. Hussain, F.; Hojjati, M.; Okamoto, M.; and Gorga, R.E., "Review Article: Polymer-Matrix Nanocomposites, Processing, Manufacturing, and Application: An Overview," *Journal of Composite Materials*, 40, 2006, pp. 1511-65.
55. Ji, G.; Li, G.; Li, X.; Pang, S.; and Jones, R., "Experimental Study of FRP Tube Encased Concrete Cylinders Exposed to Fire," *Composite Structures*, 85, 2008, pp. 149-154.
56. Platts, <http://www.platts.com/Metals/Resources/News%20Features/rebar/index.xml>, accessed December 15, 2007.

APPENDIX A

Engineering Economic Analysis

In order to conduct the engineering economic analysis of the proposed AGS tube encased concrete column, researchers compared its raw materials cost with that of a reference column, which was a steel reinforced concrete column for a highway bridge.

The reference column included a cap, body of the column, and footing. However, only the body of the column was considered replaceable by the AGS tube encased concrete column. The footing and cap remained unchanged from the original design.

10-ft Concrete column

The cylindrical body of the column was 10 ft. (304.8 cm) long and 30 in. (76.2 cm) in diameter.

$$V_{\text{col}} = \frac{\pi (30 \text{ in})^2}{4 \cdot 144} (10 \text{ ft}) \left(\frac{1}{27}\right) = 1.82 \text{ cu. yd. (1.39 m}^3\text{)}$$

Assuming Volume of steel is 4% of total volume:

$$V_{\text{steel}} = 0.04(1.82) = 0.073 \text{ cu.yd. (0.056 m}^3\text{)}$$

$$V_{\text{con}} = 0.96 (1.82) = 1.75 \text{ cu. yd. (1.34 m}^3\text{)}$$

Cost of steel is \$0.91/lb.

$$\text{Steel Cost} = 0.91 \frac{\$}{\text{lb}} \left(0.073 \text{ cu. yd} * 27 \frac{\text{ft}^3}{\text{cu. yd}} * 495 \frac{\text{lb}}{\text{ft}^3} \right) = \$529$$

$$\text{Concrete Cost} = 826 \frac{\$}{\text{ft}^3} (0.96 * 1.82 \text{ cu. yd}) = \$1443$$

The cost of a 10-ft concrete column will be: $\$529 + 1443 = \1972 .

10-ft FRP column

According to the design, the diameter of the steel reinforced concrete column was $D = 30$ in. (76.2 cm) with cross-section area of 706.5 in^2 ($455,805.5 \text{ cm}^2$). As calculated in Appendix B, the concrete core diameter d_g of the AGS tube encased concrete column is 25.9 in. (65.79 cm) with a cross-sectional area of 526.7 in^2 ($3,398 \text{ cm}^2$).

According to the calculation in Appendix B, the use of FRP in the AGS encased tube concrete column may be equivalent to that of an FRP jacketed concrete column with jacket thickness of 0.4 in. (10.36 mm).

The cross-sectional views of the steel reinforced concrete column and the AGS concrete column (replaced by the equivalent FRP jacket) are plotted in Figures 75 and 76, respectively.

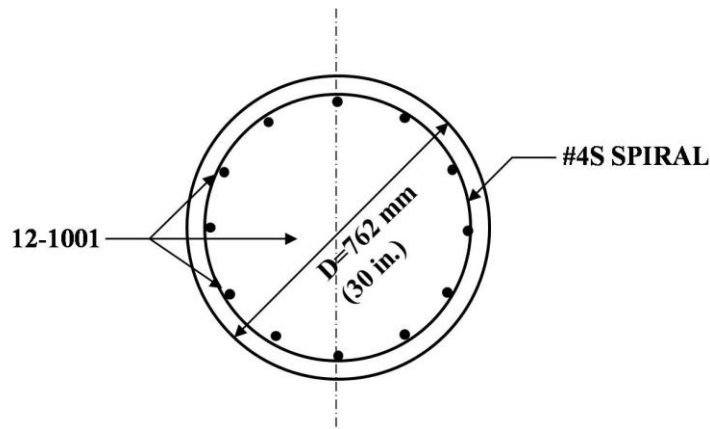


Figure 75
Cross-section sketch of steel reinforced concrete column

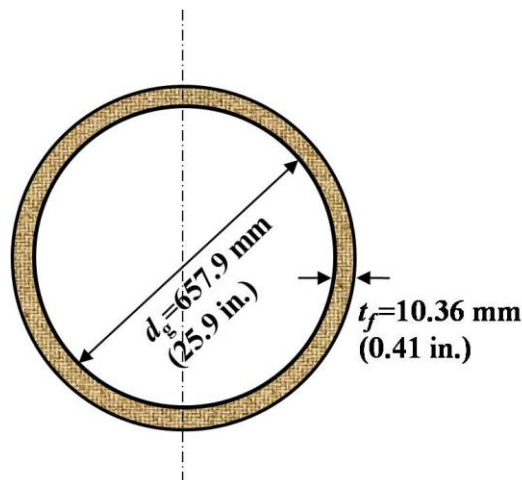


Figure 76
Cross-section of the equivalent FRP jacketed concrete column

It is important to note that the actual rib thickness of the AGS tube should be determined based on the principle that the equivalent FRP jacket with thickness $t_f = 0.41 \text{ in.}$ (10.41mm) should have the same mass as the AGS tube.

$$V_{\text{col}} = \frac{\pi (25.9 \text{ in})^2}{4 \cdot 144} (10 \text{ ft}) \left(\frac{1}{27}\right) = 1.36 \text{ cu. yd. (1.04 m}^3\text{)}$$

$$V_{\text{FRP}} = \frac{\pi}{4} * [(25.9 \text{ in} + 2 * 0.41 \text{ in})^2 - (25.9 \text{ in})^2] * 1 \frac{\text{ft}^2}{144 \text{ in}^2} * 10 \text{ ft} = 2.35 \text{ ft}^3 (0.067\text{m}^3)$$

$$\text{FRP Cost} = 2.35 \text{ ft}^3 * 106 \frac{\text{lbs}}{\text{ft}^3} * 5.5 \frac{\$}{\text{lb}} = \$1370$$

$$\text{Concrete Cost} = 1.36 \text{ cu. yd} * 826 \frac{\$}{\text{cu yd.1}} = \$1,123$$

Total cost for a 10-ft FRP Column: \$1370 + 1123 = \$2,493

Observation:

Compared to the reference steel reinforced concrete column (\$1,972), the equivalent FRP jacketed concrete column (\$2,430) has a higher direct material cost, 26 percent. Though the cost of the new product is higher, this product is corrosion-free and formwork-free.

APPENDIX B

Computation of Axial Capacity of Different Sections

In this analysis, researchers assumed that the design will ensure the failure occur within the column, instead of the cap or footing. Researchers also assumed that the load carrying capacity of the column will be controlled by the axial compressive load. Then, according to Sec. 10.3.6.2 of ACI 318-08, the maximum axial load capacity P_{\max} is calculated by (without bending):

$$P_{\max} = F \cdot \phi \cdot [0.85 f'_c (A_g - A_{st}) + f_y A_{st}] \quad (9)$$

where,

$$F = 0.8; \quad \phi = 0.65 \quad (\text{ACI 318-08, Sec. 10.3.6.1}) \quad (10)$$

According to the design, the diameter of the steel reinforced concrete column is $D = 30$ in. (762 mm), thus:

$$A_g = \frac{\pi D^2}{4} = \frac{3.14 \times 30^2}{4} = 706.5 \text{ in.}^2 (455,800 \text{ mm}^2)$$

There are 12 vertical No. 10 steel reinforcement bars used in the design. The total area of the vertical steel bars, A_{st} , is:

$$A_{st} = 12 \times 12.7 \text{ in}^2 = 15.24 \text{ in}^2 (9,832 \text{ mm}^2)$$

The yielding strength of the vertical rebar (f_y) is assumed to be 60 ksi (413.4), and the compressive strength of the concrete (f'_c) is assumed to be 3.5 ksi (2.4.1MPa). The load carrying capacity of the steel bar reinforced concrete column is:

$$P_{\max} = 0.8 \times 0.65 \times [0.85 \times 3.5 \times (706.5 - 15.24) + 60 \times 15.24] = 1,545 \text{ kips (6,868 kN)}$$

Currently, there are no design equations available for the proposed AGS tube encased concrete column. However, according to the test results in this project, the improvement in concrete compressive strength by the AGS tube is higher than that by the traditional FRP jacket. Therefore, to be conservative, researchers used the design code of FRP jacketed concrete column for the design of AGS tube encased concrete column.

According to ACI 440.2R-02 code, the maximum load of FRP jacketed concrete column may be calculated for the nonprestressed members with existing steel-tie as (without bending):

$$P_{\max} = 0.8 \cdot \phi \cdot [0.85 \Psi_f (f'_{cc} (A_g - A_{st}) + f_y A_{st})] \quad (11)$$

Since there are no vertical steel bars for the AGS tube encased concrete column, the maximum load may be calculated by:

$$P_{\max} = 0.8 \cdot \phi \cdot [0.85 \Psi_f f'_{cc} A_g] \quad (12)$$

where, $\phi = 0.65$, and $\Psi_f = 0.95$.

The compressive strength of the FRP confined concrete f'_{CC} can be calculated:

$$f'_{CC} = f'_c \left[2.25 \sqrt{1 + 7.9 \frac{f_l}{f'_c}} - 2 \frac{f_l}{f'_c} - 1.25 \right]$$

where,

$$f_l = \frac{2 f_{fe} \cdot t_f}{d} = \frac{2 \varepsilon_{fe} \cdot E_f \cdot t_f}{d} \quad (14)$$

in which f_{fe} is the effective stress in the FRP when the tensile stress reaches the failure level (MPa); t_f is the total thickness of the FRP jacket; d is the diameter of the confined concrete core; ε_{fe} is the effective hoop strain, which is suggested to be 0.004; and E_f is the elastic modulus of the equivalent FRP jacket. Depending on the quantity of the equivalent FRP jacket used for confinement, the confinement improvement ratio f'_{CC}/f'_c is typically in the range between 2 and 3. From the test results of AGS, the improvement ratio can be up to about 4.

For the sake of safety, **the confinement improvement ratio of the AGS tube is assumed to be only 2** ($f'_{CC} = 2f'_c$) for this analysis. The calculation of the load carrying capacity is based on the formulation for the FRP jacket design code (ACI 440). In other words, the actual load carrying capacity of the AGS tube should be higher than that reported for the equivalent FRP jacketed concrete column.

To be conservative, researchers used:

$$\frac{f'_{CC}}{f'_c} = \left[2.25 \sqrt{1 + 7.9 \frac{f_l}{f'_c}} - 2 \frac{f_l}{f'_c} - 1.25 \right] = 2 \quad (15)$$

With, $f'_c = 3.5$ ksi (24.1 MPa), the above equation can be rewritten as:

$$0.326 f_l^2 - 7.71 f_l + 5.5 = 0 \quad (16)$$

Note the unit in equation (16) is ksi. By solving the above quadratic equation, the two roots are:

$$f_t = 22.9 \text{ ksi (158 MPa) and } f_t = 0.74 \text{ ksi (3.78 MPa)}$$

If $f_t = 22.9 \text{ ksi (158MPa)}$, then:

$$\frac{2 \times 0.004 \times E_f \cdot t_f}{d} = 22.9 \text{ ksi (158 MPa)}$$

If $f_t = 3.78\text{MPa (0.74 ksi)}$, then:

$$\frac{2 \times 0.004 \times E_f \cdot t_f}{d} = 0.74 \text{ ksi (3.78MPa)}$$

The purpose is to determine the d and t_f for a given DFRP. Consider a typical $E_f = 4,354 \text{ ksi (30 GPa)}$ for GFRP, obviously, researchers cannot solve d and t_f using one equation.

Therefore, we first assume a diameter d . Assuming that the diameter of the concrete core is 29 in. (736.6 mm), which is slightly less than the designed diameter 30 in. (762 mm) of the reference steel reinforced concrete column, the thickness of the FRP jacket t_f can be estimated by the following equations for $f_t = 22.9 \text{ ksi (158 MPa)}$ or $f_t = 0.74 \text{ ksi (3.78 MPa)}$:

$$\frac{2 * 0.004 * 30 * t_f}{29} = 0.74 \text{ ksi (3.78 MPa)}$$

$$\frac{2 * 0.004 * 30 * t_f}{29} = 22.9 \text{ ksi (158 MPa)}$$

Then, researchers find that the thickness of the FRP jacket should be:

$$t_f = 0.46 \text{ in. (11.6 mm) for } f_t = 0.74 \text{ ksi (3.78MPa)}$$

$$t_f = 19.1 \text{ in. (485 mm) for } f_t = 22.9 \text{ ksi (158MPa)}$$

Obviously, based on the established knowledge in previous studies that a thin layer of FRP jacket can improve the compressive strength of concrete by several times, $t_f = 0.46 \text{ in. (11.6 mm)}$ must be the physically meaningful solution.

In other words, the true root of equation (16) must be $f_t = 0.74 \text{ ksi (3.78 MPa)}$. On the other hand, by using equation (11):

$$P_{\max} = 0.8 \cdot \phi \cdot [0.85 \cdot \Psi_f \cdot f'_{cc} \cdot A_g] \quad (17)$$

where,

$\phi = 0.65$ and $\psi_f = 0.95$.

The design is based on such a principle that the load carrying capacity of the AGS tube encased concrete column is equal to that of the reference steel reinforced concrete column as calculated by equation (9).

The compressive strength of the equivalent FRP jacketed concrete is:

$$f'_{cc} = 2f'_c = 2 \times 3.5 = 7 \text{ ksi (48.2 MPa)}$$

Therefore, the actual thickness of FRP jacket required can be calculated by

$$0.8 * 0.65 * \left[0.85 * 0.95 * 7 * \frac{\pi}{4} * d_g^2 \right] = 1,545 \text{ ksi}$$

where d_g is the diameter of the concrete core. It can be solved that:

$$d_g = 25.9 \text{ in. (657.9 mm)}$$

As discussed before, $f_1 = 0.74 \text{ ksi (3.78 MPa)}$. With the core diameter of the equivalent FRP jacketed concrete column $d_g = 25.9 \text{ in. (657.9 mm)}$, the actual thickness of the FRP jacket t_f with $E_f = 4,354 \text{ ksi (30 GPa)}$ is calculated by:

$$\frac{2 * 0.004 * 4.354 * t_f}{25.9} = 0.50 \text{ ksi (3.78 MPa)}$$

Finally, researchers find that the actual thickness of the FRP jacket should be

$$t_f = 0.41 \text{ in. (10.36 mm)}$$

The cross-sectional area of the equivalent FRP jacket then can be calculated by:

$$\frac{3.14}{4} * [(25.9 + 2 * 10.36)^2 - 25.9^2] = 33.7 \text{ in}^2 \text{ (21,749 mm}^2\text{)}$$

Since the length of the equivalent FRP jacket is 10 ft. (3,048 mm), assuming that the typical density of the GFRP is $106 \text{ lb}_m/\text{ft}^3$ (1.7 g/cm^3), the weight of the GFRP jacket should be:

$$106 \times 33.7 / 144 \times 10 = 248 \text{ lb. (112.6 kg)}$$